Advances In Fuel Cell Vehicle Design

by

Jennifer Bauman

A thesis
presented to the University of Waterloo
in fulfillment of the
thesis requirement for the degree of
Doctor of Philosophy
in
Electrical and Computer Engineering

Waterloo, Ontario, Canada, 2008

Author's Declaration

I hereby declare that I am the sole author of this thesis. This is a true copy of the thesis, including any required final revisions, as accepted by my examiners.

I understand that my thesis may be made electronically available to the public.

Signature

Abstract

Factors such as global warming, dwindling fossil fuel reserves, and energy security concerns combine to indicate that a replacement for the internal combustion engine (ICE) vehicle is needed. Fuel cell vehicles have the potential to address the problems surrounding the ICE vehicle without imposing any significant restrictions on vehicle performance, driving range, or refuelling time. Though there are currently some obstacles to overcome before attaining the widespread commercialization of fuel cell vehicles, such as improvements in fuel cell and battery durability, development of a hydrogen infrastructure, and reduction of high costs, the fundamental concept of the fuel cell vehicle is strong: it is efficient, emits zero harmful emissions, and the hydrogen fuel can be produced from various renewable sources. Therefore, research on fuel cell vehicle design is imperative in order to improve vehicle performance and durability, increase efficiency, and reduce costs. This thesis makes a number of key contributions to the advancement of fuel cell vehicle design within two main research areas: powertrain design and DC/DC converters.

With regards to powertrain design, this research first analyzes various powertrain topologies and energy storage system types. Then, a novel fuel cell-battery-ultracapacitor topology is presented which shows reduced mass and cost, and increased efficiency, over other promising topologies found in the literature. A detailed vehicle simulator is created in MATLAB/Simulink in order to simulate and compare the novel topology with other fuel cell vehicle powertrain options. A parametric study is performed to optimize each powertrain and general conclusions for optimal topologies, as well as component types and sizes, for fuel cell vehicles are presented. Next, an analytical method to optimize the novel battery-ultracapacitor energy storage system based on maximizing efficiency, and minimizing cost and mass, is developed. This method can be applied to any system utilizing the novel battery-ultracapacitor energy storage system and is not limited in application to only fuel cell vehicles.

With regards to DC/DC converters, it is important to design efficient and light-weight converters for use in fuel cell and other electric vehicles to improve overall vehicle fuel economy. Thus, this research presents a novel soft-switching method, the capacitor-switched regenerative snubber, for the high-power DC/DC boost converters commonly used in fuel cell vehicles. This circuit is shown to increase the efficiency and reduce the overall mass of the DC/DC boost converter.

Acknowledgements

I would like to express my deepest gratitude to my parents. They always encouraged me to follow my dreams and taught me I could achieve everything I wanted if I worked hard. I especially want to thank my mother for her unwavering support and for always being there to give me love and advice. Thanks also to my brother James for being a wonderful friend.

I am forever grateful for Douglas, my beloved husband, who has stood by me through all the successes and setbacks that come with graduate research. His never-ending confidence in me and what I could do is worth more to me than he will ever know.

I will always be grateful to my supervisor, Dr. Mehrdad Kazerani, who has provided unwavering guidance and continuous support to me throughout my graduate studies. At times I cannot believe I got so lucky as to end up with such a smart, thoughtful, and encouraging supervisor. After each and every meeting with him, I left feeling energized, positive, and full of ideas on how to further improve my research. I cannot thank him enough for all he’s done for me. Thanks also to Dr. Fraser, Dr. Aplevich, and Dr. Jayaram, members of my committee, for their confidence and suggestions.

I want to thank UWAFT for letting me join their boys club and build a DC/DC converter for a fuel cell vehicle, which was an incredible experience. Being a part of UWAFT from 2004-2006 gave me countless memories of our travels, competitions, endless nights in the garage, and in-depth discussions, as well as many cherished friendships. I am also grateful to my past and current labmates in the power electronics lab for their friendship and encouragement.

This research has been supported by two NSERC graduate scholarships and so I would like to thank the Natural Sciences and Engineering Research Council of Canada for their confidence in my research and its potential applications and benefits.

Table of Contents

List of Figures

List of Tables

Chapter 1
Introduction

1.1 Motivation for Fuel Cell Vehicle Research

Factors such as dwindling fossil fuel reserves, energy security concerns, and unacceptably high air pollution levels combine to indicate that a replacement for the internal combustion engine (ICE) vehicle is needed, and soon. These issues are briefly discussed below in order to heighten motivation for fuel cell vehicle research.

A report by The US Department of Energy states that "All or very nearly all of Earth's prolific petroleum basins are believed identified and most are partially to near-fully explored. All or nearly all of the largest oil fields in them have already been discovered and are being produced. Production is indeed clearly past its peak in some of the most prolific basins."[1]. To further compound this problem, world crude oil demand has been growing at an annualized compound rate of just over 2% in recent years [1]. The highest demand is in China and India, and is primarily due to rapidly rising consumer demand for ICE cars and trucks [1]. Figure 1-1 [1] shows an estimate for the world's annual oil production, based on a 2% production growth per year and a decline after the projected peak. Thus, according to these resource estimates, the expected world conventional crude oil production would be expected to peak in 2037 at a volume of 53.2 billion barrels per year. However, there is much discrepancy among governments and experts as to how much oil is left, and when production will peak. The one known certainty is that oil is a finite resource and thus society must shift towards renewable energy sources in order to survive peacefully into the future.

In addition to dwindling oil reserves, society must deal with other very serious side-effects of relying heavily on fossil fuels. The Intergovernmental Panel on Climate Change states in its 2007 Synthesis Report [2] that "warming of the climate system is unequivocal", as shown by data in Figure 1-2 [2]. The report also states that "Most of the observed increase in globally-averaged temperatures since the mid-20th century is *very likely* due to the observed increase in anthropogenic [caused by human activity] greenhouse gas concentrations" and that carbon dioxide (CO_2) from fossil fuel use accounts for 56.6% of global anthropogenic greenhouse gas emissions [2]. The risks of global warming include increased droughts, floods/loss of coastal area, heat waves, and species extinction [2]. In addition to the serious threat of global warming, numerous studies have shown that air pollution is positively associated with excess deaths. One study found that air pollution causes over 40,000 deaths per year in Austria, France, and Switzerland, and that half of those deaths can be attributed to motor vehicles [3]. Cleary, the reduction in burning of fossil fuels through the widespread use of zero-emission vehicles, such as fuel cell vehicles, can have a positive impact on the health of the earth and mankind.

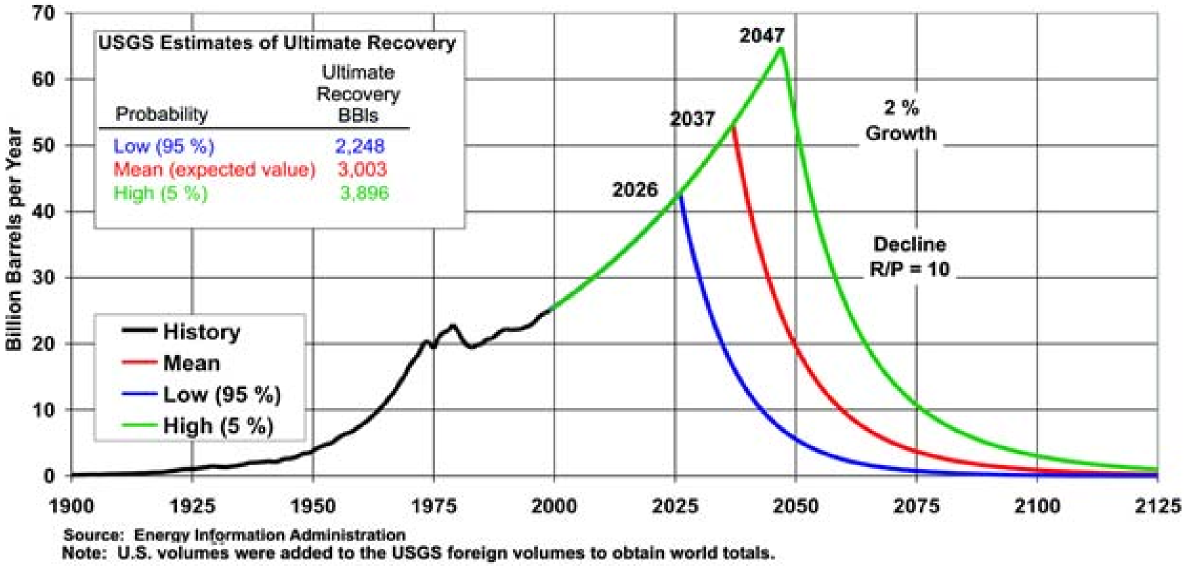

Source: Energy Information Administration
Note: U.S. volumes were added to the USGS foreign volumes to obtain world totals.

Figure 1-1: The USGS estimates of ultimate oil recovery [1]

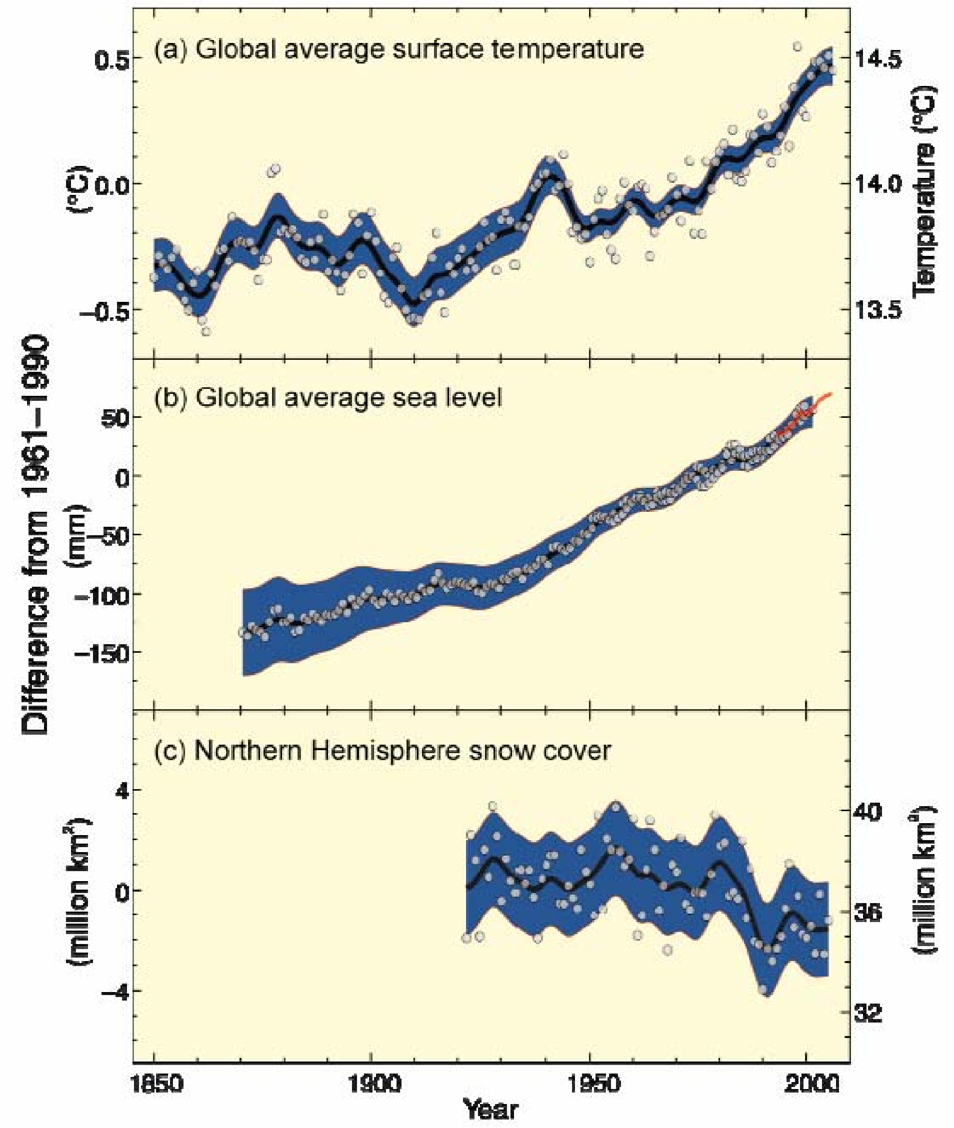

Figure 1-2: Observed changes in (a) global average surface temperature; (b) global average sea level; and (c) Northern Hemisphere snow cover for March-April (All differences are relative to corresponding averages for the period 1961-1990. Smoothed curves represent decadal averaged values while circles show yearly values.) [2]

All options for replacing the ICE vehicle are currently plagued with some sort of problem or obstacle. The gasoline-hybrid-electric vehicle [4] is an important step towards reducing oil use and emissions. Yet, it is not an adequate long-term solution, as it does not eliminate these problems. Vehicles that run on biodiesel are another alternative; however, they only reduce, not eliminate most emissions, and actually increase the emission of NOx [5]. Furthermore, production of biodiesel uses up other finite resources such as farmable land and fresh water. Electric vehicles [4] eliminate oil use and emissions, provided the electricity used to charge the battery is generated by renewable and clean sources, such as wind, solar, or geothermal. Yet, battery advancements to date have not been able to provide electric vehicles with the power, energy storage, and quick refuelling capabilities needed to satisfy consumers. Although future developments in battery technology may make electric vehicles an ideal choice for city driving, another vehicle option is needed to provide all-around performance in terms of range, quick refuelling, and zero harmful emissions.

Fuel cell vehicles have the potential to address all of the problems surrounding the ICE vehicle, while offering the consumer no significant sacrifice in performance or driving range. Also, fuel cell vehicles, which run on hydrogen, could help the energy sector move to a more decentralized hydrogen economy, where all people have the opportunity to be both a producer and user of energy [6]. While most major automotive companies are investing in the commercialization of fuel cell vehicles [7], many challenges remain in getting fuel cell vehicles on the road. These issues, as well as the history of fuel cell vehicles, are discussed in Section 1.3, but first, an introduction to fuel cells is given in Section 1.2.

1.2 Background Information

1.2.1 Fuel Cells

A fuel cell is an electrochemical energy conversion device, which, unlike a battery, can continuously provide electricity as long as a fuel, such as hydrogen, is continuously supplied. This thesis will focus on the Polymer Electrolyte Membrane Fuel Cell (PEMFC), as this type runs at a relatively low temperature, has a short start-up time, and has a high power density [8], making it best suited to vehicular applications.

Figure 1-3 [9] shows a diagram of a PEMFC. The main components are the anode, cathode, electrolyte, and catalyst. The catalyst is carbon paper or cloth with a thin coating of platinum powder. The purpose of the catalyst is to facilitate the reactions at the anode and cathode. The anode conducts the electrons that are freed from the hydrogen fuel so that they can be used in an external circuit. It has channels etched into it that disperse the hydrogen gas evenly over the surface of the catalyst. The electrolyte is a proton exchange membrane, which blocks electrons and only conducts positively charged ions. The cathode has channels etched into it that distribute the oxygen evenly over the surface of the catalyst. It also conducts the electrons back from the external circuit to the catalyst, where they can recombine with the hydrogen ions and oxygen to form water. The result of the reaction is water and heat. The chemical reactions are given by Equations (1-1) to (1-3).

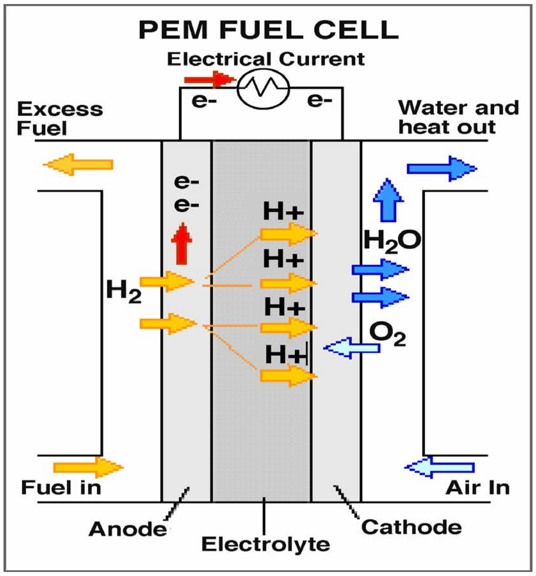

Figure 1-3: PEMFC diagram [9]

Anode side: $\mathbf{2H_2 \Rightarrow 4H^+ + 4e^-}$ **(1-1)**

Cathode side: $\mathbf{O_2 + 4H^+ + 4e^- \Rightarrow 2H_2O}$ **(1-2)**

Net reaction: $\mathbf{2H_2 + O_2 \Rightarrow 2H_2O}$ **(1-3)**

As shown in Figure 1-4 [10], fuel cells exhibit quite high efficiencies, compared to the traditional internal combustion engine, which has an average thermal efficiency of 30-35% [8]. The efficiency versus power curve is important when developing a drive train topology and control strategy for a fuel cell vehicle. Also, the voltage-current (V-I) curve of the fuel cell, shown in Figure 1-5 [8], gives important information regarding how the voltage of the fuel cell stack varies with the output current. For each type of voltage drop, Figure 1-5 shows the cause for the loss. Activation loss is associated with the slow rate of the electrochemical reaction [8]. Resistive loss occurs due to the resistance to the flow of ions in the electrolyte and to the flow of electrons through the electrode materials [8]. Concentration loss is caused by consumption of reactant at the electrode by the reaction, leading to loss of potential due to the inability of the surrounding material to maintain the initial fluid concentration [8].

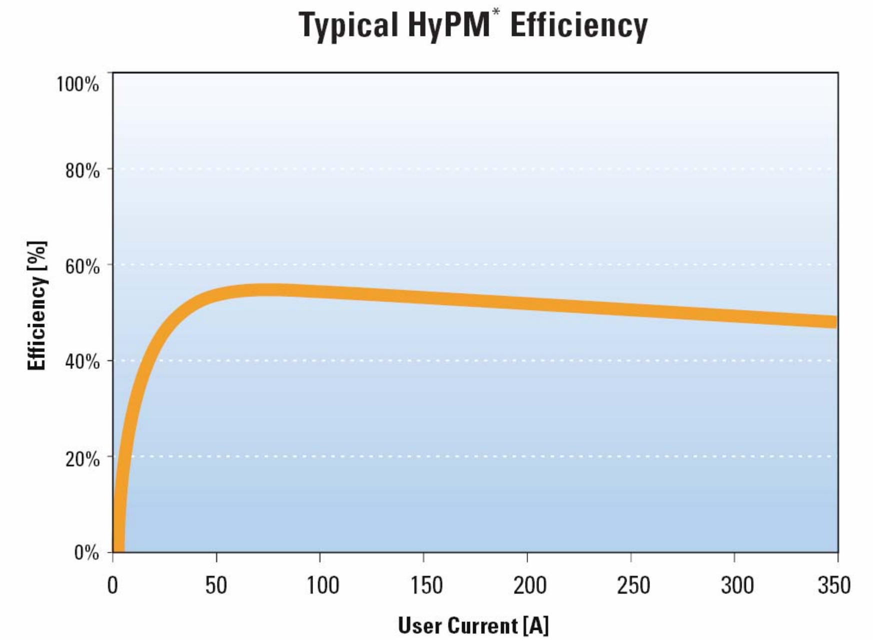

Figure 1-4: Hydrogenics HyPM fuel cell efficiency curve [10]

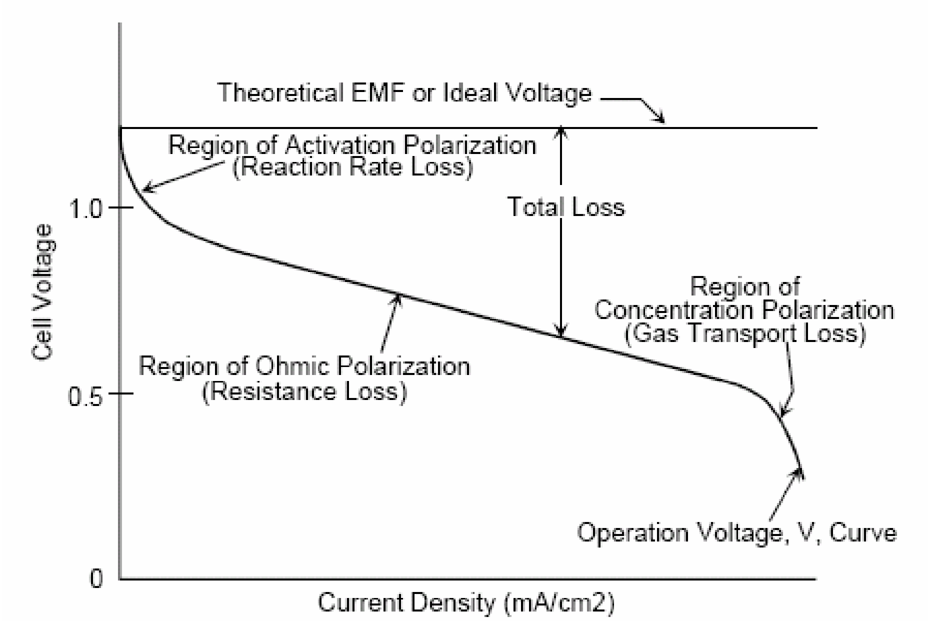

Figure 1-5: Typical voltage vs. current curve for a fuel cell [8]

The history of fuel cells begins in 1839 with Sir William Grove. His experiment was to attempt to reverse the process of electrolysis (the splitting of water into hydrogen and oxygen using electricity), but he was not very successful because not enough was known about electricity at the time. Dr. Francis Thomas Bacon initiated work on an alkaline fuel cell system in the 1930s and by 1952, construction and testing of a 5-kW alkaline fuel cell was completed [8]. The late 1950s and early 1960s brought on the first boom in fuel cell use due to the American space program. Space shuttles required portable power but suitable options were slim: nuclear power was seen as being too dangerous, solar arrays were too bulky and expensive, and batteries were too heavy. Fuel cells met the needs well, and were further developed for use in the Apollo space vehicle [8].

Due to renewed interest in fuel cell vehicles after the 1973 oil embargo, much research and development has been devoted to improving the performance of fuel cells and reducing their cost. The US Department of Energy presents in its "Hydrogen, Fuel Cells, and Infrastructure Technologies: Development and Demonstration Plan", industry targets for fuel cell durability, performance, and cost. Ballard, a leading Canadian fuel cell company, has focused on four important areas of research in order to meet or exceed these industry targets: (i) durability (completed 2000 hours or 100,000 kilometres of real drive cycle testing), (ii) power density, (iii) freeze start capability (achieved start-up from -30°C in 195 seconds), and (iv) stack cost [11].

1.2.2 Fuel Cell Vehicles

The development of one important aspect of the fuel cell vehicle, the electric motor, dates back to the early 19th century. Although electric vehicles were a strong contender in the early 20th century to become a mainstream transportation method, the ICE vehicle eventually won out due to the short range and high cost of electric vehicles. Also, the discovery of Texan oil reduced the price of gasoline so that it was affordable to the average consumer. Thus, fuel cell and electric vehicles took a backseat to the ICE vehicle for the majority of the last 100 years.

The oil embargo in 1973 kick-started renewed interest in fuel cell power for personal transportation applications as governments looked to reduce their dependence on petroleum imports. The 1970s also brought increasing concern over the environmental effects of ICE vehicles. Companies and government organizations began working on improving fuel cell technology throughout the 1970s and 1980s.

In the early 1970s, K. Kordesch modified a sedan to operate from a 6-kW fuel cell and a lead-acid battery pack. The car was driven on public roads for about three years [8]. In 1993, Ballard launched a fuel cell-powered light-duty transit bus using a 120-kW fuel cell system, followed by a heavy-duty transit bus using a 200-kW fuel cell system in 1995 [8]. In 1994 and 1995, H-Power built three fuel cell-battery hybrid buses, each using a 50-kW fuel cell and a 100-kW nickel-cadmium battery [8]. The importance of these releases was to make fuel cell technology visible and understandable to key decision makers in government and industry. These buses helped to prove that fuel cells would work in the real world. Fleet-vehicle operations, such as buses and delivery services, are seen as early adopters of fuel cell technology due to the ease of centralized refuelling and the reduced requirement for a high range capability between fill-ups. Trials of fuel cell powered buses have taken place in Chicago and Vancouver as well as in other cities in North America and Europe.

Today, most major automotive manufactures have developed prototype fuel cell vehicles, and a comprehensive review of these vehicles can be found in [7]. In July 2005, the first fuel cell vehicle was leased to a family in California [12], as an important step in getting more fuel cell vehicles on the road. However, many obstacles still remain before the fuel cell vehicle can become a mainstream form of transportation.

An obvious issue is the need for a hydrogen infrastructure to enable refuelling of the vehicles. However, hydrogen filling stations currently exist in many countries around the world, such as Canada, the USA, Iceland, Japan, Singapore, and Germany. Though these stations are currently not widespread enough to allow large numbers of people to begin driving fuel cell vehicles, it is expected that more hydrogen infrastructure will be built as more fuel cell vehicles become commercially available. Another option is to use electrolysis at refuelling stations to convert electricity from the grid into hydrogen. This idea can be extended so that people would actually have an electrolyzer in their homes, to provide hydrogen to fill up at home [6]. The obstacles associated with developing an adequate hydrogen infrastructure brings up another important question: Where will the hydrogen come from?

Although hydrogen is the most abundant element in the universe, it rarely exists alone in nature. Today, hydrogen is mostly produced by reforming natural gas. In this way, pollutants can be captured if the reforming is done at a central plant. However, other options, such as direct solar hydrogen from methane at land fills [13], and hydrogen from bacteria [14], are continually being explored. If electrolysis is used to generate hydrogen, there may have to be an increase in electricity generation to satisfy the need for hydrogen, though the increase may be small, since hydrogen can be produced during off-peak times (e.g., overnight). Methods to generate electricity which have a minimal impact on the environment include: nuclear, wind, solar, hydro, and geothermal. It is often said that at the beginning of the hydrogen economy, most of the hydrogen will still be reformed from natural gas, but as time goes by, society will move towards more ideal sources of energy, such as wind and solar [6]. Therefore, although generation and transportation of hydrogen is a major issue in the deployment of fuel cell vehicles, many diverse ideas are being developed to solve the problem.

Other obstacles for fuel cell vehicles include improving on-board hydrogen storage, improving fuel cell and battery durability, and increasing the efficiency and performance of a fuel cell vehicle. The last barrier to commercialization is cost, a true challenge as fuel cells are still extremely expensive today. Also, many parts used to work with fuel cells (e.g., power electronic converters) must be custom-made and can thus be very expensive. However, these costs will decrease as technological processes improve, and components are mass-produced.

1.3 Research Objectives and Contributions

Though there are currently a number of obstacles to attaining widespread proliferation of fuel cell vehicles, the fundamental concept of the fuel cell vehicle is strong: it is efficient, emits zero harmful emissions, and the hydrogen fuel can be produced from different renewable sources. Therefore, research on fuel cell vehicle design is imperative in order to improve vehicle performance and durability, increase efficiency, and reduce costs. These improvements can help push forward the widespread transition from ICE vehicles to fuel cell vehicles. In this thesis, the following contributions are made to the advancement of fuel cell vehicle design:

1) A novel battery-ultracapacitor energy storage system topology for use in fuel cell vehicles, which exhibits higher efficiency, lower cost, and lower mass than other battery-ultracapacitor topologies presented in the literature, while maintaining similar performance.

2) General conclusions for optimal topologies, as well as component types and sizes, for a fuel cell vehicle resulting from a parametric study using a custom-made vehicle simulator.

3) An analytical method to optimize the novel battery-ultracapacitor energy storage system based on maximizing efficiency, and minimizing cost and mass. This method can be applied to any system utilizing the novel battery-ultracapacitor energy storage system and is not limited to application in fuel cell vehicles alone.

4) A novel soft-switching method, the capacitor-switched regenerative snubber, for the high-power DC/DC boost converters commonly used in fuel cell vehicles. This circuit increases the efficiency and reduces the overall mass of the DC/DC boost converter.

Hence, the main goal of this thesis is to provide new ideas to improve the design of fuel cell vehicles in the areas of powertrain topologies, energy storage systems, and power electronic converters.

1.4 Thesis Organization

This thesis is organized into seven chapters and one appendix. Chapter 1 has given an introduction to fuel cells and fuel cell vehicles, as well as motivation for fuel cell vehicle research. Chapter 2 performs a literature review on fuel cell vehicle powertrain topologies, discusses the advantages and disadvantages of using different energy storage systems types (battery, ultracapacitor, and combined battery-ultracapacitor), and gives an analysis of the numerous powertrain topologies available for each energy storage system type. Chapter 2 also presents the novel battery-ultracapacitor topology for fuel cell vehicles.

Chapter 3 discusses the development of the hardware and control method used in a 65-kW DC/DC boost converter built for use in a fuel cell vehicle. The results are used to aid in modeling of the DC/DC converters in the vehicle simulator built in Chapter 4.

Chapter 4 presents the modeling details of a vehicle simulator created in MATLAB/Simulink with the purpose of performing fuel cell vehicle optimizations through a comprehensive parametric study. The results provide general conclusions regarding optimal fuel cell size, energy storage system type, and powertrain topology.

In Chapter 5, an analytical method is derived in order to perform an optimization of the novel battery-ultracapacitor topology presented in Chapter 2 and simulated in Chapter 4. The method uses several inputs to calculate the optimal sizes of the battery and ultracapacitor based on maximizing efficiency, and minimizing cost and mass.

One or more high-power DC/DC boost converters are commonly required within a fuel cell vehicle powertrain. Chapter 6 presents a novel capacitor-switched regenerative snubber which is shown to increase the efficiency and decrease the mass of the boost converter. Lastly, conclusions and suggestions for future work are presented in Chapter 7. Appendix A provides photographs of the laboratory prototypes built for the experimental study and evaluation of the capacitor-switched regenerative snubber presented in Chapter 6.

Chapter 2

Energy Storage Systems and Powertrain Topologies for Fuel Cell Vehicles

2.1 Introduction to Energy Storage Systems for Fuel Cell Vehicles

In order to attain the goal of designing a fuel cell vehicle with high efficiency, high performance, high durability, and low cost, numerous design decisions must be made. This thesis focuses on design decisions for the powertrain from the fuel cell power source to the high-voltage bus connected to the inverter and motor. The design decisions generally include the choice of the type of component as well as how to connect the powertrain components, which is referred to as the powertrain topology. This chapter specifically focuses on the choice of energy storage system (ESS) type, and the related choices for powertrain topologies for each ESS type.

It is important to hybridize a fuel cell vehicle using an ESS for the following reasons:

(1) To enable recovery of regenerative braking energy, thus increasing the overall efficiency of the vehicle. Regenerative braking energy is the captured kinetic energy that would otherwise be lost if an electric motor/generator, a bidirectional converter, and an ESS were not used. The ESS stores this captured energy to be used during the next acceleration, or whenever else needed.

(2) To provide fast and additional power during peak demand periods such as acceleration. It should be noted that the fuel cell has a time-delayed response, and is limited in power output.

(3) To reduce the size of the fuel cell. A fuel cell of lower rated power can be significantly lighter and cheaper than a fuel cell of higher rated power. Thus, adding an ESS is also a cost-

reduction method, since ESS components are generally cheaper than fuel cells on a per-kilowatt basis.

(4) To allow a control strategy to be implemented to ensure the fuel cell operates more often in the high-efficiency region.

The most common choices for an ESS are batteries and ultracapacitors [15]. A battery is a device which stores and releases energy via an electrochemical process, whereas ultracapacitors store and release energy via an electrostatic field. For purposes of energy storage in a hybrid vehicle, the main distinction between the two energy storage elements is that batteries have higher specific energy and ultracapacitors have higher specific power, higher efficiency, and a longer lifetime in terms of charge/discharge cycles [15]. Figure 2-1 shows the specific power and specific energy for some commercially-available batteries [16][17][18], and an ultracapacitor [19]. The specific power for a commercially-available fuel cell is also shown for comparison purposes [11]. It can be concluded that the lithium-ion batteries and the ultracapacitor are far superior to fuel cells in terms of specific power. It can also be seen that high-power lithium-ion batteries are closing the gap in specific power between other battery types and ultracapacitors. However, other issues related to the lithium-ion battery, such as safety and durability, must be considered when comparing them with ultracapacitors, and this will

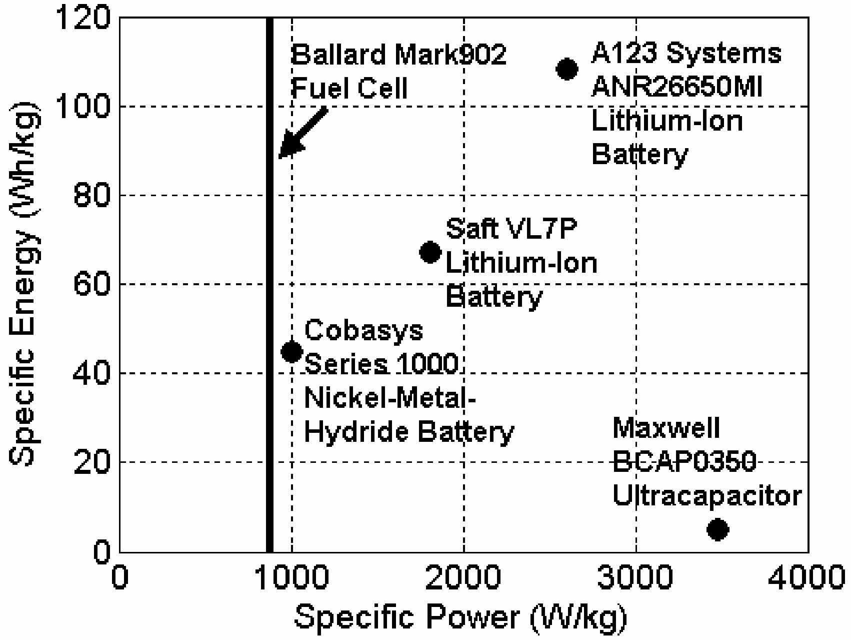

Figure 2-1: Specific energy and specific power for various commercially-available power sources

be discussed further in future sections. This thesis will investigate the use of a battery ESS, an ultracapacitor ESS, and a combined battery-ultracapacitor ESS. In general, for energy storage:

(1) The maximum power output should be enough to compensate for the difference between the fuel cell power and the forecasted maximum power required by the vehicle.

(2) The energy content should be enough to avoid complete discharge during any high-power-demand period.

The issues that must be considered when choosing an ESS for a fuel cell vehicle are: positive and negative power capability, energy storage capability, cost, mass, durability, efficiency, and simplicity of interconnection. However, energy storage system cost is a difficult parameter to quantify. Some manufacturers are careful to keep their product costs unavailable to the public, and if they are made available to certain individuals, then the information is strictly confidential. This rationale is understandable because many of these cutting-edge technologies are currently very high-cost, and more development, as well as mass production, will bring the costs downs in the future. Also, if only low-volume costs are available, then estimation must be used to obtain a reasonable high-volume cost. Furthermore, since the cost of certain technologies may drop faster than that of others in the future, this thesis focuses firstly on the technical feasibility of the ESS, and considers the estimated costs to be of secondary importance. A detailed analysis of energy storage system costs is presented in Chapter 4.

The main goal of Chapter 4 is to provide a fair comparison of all fuel cell vehicle topologies using quantitative results from a vehicle simulator. However, since it is unrealistic to simulate every possible powertrain topology, the remainder of Chapter 2 uses qualitative analysis to determine the most promising topologies for a battery ESS, an ultracapacitor ESS, and a combined battery-ultracapacitor ESS. These most promising topologies are simulated and analyzed further in Chapter 4.

2.2 Fuel Cell Connection Topologies

In general, there are three topologies that can be used to connect the fuel cell to the main high-voltage bus, as shown in Figure 2-2. Topology (a) [20][21][22] connects the fuel cell to the high-voltage bus through a boost (step-up) DC/DC converter, topology (b) [23] connects the fuel cell to the high-voltage bus through a buck (step-down) DC/DC converter, and topology (c) [20][22][24] connects the fuel cell directly to the high voltage bus.

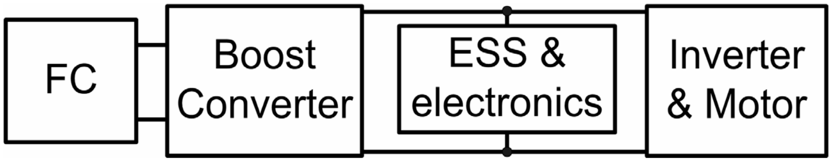

(a) Boost converter [20][21][22]

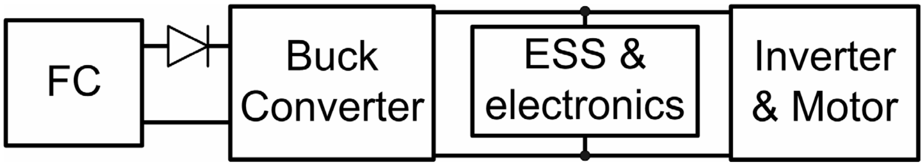

(b) Buck converter [23]

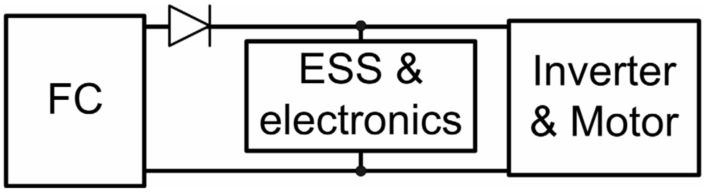

(c) Direct connection [20][22][24]

Figure 2-2: Fuel cell connection topologies

Before comparing the three topologies, it is important to note the following:

(1) It is generally advantageous to operate the inverter and motor at high-voltage/low-current rather than at low-voltage/high-current to minimize I^2R losses for a given output power. For the same reasons, a high-voltage ESS can output a given power more efficiently than a low-voltage ESS. Thus, in order to achieve the goal of high efficiency, a relatively high-voltage bus as well as a high-voltage inverter and motor are assumed to be used. A common inverter and motor voltage range in industry is 250V – 425V [25], and this range will be used throughout the thesis.

(2) Fuels cells are known to be relatively low-voltage/high-current power sources. The voltage of each cell can drop significantly at high power (as shown in Figure 1-5) and many cells are connected in series to form a high-voltage, high-power fuel cell stack. For example, the Hydrogenics HyPM HD65 stack has a voltage range of 218V – 305V, maximum current of 300A, and maximum power of 65.5 kW [10]. Ballard's Mark902 stack has minimum voltage of 284V, maximum current of 300A, and maximum power of 85kW [11]. In general, the minimum voltage (the stack voltage at maximum power) is higher for a higher-power fuel cell module.

(3) Today, and in the foreseeable future, fuel cells are the most costly source of power in the vehicle (compared to batteries and ultracapacitors). This will be quantified in Chapter 4.

Thus, the major advantage of topology (a) is that a smaller and thus cheaper fuel cell may be used because the minimum fuel cell voltage can be below the minimum voltage of the inverter. The boost DC/DC converter steps-up the fuel cell voltage to match that of the high-voltage bus, and thus the fuel cell size can be chosen based on the optimal power level and cost, rather than based on meeting a high voltage requirement. Since high cost is a major obstacle to the commercialization of fuel cell vehicles, this significant opportunity to reduce cost should not be overlooked. In addition, the boost converter, shown in Figure 2-3(a) has a built-in diode to prevent reverse current into the fuel cell, which the buck converter, shown in Figure 2-3(b) does not. Thus, in topologies (b) and (c) of Figure 2-2, an extra diode must be added to prevent reverse fuel cell current, causing some additional losses.

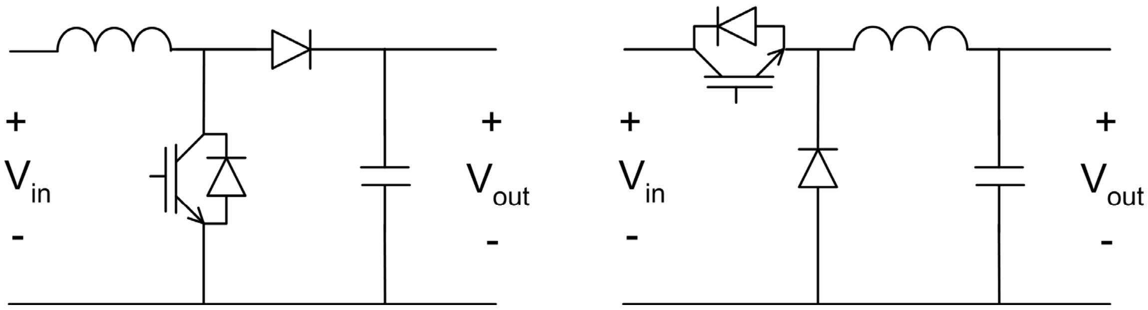

(a) Boost converter

(b) Buck converter

Figure 2-3: Boost and buck DC/DC Converters

The advantage of topology (b) of Figure 2-2 is that buck converters are generally more efficient than boost converters, though the exact efficiency improvement depends on the specific converter design and voltage step-up/step-down requirements. However, the need for an additional diode to prevent fuel cell reverse current will add losses to topology (b), reducing or possibly nullifying the efficiency advantage of the buck converter over the boost converter. The main disadvantage of topology (b) is that a larger fuel cell must be used, so that the minimum stack voltage (which is attained at maximum power) is higher than the minimum inverter voltage (e.g., 250V). For example, the Honda FCX fuel cell vehicle uses topology (b) [23] and a 78-kW fuel cell for a relatively small passenger vehicle. A larger fuel cell adds significant mass (which in turn reduces fuel economy) and cost to the vehicle.

The advantage of topology (c) is that since there is no DC/DC converter in the fuel cell power path, the only losses are from the diode, which is needed to prevent reverse fuel cell current. Thus, topology (c) is the most efficient option for providing fuel cell power to the inverter. However, this must be weighed against the higher mass and cost of a larger fuel cell required to meet the high-voltage requirements of the inverter and motor. Also, the instantaneous fuel cell voltage dictates the bus voltage, meaning that all ESS components (batteries and/or ultracapacitors) must be connected to the bus through DC/DC converters if independent control of all power sources is desired. Thus, the efficiency gain due to elimination of the DC/DC converter of the fuel cell may be traded for efficiency losses in DC/DC converters for the ESS components (to be further discussed in Sections 2.3-2.5). Similarly, the mass and cost savings of not using a DC/DC converter after the fuel cell may be nullified by the mass and cost of a DC/DC converter used with an ESS component.

The preceding qualitative analysis supports the conclusion that in order to minimize vehicle cost, the best option is to connect the fuel cell to the high-voltage bus through a boost converter, so that fuel cell size can be minimized (while still providing adequate base power for the specific vehicle platform). Furthermore, there are efficiency consequences for each topology, and the boost converter option has approximately the same efficiency compared to the other topologies when the entire system (extra diodes required for topologies (b) and (c) and an extra DC/DC converter required for an ESS component for topology (c)) is considered. Thus, the ensuing analysis of ESS types and topologies will assume the fuel cell is connected to the high-voltage bus through a boost converter.

2.3 Battery ESS Topologies

As can be seen in Figure 2-1, A123 Systems' ANR26650MI lithium-ion cell offers very good specific power and specific energy [18]. Thus, lithium-ion batteries, and A123 Systems' cell in particular, will be used for the ensuing qualitative analysis and the quantitative analysis in Chapter 4, as lithium-ion batteries are currently considered the best choice for hybrid-vehicle applications. The interest of industry in lithium-ion batteries for automotive use is clearly demonstrated by the recent announcement by General Motors that it is partnering with A123 Systems to co-develop lithium-ion batteries for the new Chevrolet Volt [18].

A lithium-ion battery consists of two electrodes (the anode and the cathode) separated by a polymer film (to prevent contact and short circuits) and surrounded by an ion-rich solution, the electrolyte. When an external circuit is connected across the electrodes, the electric potential inherent across the cell pulls the ionized lithium elements from the anode through the electrolyte and polymer film towards the cathode. Ions arriving at the cathode give up electrons and the electrons flow through the external circuit, producing current in the opposite direction. The anode is typically made of graphite, but the cathode composition varies widely. A123 Systems' lithium-ion cell uses a new iron phosphate cathode with nanostructures which appears to offer superior safety, higher power, and longer life than earlier generations of iron phosphate cells [18].

Due to the higher specific energy of batteries compared to ultracapacitors, it is advantageous for a fuel cell vehicle to use a battery ESS for the following reasons:

(1) Extra power is available for longer periods of time, which is useful during demanding driving tasks, such as towing a load up an incline or passing at high speeds.

(2) The extra energy required for a hard acceleration can generally be provided by batteries for less cost and mass than by ultracapacitors (to be quantified in Chapter 4).

(3) During low-power demands, the battery can be used to propel the vehicle if the fuel cell would be operating in a very low-efficiency region. This control method can be used to improve the overall efficiency of the vehicle.

The disadvantages of using a battery ESS are as follows:

(1) Higher losses than ultracapacitors during charging and discharging due to higher internal resistance and columbic losses. Columbic losses are due to undesired side reactions

occurring within the cell and columbic efficiency is the ratio of the discharge capacity to the ratio of the charge capacity. These higher losses indicate that a larger and more costly cooling system may be required.

(2) Shorter lifetime in terms of charge/discharge cycles than ultracapacitors.

(3) Lower specific power compared to ultracapacitors. This is especially apparent when comparing maximum charge rates of batteries and ultracapacitors. Batteries have a much lower safe charge rate and hence usually capture less regenerative braking energy than ultracapacitors, which negatively affects the overall vehicle fuel economy.

(4) Safety Issues: more safety problems exist for larger lithium-ion batteries designed for electric vehicle use than with the lithium-ion batteries used in smaller consumer products. Most concerning, overcharging can lead to thermal runaway [26]. Extra electronics are generally required to provide overcharge and short circuit protection [26]. However, advances in battery design, as seen in A123 Systems' cells, offer the possibility of improving the safety of lithium-ion batteries.

(5) More complicated control and monitoring may be required since the battery state-of-charge (SOC) cannot be accurately determined by its terminal voltage, unlike ultracapacitors.

Two battery ESS topologies, shown in Figure 2-4, are compared qualitatively in order to choose the topology to be modeled and simulated for the quantitative comparison of ESS options. For topology (b), a two-quadrant DC/DC converter generally suffices, since the battery voltage can be chosen to be either higher or lower than the high-voltage bus and thus power from the battery would always require either a step-up or a step-down in voltage. Since it has been established that it is advantageous to use a relatively high voltage level at the main bus, it is common to choose the battery to have a lower voltage than the bus, and this will be assumed henceforth.

The main disadvantage of topology (b) is that the second high-power DC/DC converter used to connect the battery to the high-voltage bus adds significant mass and cost to the vehicle powertrain. This means that for the same amount of ESS power required, the ESS system (battery only) shown in topology (a) will be cheaper and smaller than the ESS system (battery + DC/DC converter) shown in topology (b). Furthermore, the losses from the bidirectional converter will decrease the efficiency of the battery charge and discharge cycles. However, a possible advantage for topology (b) arises if the maximum ESS power required is relatively small (based on the type and size of the vehicle and the size of the fuel cell), because a large number of battery cells in series to reach the voltage of the high-voltage bus in topology (a) may be unwarranted. In this case, mass and cost may be able to be saved with topology (b) if only a small amount of battery power is required. However, this is a specific case, and in most cases, especially when a relatively small fuel cell size has been chosen to reduce costs, the high power achieved by using a high-voltage battery (topology (a)) is much needed.

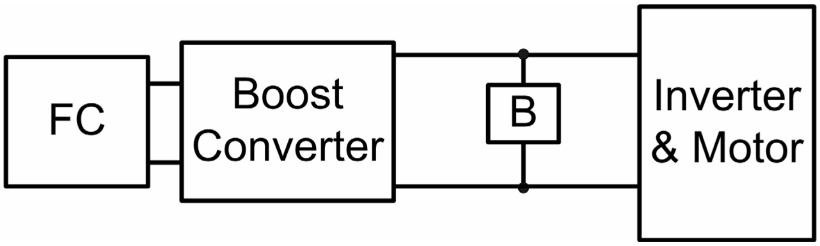

(a) Direct connection [21]

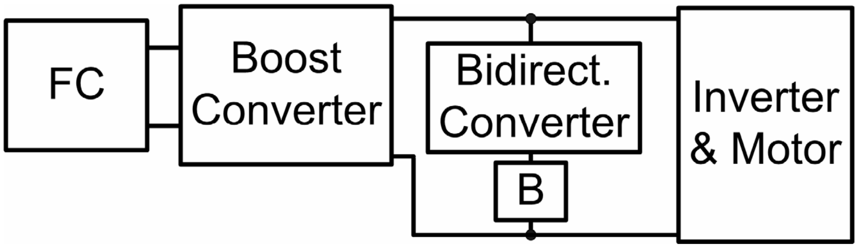

(b) Connection through bidirectional DC/DC converter [22]

Figure 2-4: Two topology options for a fuel cell-battery (FC-B) powertrain

It is also important to note that both topologies provide full control of both the fuel cell and the battery power. In topology (a), the battery power is simply the difference between the motor power required and the power requested out of the fuel cell boost converter. Thus, the analysis and comparison shows that in most cases, topology (a) will be the better topology choice for a battery ESS since the extra mass, cost, and losses of a second DC/DC converter can be saved. Therefore, the battery ESS quantitative analysis in Chapter 4 will use topology (a), i.e., the direct connection of the battery to the high-voltage bus.

2.4 Ultracapacitor ESS Topologies

Ultracapacitors are composed of two electrodes, the positive and negative plates, separated by a thin dielectric. When voltage is applied across the electrodes, an electric field builds up between the plates and electrons are removed from the positive plate and deposited on the negative plate. Energy, E, is stored in the electric field according to the equation

$$E = \frac{1}{2} C V^2 \qquad \textbf{(2-1)}$$

where C is the capacitance in farads and V is the cell voltage in volts. Since the capacitance is proportional to the area of the plates, ultracapacitors are made to have much larger surface areas than traditional capacitors, which leads to their comparatively high energy density. A common approach is to coat the electrodes with activated carbon, which is chemically etched to produce many holes through the material, making the interior surface area about 100,000 times larger than the outside [27]. New methods, such as using carbon nanotubes, further increase the interior surface area, offering the promise of even higher energy density for ultracapacitors in the future [27].

The ultracapacitor ESS analysis will be based on Maxwell Technologies' 350-F cell [19], as it offers high specific power and is easily configurable due to its small size. The advantages of using an ultracapacitor-based ESS in a fuel cell vehicle are:

(1) Longer life expectancy than batteries in terms of charge/discharge cycles.

(2) Higher specific power than batteries, specifically in the ability to accept higher power during charging (resulting in more complete handling of the frequent charge/discharge cycles during regenerative braking and motoring modes of operation).

(3) Higher efficiency than batteries due to lower internal resistance (thus also generating less heat than batteries).

(4) Can generally operate over a wider temperature range than batteries [27].

(5) Since stored energy is expressed by Equation (2-1), the ultracapacitor SOC can be determined from the voltage, enabling the control system to be simplified.

Due to the comparatively low energy-storage capability of ultracapacitors, the following disadvantages are associated with an ultracapacitor ESS:

(1) Depending on the size of ultracapacitor bank used, there may not be enough extra energy available to complete all demanding driving tasks, especially at high speeds. Since energy from the ultracapacitor is used in the acceleration to attain high speeds, the ultracapacitor may get significantly depleted, and require a regenerative braking event to re-charge. Thus, if extra energy (e.g., for passing or driving up a large incline) is required at high speeds, the ultracapacitor may not be able to provide that energy.

(2) The ultracapacitor ESS does not provide enough energy to propel the vehicle when the fuel cell is operating at low efficiency (i.e., at low speeds).

Three ultracapacitor ESS topologies, as shown in Figure 2-5, are compared qualitatively in order to choose the topology to be modeled and simulated for the quantitative comparison of ESS options in Chapter 4.

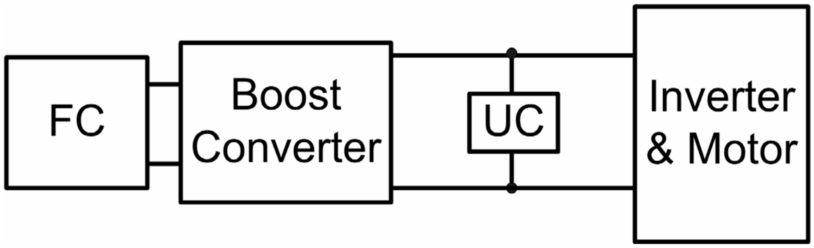

(a) Direct connection to high-voltage bus [23]

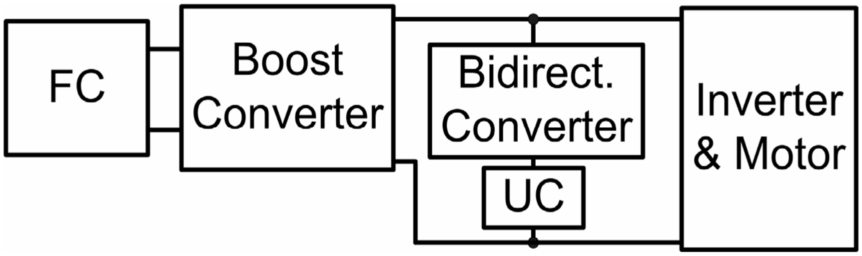

(b) Connection through bidirectional DC/DC converter [28]

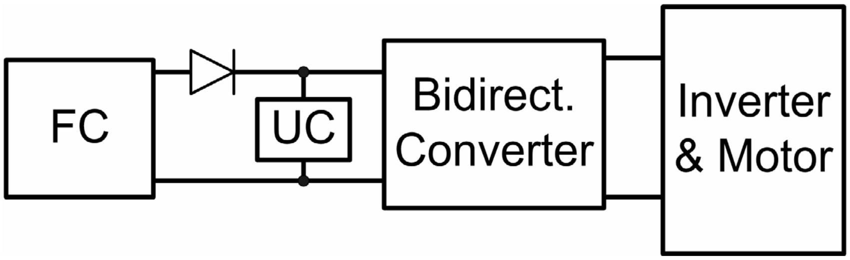

(c) Direct connection to low-voltage fuel cell bus [29]

Figure 2-5: Three topology options for a fuel cell-ultracapacitor (FC-UC) powertrain

The comparison between ultracapacitor topologies (a) and (b) is similar to the comparison between the two battery ESS topologies of Figure 2-4; i.e., topology (b) has the additional mass, cost, and losses of a second high-power DC/DC converter, while offering no control advantage because the ultracapacitor power can be indirectly controlled in topology (a). However, a new facet that is unique to the ultracapacitor ESS is the voltage swing limits of the ultracapacitor as it is charged and discharged. For topology (a), the energy available from the ultracapacitor is limited by the fact that the voltage swing of the high-voltage bus is limited (i.e., to 250V-425V). From this point of view, topology (b) could be seen to have an advantage because the bidirectional DC/DC converter allows the ultracapacitor voltage to swing lower than the minimum bus voltage, and hence more energy may be available. However, this must be weighed with the fact that for high power requirements (which are a common requirement for any ESS), a low ultracapacitor voltage could lead to prohibitively high currents. These high currents would contribute to more I^2R losses, could reach the safe upper limit for the current of a particular ultracapacitor, and would require a very large bidirectional DC/DC converter capable of handling such high currents. Thus, the prospect of accessing more of the ultracapacitors' stored energy by using topology (b) may be of little practical value for many systems.

Topology (c) makes use of the fact that the ultracapacitor voltage varies in a similar manner to the fuel cell voltage (high voltage at low power or the beginning of an acceleration and low voltage at high power or the end of an acceleration) and uses a parallel fuel cell-ultracapacitor connection. A diode is required after the fuel cell to prevent reverse fuel cell current when regenerative braking is occurring, which contributes to a relatively small amount of loss from the fuel cell output power. Topology (c) uses only one DC/DC converter, similar to topology (a) and fewer ultracapacitor cells may be used to reach the lower-voltage fuel cell bus. However, a major disadvantage of topology (c) is that the DC/DC converter must be sized large enough to process the peak power of the powertrain. This means that the bidirectional converter size could be larger than two times the size of the boost converter in topology (a). Furthermore, the efficiency of the ultracapacitor charges and discharges are reduced compared to topology (a) due to the losses in the large bidirectional DC/DC converter. Therefore, topology (c) results in more losses of ultracapacitor energy, loss of independent control of the fuel cell power and ultracapacitor power, and an increase in the size of the power electronic converter required compared to topology (a). It can also be noted that similar to topology (b), the lower-voltage ultracapacitor bank in topology (c) would lead to higher ultracapacitor currents for a given ESS power requirement compared to topology (a).

The preceding analysis shows that the simple connection of the ultracapacitor bank to the high-voltage bus is the most promising ultracapacitor topology in general, as it eliminates the need for a larger or second DC/DC converter, is highly efficient, and provides full control of the fuel cell and ultracapacitor power. Further to this point, Honda has actually used this ESS topology in its FCX vehicle with much success [23]. Thus, the quantitative analysis in Chapter 4 will use topology (a), i.e., direct connection to the high-voltage bus, for the ultracapacitor ESS.

2.5 Combined Battery-Ultracapacitor ESS

As discussed in Sections 2.3 and 2.4, batteries and ultracapacitors both offer unique advantages as energy storage systems for fuel cell vehicles. In fact, the high specific power, high efficiency, and long lifetime of ultracapacitors are excellent complements to the high specific energy of batteries. Thus, a combined battery-ultracapacitor ESS has the potential to maximize the advantages of each technology, while minimizing the disadvantages. Recent studies [24][30][31][32][33] have shown that a combined battery-ultracapacitor ESS can provide excellent performance and fuel economy. Furthermore, recent news proves that industry is also very interested in the possibilities of combined battery-ultracapacitor power sources: On November 19, 2007, Maxwell Technologies, Inc. (a leading ultracapacitor manufacturer) and Tianjin Lishen Battery Joint-Stock Co., Ltd., (China's leading producer of rechargeable lithium-ion batteries) announced an alliance to manufacture and market energy storage products combining the companies' respective ultracapacitor and lithium-ion battery technologies [19]. Maxwell's president and chief executive office, David Schramm, states "We believe that the products we envision will give end-users the best of both worlds in terms of the long cycle life, rapid charge/discharge characteristics and low temperature performance of ultracapacitors and the large energy storage capacity of lithium-ion batteries" [19]. The companies plan to develop products for various sectors, including the automotive industry.

Though the idea of a combined battery-ultracapacitor ESS is gaining momentum in industry, challenges remain in designing the combined system using a topology to minimize mass and cost, and maximize efficiency. A combined system is more complicated than a single ESS because more DC/DC converters are usually required to connect the multiple sources. Thus, the remainder of this section reviews four common topologies for a battery-ultracapacitor ESS for fuel cell vehicles from the literature (shown in Figure 2-6) and analyses the advantages and disadvantages of each to find the most promising of these topologies for simulation in Chapter 4. Section 2.6 presents a novel fuel cell-battery-ultracapacitor topology which minimizes many of the disadvantages of the existing topologies.

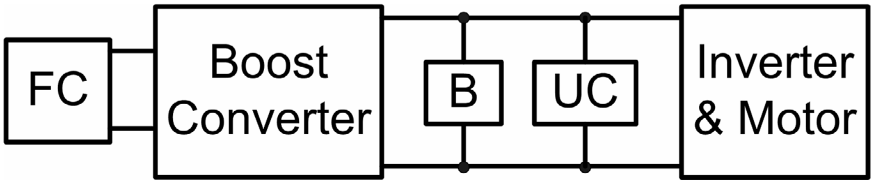

(a) Parallel connection of battery and ultracapacitor to high-voltage bus [34]

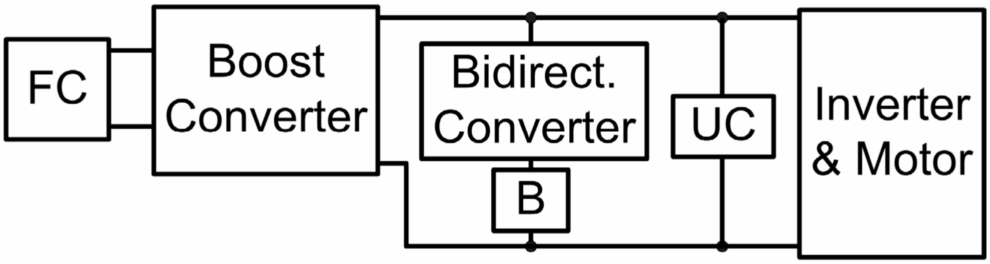

(b) Direct ultracapacitor connection to bus, battery connects through DC/DC converter [35]

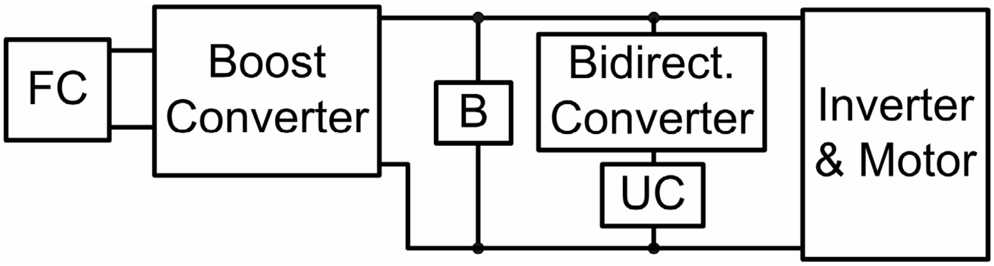

(c) Direct battery connection to bus, ultracapacitor connects through DC/DC converter [36]

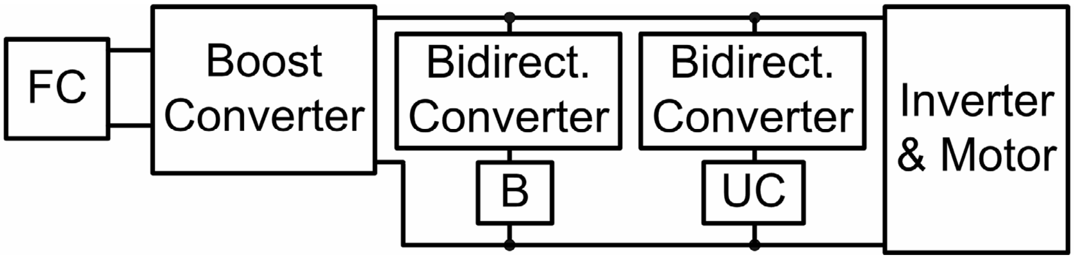

(d) Both battery and ultracapacitor connected to high-voltage bus through DC/DC converters [24][30]

Figure 2-6: Four common topologies for a fuel cell-battery-ultracapacitor (FC-B-UC) powertrain

The parallel battery-ultracapacitor connection shown in topology (a) of Figure 2-6 has been analyzed in [34]. Since both battery and ultracapacitor are directly connected to the high-voltage bus, this topology does not have the extra mass, cost, and losses of the additional DC/DC converter(s) associated with other topologies. Since high-power DC/DC converters add significant mass and cost to the powertrain, this is a large savings for this topology. However, a major disadvantage of this topology is that the power sharing between the battery and the ultracapacitor is determined by their respective internal impedances. In other words, there is no mechanism to separate or control the power flow of each component; so when current flows from the combined ESS, it always flows from both components. A major motivation for combining batteries and ultracapacitors is to extend the battery lifetime by allowing the ultracapacitor to provide more of the high-power ESS requirements. Thus, for the power request profiles typical of a fuel cell vehicle ESS, this topology is not an optimal choice for reducing battery current, because the battery operates as frequently as the ultracapacitor (though the battery root-mean-square (RMS) current is somewhat reduced compared to the battery-only ESS). Furthermore, the ultracapacitors' high specific power cannot be well utilized because the ultracapacitor cannot provide high-power charge or discharges pulses since its voltage swing is limited by the relatively-steady battery terminal voltage.

Topology (b) [35] corrects the main problem with topology (a) because the bidirectional DC/DC converter between the battery and the high voltage bus allows independent control of the battery power. This converter also allows indirect control over the ultracapacitor power, since it is the difference between the power required at the motor inverter and the total power provided by the fuel cell and battery. The disadvantage of this topology is the additional mass, cost, and losses associated with the bidirectional DC/DC converter connected to the battery, which can be significant. Another potential problem with this topology relates to the efficiency of charging the battery. High-power DC/DC converters are usually relatively inefficient at light load. However, charging the battery is relatively inefficient at high currents due to the I^2R losses associated with the battery's internal resistance. In addition, when charging the battery from the fuel cell, the power must flow through two DC/DC converters to reach the battery, which introduces further losses. Thus, from an efficiency point of view, the disadvantage of topology (b) is the relatively low-efficiency charge path from the fuel cell to the battery. However, topology (b) offers a very high ultracapacitor charge/discharge path efficiency since the ultracapacitor is connected directly to the high voltage bus. If a control strategy is implemented to minimize the battery current, then the ultracapacitor will be providing and storing the majority of energy for acceleration and regenerative braking, and thus the high ultracapacitor path efficiency may outweigh the lower battery path efficiency.

Topology (c) [36] uses the same principle as in topology (b) by connecting one ESS component, the ultracapacitor in this case, to the high-voltage bus through a bidirectional DC/DC converter. Thus, it also gives the advantage of full control of the power from each ESS component and the disadvantage of the extra mass, cost, and losses of the extra DC/DC converter. Topology (c) has a relatively high-efficiency charge path for the battery and a relatively low-efficiency charge path for the ultracapacitor, due to the losses from the DC/DC converter. The choice between topology (b) and topology (c) may depend on the size of the battery and ultracapacitor in the proposed design: using the DC/DC converter with the component having lower power rating means the DC/DC converter size and cost can be minimized. However, considering the desired operation of the combined ESS presents another strategy for choosing the superior topology. When the control of the ESS power is considered, it is clear that the ultracapacitor will be used more often to provide fast and large power transients – this control strategy accomplishes the goal of increasing the battery lifetime by using the battery less often. Thus, from this point of view, it would be best to use the bidirectional DC/DC converter with the battery (topology (b)), because the efficiency losses of the DC/DC converter will be minimized since the battery operates much less often than the ultracapacitor.

Topology (d) [24][30] has bidirectional DC/DC converters connected to both the battery and the ultracapacitor. This adds significant mass, cost, and losses to the system. Also, a capacitor must be added to the high voltage bus to provide slack [30], since all four of the components connected to the high voltage bus (three DC/DC converters and the motor inverter) are directly controlled. Topology (d) is generally undesirable due to the extra converter with no significant benefit.

The preceding analysis indicates that both topologies (b) and topology (c) are good possibilities for a battery-ultracapacitor ESS. However, since an important goal of the combined ESS is to use the ultracapacitor often to increase charge/discharge efficiencies and extend battery life, and topology (b) achieves these goals, topology (b) is chosen to be modeled and simulated in Chapter 4 for the quantitative analysis.

2.6 Novel Topology for Combined Battery-Ultracapacitor ESS

The main disadvantages of the best battery-ultracapacitor topology chosen from the literature for simulation in Section 2.5 (Figure 2-6 (b)) include the extra cost, mass, and losses associated with the high-power DC/DC converter used to interface the battery to the high-voltage bus. Another approach is to use a diode to decouple the battery and ultracapacitor voltages, rather than a high-power DC/DC converter. This approach can lead to lower cost, lower mass, and higher efficiency, though it introduces difficulties in how to best charge each ESS component. References [37] and [38] use the diode approach for a battery-ultracapacitor ESS in a pure-electric and a hybrid-electric vehicle, respectively. It can be shown that both proposed systems have room for improvement. First, these two systems are briefly analyzed, and then a new diode-based system for a fuel cell vehicle ESS is proposed, which offers improvements over the two diode-based systems for pure-electric and hybrid-electric vehicles from the literature, and over the best battery-ultracapacitor ESS for fuel cell vehicles found in the literature, as determined in Section 2.5.

The system proposed in [37] places a diode in series with an ultracapacitor pack, and connects this system in parallel with a battery pack, as shown in Figure 2-7. The philosophy behind this design is that when the battery voltage drops due to a high-current discharge, the diode becomes forward-biased and the ultracapacitor provides current as well, thus reducing the magnitude of the high-current pulse required from the battery. However, additional circuitry is required to make it possible to charge the ultracapacitor. A current-limiting switch in parallel with a resistor is placed anti-parallel to the diode to provide a path for charging the ultracapacitor from the battery. Also, a silicon-controlled rectifier (SCR) in series with a low-resistance resistor is connected anti-parallel to the diode to provide a path for charging the ultracapacitor from regenerative braking energy. When the ultracapacitor is charged up by regenerative braking to exceed the battery voltage, the charging current automatically transitions to the battery, and the SCR is commutated. In both ultracapacitor charge paths, resistors and/or current-limiting devices are used to prevent damaging in-rush currents caused by the difference between the voltages of the ultracapacitor and battery terminals. Therefore, a main disadvantage of this system is that the ultracapacitor charge paths are inefficient due to resistive losses. The other main disadvantage of this system is that the battery still provides and accepts power during each acceleration and deceleration, and the diode-ultracapacitor connection only reduces the magnitude of the current pulses. But since a main goal of combining a battery and ultracapacitor is to reduce battery current to extend battery lifetime, the system proposed in [37] is not an ideal ESS for hybrid vehicles.

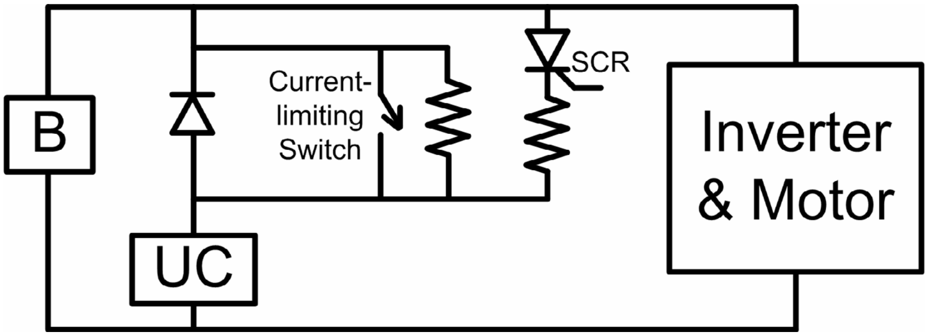

Figure 2-7: Battery-ultracapacitor-diode topology from the literature (1) [37]

Reference [38] uses a better approach by placing a diode in series with a battery pack, where the battery-diode combination is connected in parallel with an ultracapacitor pack, as shown in Figure 2-8. In this way, the ultracapacitor provides positive power until it is discharged to the battery voltage, and then the diode is forward-biased, allowing the battery to provide positive power as well. The control methodology dictates that only the ultracapacitor accepts regenerative braking energy, since the diode blocks the battery from accepting current.

However, difficulties arise when the battery charge methods are examined. The battery is charged from the internal combustion engine through the electric motor and inverter. A switch is connected anti-parallel to the diode to allow this charging of the battery. This switch is only closed when the battery and ultracapacitor voltages are within 10% of each other (to prevent large in-rush currents), and when the entire battery-ultracapacitor ESS is neither providing nor accepting power. The latter rule places severe restrictions on the amount of time available for the battery to be charged, since the ESS handles transient power requests very frequently, especially in a fuel cell vehicle where the ESS is generally used to smooth the fuel cell power request. If the ESS is not required for a short period of time while the vehicle is in motion (which is in itself a difficult thing to determine), the ultracapacitor voltage must first be discharged through the inverter to match the battery voltage before the anti-parallel switch can be closed.

Overall, the ability to charge the battery is very dependent on the operation of the rest of the powertrain during a drive cycle. This means that the battery may often have to instead be charged when the vehicle is not in motion. In this case, the ultracapacitor is discharged down to the battery voltage through a separate switch and resistor, which leads to unnecessary losses. Also, the internal combustion engine must be left on to charge the battery, which is inefficient and can be inconvenient and impractical. Another negative aspect of the battery-charging procedure is that the path is inherently inefficient since the battery has the highest charge efficiency at low currents (due to low internal I^2R losses) and the inverter, which is sized large enough to provide all of the peak ESS power requirements, is more efficient at higher load. Due to the difficulties and inefficiencies associated with battery charging, it is clear that there is room for improvement in the system presented in [38].

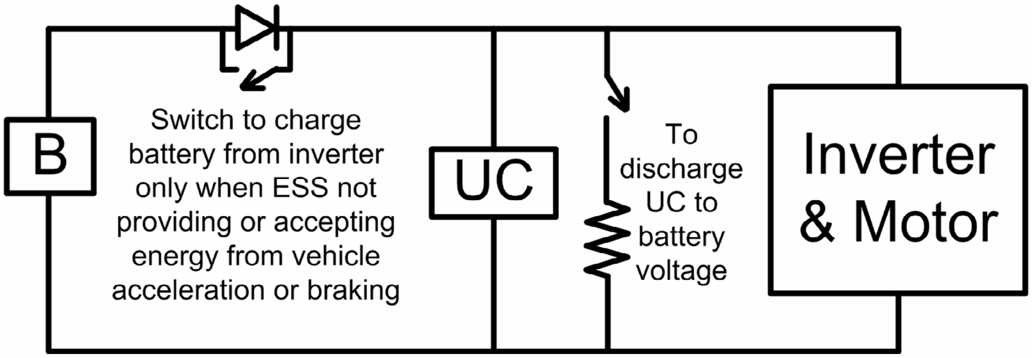

Figure 2-8: Battery-ultracapacitor-diode topology from literature (2) [38]

This thesis presents a novel topology for a fuel cell-battery-ultracapacitor powertrain, which is presented as two design options. The first option is shown in Figure 2-9. This topology aims to correct the disadvantages of the previously discussed battery-ultracapacitor topologies, while adding no significant disadvantages. Compared to the selected topology from Section 2.5, this topology only requires one high-power DC/DC unidirectional converter for boosting the fuel cell voltage. The ultracapacitor is connected directly to the high voltage bus and the battery is connected to the high voltage bus through a diode. Because this diode is not used in a high-speed switching scheme, it does not have to be a fast-recovery diode, and hence it can be chosen to have a very low forward voltage drop with minimal conduction losses.

The principle of operation of the system shown in Figure 2-9 is as follows: when power is required from the ESS, the ultracapacitor provides the initial power until the ultracapacitor voltage reaches the battery terminal voltage (minus the diode forward voltage drop), similar to the operation during positive power requests of the system in [38]. At this point, the battery and the ultracapacitor both provide the required power, and their respective impedances determine the power sharing. When regenerative braking occurs, the ultracapacitor is charged back up to a higher voltage than the battery. This operation ensures that the ultracapacitor provides most of the transient power requests, while the battery is only used when the power request is very large or the ultracapacitor is depleted.

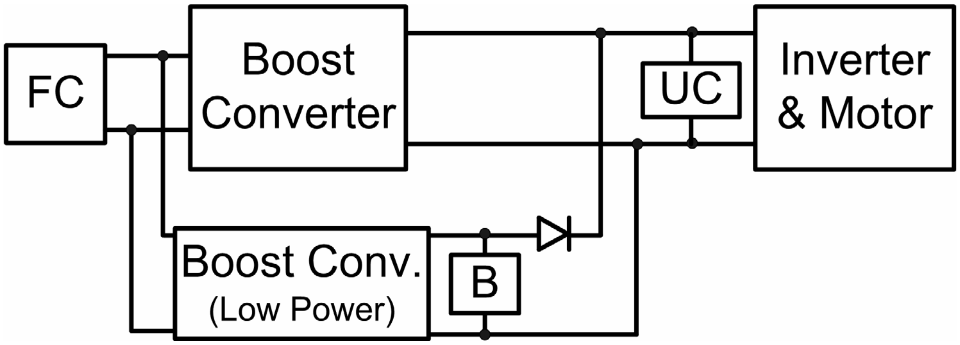

Figure 2-9: Proposed new battery-ultracapacitor ESS topology for a fuel cell vehicle (Option 1)

Unlike the restrictive rules required for battery charging in [38], the battery in the proposed topology can be charged from the fuel cell in a fully-controlled manner through a low-power (unidirectional) boost converter at any point during the drive cycle. To maintain high-efficiency charging, the following battery-charging rules are proposed:

(1) Only charge the battery when the fuel cell is providing enough power to the high-voltage bus to be operating above a certain efficiency (e.g., 45% or 50%); this ensures that the fuel cell is not operated at very low power in the low-efficiency region to charge the battery.

(2) Do not charge the battery when the battery is providing positive power to the high-voltage bus, as the high-power boost converter (which, at times when battery power is required, is likely processing enough fuel cell power to be operating in its higher-efficiency region) usually provides a higher-efficiency path for energy from the fuel cell that is desired immediately at the high-voltage bus.

Very high-efficiency charging of the battery can be achieved, since the low-power boost converter can operate in its high efficiency region, yet provide low-power charging for the battery (e.g., 1kW) to minimize the I^2R losses in the battery. This high-efficiency battery charging path is a major advantage over topology (b) from Section 2.5 and the system proposed in [38]. The proposed topology also has a higher-efficiency battery discharge path compared to topology (b) since the conduction losses from the diode are smaller than the overall losses of the high-power bidirectional DC/DC converter. Furthermore, the proposed topology retains the high-efficiency charge/discharge path of the ultracapacitors, as opposed to topology (c) from Section 2.5.

A straight-forward design procedure is proposed for choosing the power rating of the low-power boost converter, and can be based on initial simulation results that do not include charging the battery from the fuel cell. Simulation results for a typically expected drive cycle will include the change in battery energy, $E_{\Delta batt}$, and will give an indication of the percentage of time that conditions (1) and (2) are met for battery charging. For example, over a 490-second drive cycle, a conservative battery charging time is 50%, or 245 seconds. Initial results may show that $E_{\Delta batt} = 200$ kJ. Thus, the power required to replenish the 200 kJ over 245 seconds of battery charging is 200kJ/245s = 0.82kW. Thus, a 1-kW converter would be a good choice in this scenario. It is important to mention that since this low-power converter has relatively high voltages on both the input and the output sides (from the fuel cell and the battery), very low currents will be present. For example, if the minimum fuel cell voltage is 160V and the battery voltage is 330V, the input current would be approximately 6.25 A and the output current would be approximately 3 A. Thus, the converter can be generally designed to be very low in mass and cost, due to the low power and low current requirements.

A second option for the proposed topology is shown in Figure 2-10. This option involves adding an anti-parallel switch across the diode for the unique purpose of charging the battery from regenerative braking energy. The proposed control strategy is as follows:

(1) When the ultracapacitor voltage has decreased to the battery voltage during an acceleration and the inverter power request changes from positive to negative (i.e., regenerative braking begins), the anti-parallel switch is closed. This does not cause any in-rush current as the battery and ultracapacitor voltages are virtually equal.

(2) Both the battery and ultracapacitor accept regenerative braking energy until the battery current (which is continually increasing due to the rising voltage of the ultracapacitor) reaches the battery current upper limit. At this time, the anti-parallel switch is opened.

(3) The ultracapacitor alone accepts the rest of the regenerative braking energy, and its voltage rises above the battery voltage.

In this control scheme, the battery only accepts regenerative braking energy at the beginning of the regenerative braking event, and only in the case that the diode has been forward-biased during the previous acceleration event. The latter condition is justified by the fact that larger accelerations (which are more likely to deplete the ultracapacitor down to the battery voltage) generally give the vehicle more velocity and thus more kinetic energy, meaning it is most important at these times to be able to store some regenerative braking energy in the battery to reduce the chance that the ultracapacitor will become fully charged before regenerative braking is complete. During smaller accelerations (when the diode is not forward biased), the ultracapacitor provides all of the positive energy and should generally be able to store all of the regenerative braking energy during the following small deceleration.

The advantage of using Option 2 of the proposed topology is that there is the possibility of obtaining slightly higher fuel economy than with Option 1 for a given ultracapacitor size since there is less chance of the ultracapacitor becoming fully charged before regenerative braking is completed, in which case mechanical braking would be used resulting in the loss of some energy. However, this advantage effectively vanishes if the ultracapacitor pack is sized large enough to accept virtually all regenerative braking energy pulses. One disadvantage of using Option 2 of the proposed topology is the extra mass and cost of the anti-parallel switch, though these can be minimized by using a small switch rated only to handle the maximum battery charge current (which is much smaller than its maximum discharge current, as discussed in Section 4.2.4). Another possible disadvantage of using Option 2 is that if the ultracapacitor is adequately sized, storing some regenerative braking energy in the battery is less efficient than storing all of the regenerative braking energy in the ultracapacitor, due to the conduction losses through the anti-parallel switch and the higher I^2R and columbic losses of the battery. The most notable disadvantage of Option 2 is that the battery will be charged to its maximum current limit every time regenerative braking occurs after the battery has provided positive power. This means that the battery life extension gained from combining the battery and ultracapacitor is slightly reduced, since high-current charging reduces battery lifetime more quickly than the low-current charging that is controlled through the low-power DC/DC converter. However, the goal of this thesis is to prove that both options are superior to previous battery-ultracapacitor ESS topologies presented in the literature. It is left to the vehicle designer to choose the best option of the new topology for a specific vehicle design, based on the advantages and disadvantages discussed above.

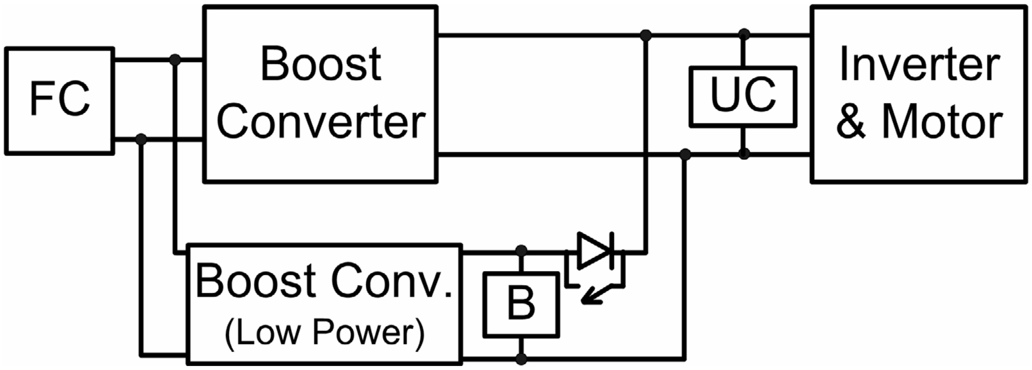

Figure 2-10: Proposed new battery-ultracapacitor ESS topology for a fuel cell vehicle (Option 2)

An interesting result from the use of a low-power boost converter to charge the battery from the fuel cell is the option of easily modifying the system to be a plug-in vehicle. A diode rectifier added before the input of the low-power boost converter can rectify the AC mains voltage, allowing the low-power boost converter to trickle-charge the battery over long periods (i.e., overnight). Only a diode would have to be added to the fuel cell path to ensure reverse current does not enter the fuel cell during charging. When the plug-in idea is considered for the most promising topology (b) from Section 2.5, it is found the a two-quadrant DC/DC converter which steps-down the bus voltage to the battery voltage would not suffice, since the 120V AC mains voltage would usually have to be stepped-up for a high-voltage battery. The use of a low-power boost converter for possible plug-in charging also offers a higher-efficiency charging path when compared to the use of the high-power DC/DC boost converters in other topologies analyzed (since the high-power converter is less efficient at light loads and the battery is more efficiently charged at low currents). Even though this thesis does not provide any further or quantitative analysis for plug-in vehicles, it is useful to note that the proposed battery-ultracapacitor ESS topology offers the flexibility for easy modification to a plug-in vehicle.

2.7 Summary

This chapter has analyzed numerous fuel cell vehicle powertrain topologies from the literature and has selected the best fuel cell-battery, fuel cell-ultracapacitor, and fuel cell-battery-ultracapacitor powertrain topologies from the literature for simulation in Chapter 4. This chapter has also proposed a novel diode-based fuel cell-battery-ultracapacitor topology which will be simulated and compared to the other topologies in Chapter 4. In summary, the proposed topology has the following advantages:

(1) It uses a low-power (e.g., 1kW) unidirectional DC/DC converter instead of the high-power (e.g., 20kW-70kW) bidirectional DC/DC converter used in topology (b) from Section 2.5. The resulting savings in mass and cost are significant.

(2) It provides a high-efficiency path for charging the battery, since the power is only processed by one low-power DC/DC boost converter and high efficiency low-power charging is possible.

(3) The battery charging rules are simple, and allow plenty of time during a drive cycle to charge the battery unlike the battery charging scheme in [38].

(4) It provides a high-efficiency path for discharging the battery, since the losses resulting from using a low-forward-voltage-drop diode are less than those of a high-power DC/DC converter.

(5) High-efficiency charging and discharging of the ultracapacitor is maintained.

(6) Though independent control of the battery power and the ultracapacitor power is not available when the diode is conducting, proper design of the system can still ensure that the ultracapacitor provides the majority of the transient power requirements, thus reducing battery use and extending the battery lifetime.

(7) The use of the low-power boost converter for battery charging allows for easy modification to a plug-in vehicle.

(8) Option 2 is provided to allow the battery to accept some regenerative braking energy, which can be an advantage over the system in [38].

(9) The proposed topology is more fault-tolerant than topology (b) from Section 2.5, since only a diode is required for the battery to provide positive power (rather than a high-power DC/DC converter), and a malfunction with the diode is less likely than with the converter.

Chapter 3 now presents a discussion on the hardware and controller design of DC/DC converters for use in fuel cell vehicles. The results are used for DC/DC converter modeling in Chapter 4. Chapter 4 provides a quantitative analysis based on vehicle simulation and cost data to perform an in-depth comparison of the proposed topology and the other promising fuel cell ESS topologies discussed in Chapter 2. Then, Chapter 5 presents an analytical design method for determining the optimal sizing of the battery and ultracapacitor in the proposed topology. The optimization method is based on the fact that the control of the ESS power split is embedded in the design of the component sizes. For example, a larger capacitance will mean a slower fall of the ultracapacitor voltage, which determines when the battery starts providing positive power. Also, a higher-voltage battery will start providing positive power sooner than a lower-voltage battery. The optimization method seeks to maximize efficiency, while minimizing mass and cost of the proposed topology for a given set of system constraints.

Chapter 3

DC/DC Converters In Fuel Cell Vehicles

DC/DC converters are crucial powertrain components in fuel cell vehicles because they allow the voltages of different power sources to vary independently of one another. For example, as discussed in Section 2.2, this means that the fuel cell can be sized based on the average power required rather than based on matching the fuel cell voltage to the usually higher voltage of the battery/ultracapacitor/motor inverter. DC/DC converters also provide the physical mechanism that actually controls the power from the source, allowing high-efficiency control methods to be employed. This chapter first presents the hardware design details of a 65-kW DC/DC converter that was custom-made for use in an actual fuel cell vehicle. The component types, masses, and costs are used from this real converter for accurate modeling of DC/DC converters in the vehicle simulator developed in Chapter 4. This chapter also presents the derivations of the transfer functions for a boost converter under voltage and current control, and shows that current control is superior to voltage control for use in a fuel cell vehicle due to the absence of right-half-plane (RHP) zeros. Since this result indicates that it is advantageous to use current control for boost converters, the vehicle simulator developed in Chapter 4 uses a current-request control method to control power flow in the vehicle.

As discussed in Chapter 2, the DC/DC step-up, or “boost”, converter is generally most useful in fuel cell vehicle powertrains, since it allows for the lower voltage of fuel cells or batteries to be stepped-up to match the usually higher motor inverter voltage. A non-isolated DC/DC step-up converter is suitable for use in fuel cell vehicles since isolation is generally not necessary and the required voltage boost is not too high (i.e., $V_{out}/V_{in} \leq 2$) [39]. This chapter focuses on the simple boost converter topology shown in Figure 2-3 (a), since all powertrain topologies analyzed in this thesis use this converter structure to process the fuel cell power. A bidirectional converter for use with a battery can be obtained from the converter shown in Figure 2-3 (a) by adding an anti-parallel switch across the boost diode. Soft-switching can be used to reduce the mass or increase the efficiency of these converters; a review of soft-switching methods and a novel regenerative snubber are presented in Chapter 6.

3.1 Design of a 65-kW Boost Converter for a Fuel Cell Vehicle

From 2004 to 2007, the University of Waterloo Alternative Fuels Team participated in a North American-wide student vehicle competition called ChallengeX. The task was to re-design and re-build a 2005 GM Equinox to improve fuel economy and reduce emissions while maintaining stock vehicle performance. Based on the components available at the time, the team decided on the fuel cell-battery topology shown in Figure 2-4 (a) powered by a 65-kW Hydrogenics fuel cell and a 70-kW, 336-V Nickel-Metal-Hydride battery from Cobasys. A custom-made 65-kW (350A) DC/DC boost converter was required to boost the voltage of the fuel cell and control the power from the fuel cell. This section summarizes the design and construction of the boost converter, which is pictured at one stage of development in Figure 3-1. The circuit diagram for the converter, which uses an insulated-gate bipolar-transistor (IGBT) switch, is shown in Figure 3-2. Table 3-1 lists the masses and costs of all components required for the converter.

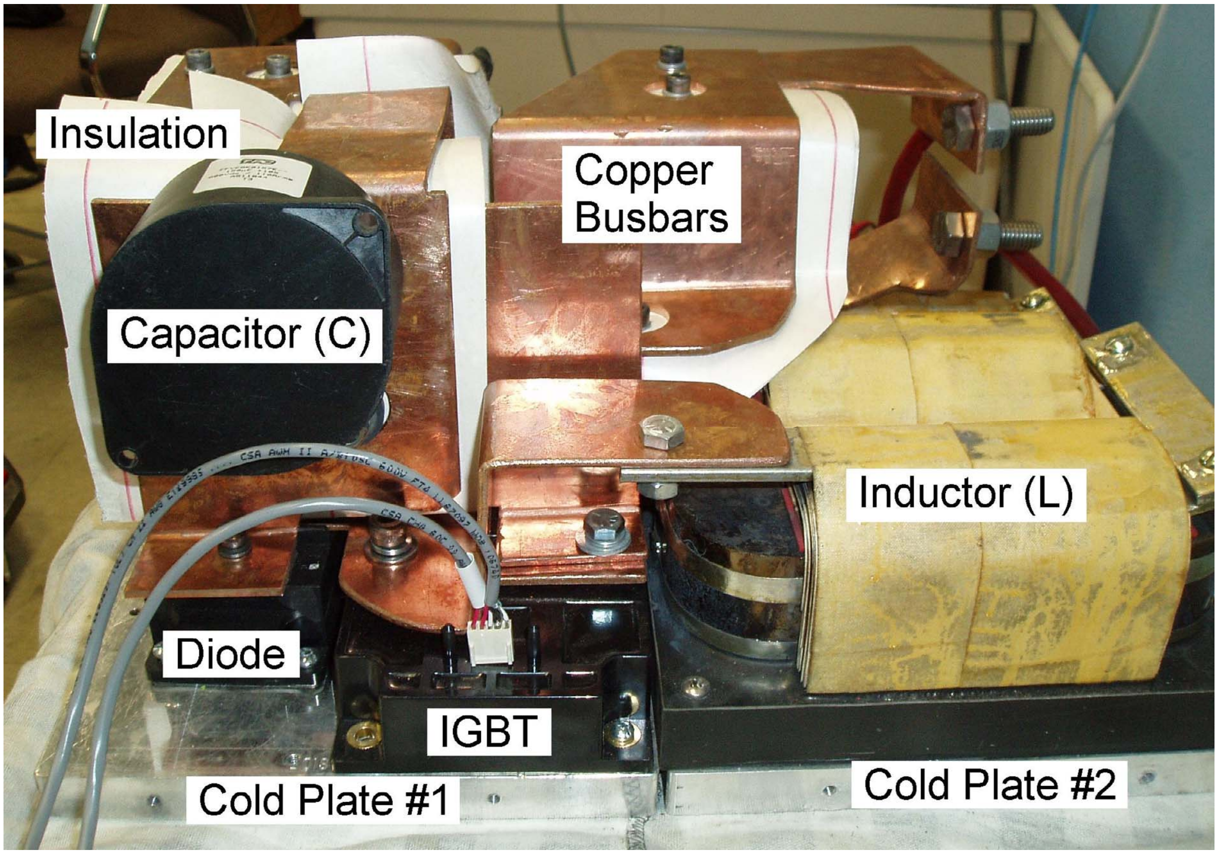

Figure 3-1: Custom-made 65-kW boost converter for a fuel cell vehicle

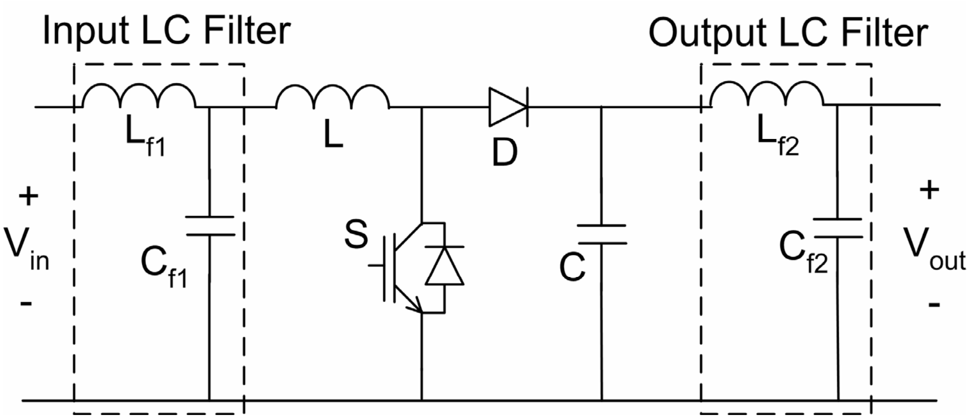

Figure 3-2: Circuit diagram of 65-kW boost converter

Table 3-1: Masses and Costs of Components for 65-kW Boost Converter

Component Description	Mass (kg)	Cost (USD)	Quantity	Total Mass (kg)	Total Cost (USD)
Basic Circuit Components:					
S - IGBT module (PM600HSA120)	1.09	450	1	1.09	450
D - Diode (RM400HA-24S)	0.46	360	1	0.46	360
L - 100uH boost inductor	10.8	714.29	1	10.8	714.29
C - 150uH capacitors	0.42	82	2	0.84	164
Lf1 - 20uH input filter inductor	2.1	138.89	1	2.1	138.89
Lf2 - 20uH output filter inductor	1.1	72.75	1	1.1	72.75
Cf1, Cf2 - 2.2mF capacitors	1.12	104	2	2.24	208
Total				18.63	2107.93
Auxiliary Components Required:					
Cold Plate for liquid cooling system	1.4	554.2	2	2.8	1108.4
Copper busbars	5.6	185	1	5.6	185
Insulator for busbars	0.1	15	1	0.1	15
Nuts, bolts, connectors	0.8	25	1	0.8	25
Aluminum enclosure	2.2	40	1	2.2	40
Fans	0.6	35	2	1.2	70
Liquid cooling system (piping, radiator)	5.4	170	1	5.4	170
Pre-charge circuit (resistor, contactors)	0.2	20	1	0.2	20
Total				18.3	1633.4
Total (Basic + Auxiliary Components)				36.93	3741.33
(Basic + Auxiliary Components)/ (Basic Components)				1.98	1.77

Various lessons were learned through the design, construction, and testing of the 65-kW converter that can be applied to the converter models in Chapter 4. These include:

(1) High-power inductors are large and heavy and contribute significantly to the mass and cost of the converter. Note that the costs used in Table 3-1 are the estimated mass production costs ($66.138/kg) because the costs of the actual custom-made inductors used in the 65-kW converter were much higher and do not give a good estimate of costs in a high-volume situation.

(2) In order to keep the turn-off voltage spikes across the switch below maximum safe levels, parasitic inductance in the circuit must be minimized. This can be done by using copper busbars to connect the components, with thin sheets of insulation material placed between the positive and negative copper plates. As shown in Table 3-1, these copper busbars add significant cost and mass to the system.

(3) In addition to the cost and mass of the basic components (IGBT, diode, inductors, and capacitors) significant cost and mass is added by other necessary components for connections, the enclosure, the cooling system, etc., as shown in Table 3-1. The last row of Table 3-1 shows the factor by which the basic components' mass and cost must be multiplied to arrive at the total mass and cost of the system, including the auxiliary components. It can be seen that the mass of the basic components is multiplied by 1.98 to get the total mass of the system, and the cost of the basic components is multiplied by 1.77 to get the total cost of the system.

The idea of the mass and cost multiplication factors discussed in point (3) is used in Chapter 4 to obtain an accurate mass and cost for the DC/DC converter(s) in each simulation run. In Chapter 4, the mass factor is estimated to be 1.85, since it is anticipated that experts in industry could reduce the mass of the auxiliary components, compared to the mass factor of 1.98 for the custom-made 65-kW converter. It is also expected that the cost factor could be reduced by industry. However, the construction and testing of a high-power converter requires many work-hours, which have not been included in the total cost calculations. Therefore, the cost factor in Chapter 4 is only slightly reduced from the cost factor for the 65-kW converter, to 1.7, to account for the cost of building and testing each converter. It should be noted that mass and cost multiplication factors are parameters that can be modified if more recent or accurate data is available.

3.2 Control Method Selection for Boost Converter in a Fuel Cell Vehicle

There are generally two controllable parameters in a DC/DC boost converter: output voltage and input current. Two simplified control diagrams for voltage and current control, using a proportional-integral (PI) controller, are shown in Figure 3-3 (a) and (b), respectively. The choice of which control parameter to use should be based on (i) the suitability for the application, and (ii) obtaining optimal closed-loop behaviour of the system. For a fuel cell vehicle powertrain, the input-current control method is suitable because it allows intuitive management of the power flows within the powertrain. However, the closed-loop behaviour of a boost converter under voltage control and current control must also be investigated so that the optimal control method can be identified. To do this, the state-space model of a boost converter (in continuous mode of operation and linearized around a specific operating point) is presented, as derived in Appendix A and [40]. The transfer functions of the converter under output-voltage control and input-current control are derived. Then, the locations of the poles and zeros for each control type are analyzed so that conclusions can be made regarding the stability and trackability of each system. For the DC/DC boost converter modeling, a constant voltage source (V_{in}) and resistive load are included, as shown in Figure 3-4.

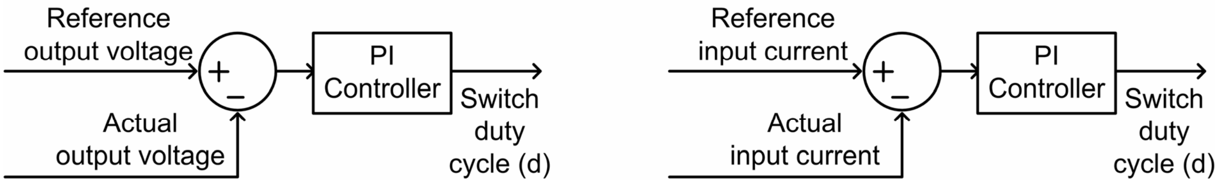

(a) Output voltage control (b) Input current control

Figure 3-3: Simplified control diagrams for a DC/DC boost converter

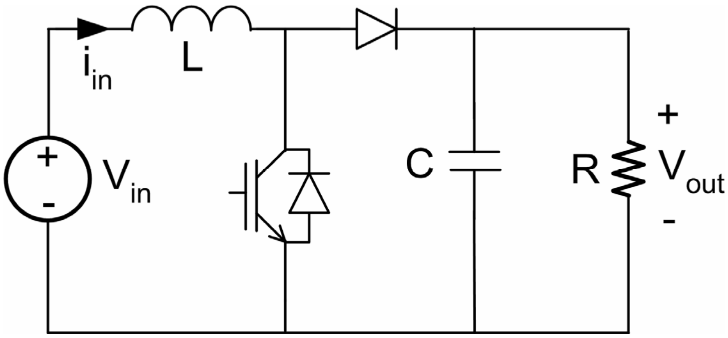

Figure 3-4: DC/DC boost converter diagram for modeling purposes

The generalized linear state-space model is given by Equation (3-1) where $\overline{x}$ is the system state vector, $\overline{u}$ is the input vector, and $\overline{y}$ is the output vector. Equation (3-2) shows the state-space model of a DC/DC boost converter in continuous mode operation and linearized around V^*_{in} and V^*_{out}, as derived in Appendix A (based on [40]). The variables Δi_{in} and Δv_{out} represent the small perturbations of i_{in} (the input current) and v_{out} (the output voltage) from steady state when small changes in V_{in} and/or the switch duty cycle, d, occur.

$$\begin{aligned} \frac{d\overline{x}}{dt} &= A\overline{x} + B\overline{u} \\ \overline{y} &= C\overline{x} + D\overline{u} \end{aligned} \tag{3-1}$$

$$\begin{aligned} \frac{d}{dt}\begin{bmatrix} \Delta i_{in} \\ \Delta v_{out} \end{bmatrix} &= \begin{bmatrix} 0 & -\frac{V^*_{in}}{LV^*_{out}} \\ \frac{V^*_{in}}{CV^*_{out}} & -\frac{1}{RC} \end{bmatrix}\begin{bmatrix} \Delta i_{in} \\ \Delta v_{out} \end{bmatrix} + \begin{bmatrix} \frac{1}{L} & \frac{1}{L}V^*_{out} \\ 0 & -\frac{V^{*\,2}_{out}}{RCV^*_{in}} \end{bmatrix}\begin{bmatrix} \Delta V_{in} \\ \Delta d \end{bmatrix} \\ \overline{y} &= \begin{bmatrix} 0 & 1 \\ 1 & 0 \end{bmatrix}\begin{bmatrix} \Delta i_{in} \\ \Delta v_{out} \end{bmatrix} + \begin{bmatrix} 0 & 0 \\ 0 & 0 \end{bmatrix}\begin{bmatrix} \Delta V_{in} \\ \Delta d \end{bmatrix} \end{aligned} \tag{3-2}$$

From linear control theory, the general transfer function *H(s)* can be found from the state-space model using Equation (3-3).

$$H(s) = C(sI - A)^{-1}B + D \tag{3-3}$$

The transfer function is now derived for the output-voltage control method. In the case of output-voltage control of the boost converter, the output of interest is Δv_{out} and the desired input-to-output transfer function is $\Delta v_{out}/\Delta d$. Therefore, matrices *B* and *C* from Equation (3-2) can be re-written as shown in Equation (3-4).

$$B' = \begin{bmatrix} \frac{1}{L}V^*_{out} \\ -\frac{V^{*\,2}_{out}}{RCV^*_{in}} \end{bmatrix} \qquad C' = \begin{bmatrix} 0 & 1 \end{bmatrix} \tag{3-4}$$

Equation (3-3) is applied to Equation (3-2), using *B'* and *C'* from Equation (3-4) instead of *B* and *C* from Equation (3-2) in order to obtain the desired transfer function, as shown in Equation (3-5).

$$H_v(s) = \frac{\Delta v_{out}}{\Delta d} = \frac{\frac{V_{in}^*}{LC} - \left[\frac{V_{out}^{*2}}{RCV_{in}^*}\right]s}{s^2 + s\left[\frac{1}{RC}\right] + \frac{1}{LC}\left(\frac{V_{in}^*}{V_{out}^*}\right)^2} \tag{3-5}$$

The locations of the two poles are found by setting the denominator of $H_v(s)$ to zero and solving for *s* as follows:

$$s_{P1}, s_{P2} = \frac{-\frac{1}{RC} \pm \sqrt{\left(\frac{1}{RC}\right)^2 - \frac{4}{LC}\left(\frac{V_{in}^*}{V_{out}^*}\right)^2}}{2} \tag{3-6}$$

When the discriminant in Equation (3-6) is greater than or equal to zero, the two poles are in the left-half-plane (LHP), meaning the system is bounded-input-bounded-output (BIBO) stable. Thus, *R*, *C*, and *L* should be chosen appropriately for the desired V^*_{in} and V^*_{out} so that the discriminant is greater than or equal to zero.

The zeros of the system are found by setting the numerator of Equation (3-5) to zero, and solving for *s*, as shown in Equation (3-7).

$$s_Z = \frac{R}{L}\left(\frac{V_{in}^*}{V_{out}^*}\right)^2 > 0 \quad \Rightarrow \mathit{zero\ in\ RHP} \tag{3-7}$$

Equation (3-7) shows that the output-voltage-controlled boost converter has a zero in the right-half-plane (RHP). This is undesirable as it acts as a delay and therefore, the system may have stability problems and cannot achieve arbitrarily good tracking. The physical explanation of the RHP zero is that when the switch duty cycle is increased in order to increase the output voltage, the output capacitor voltage first decreases before rising, meaning arbitrarily good tracking is not possible. In extreme cases, such as a step change in the reference voltage, the voltage of the capacitor may not recover and the output voltage can become unstable.

The transfer function is now derived for the current-control method. In the case of input-current control of the boost converter, the output of interest is Δi_{in} and the desired input-to-output transfer function is $\Delta i_{in}/\Delta d$. Therefore, matrices *B* and *C* from Equation (3-2) can be re-written as shown in Equation (3-8).

$$B' = \begin{bmatrix} \frac{1}{L} V_{out}^{*} \\ -\frac{V_{out}^{*\ 2}}{RCV_{in}^{*}} \end{bmatrix} \qquad C' = \begin{bmatrix} 1 & 0 \end{bmatrix} \tag{3-8}$$

Equation (3-3) is applied to Equation (3-2), using *B'* and *C'* from Equation (3-8) instead of *B* and *C* from Equation (3-2) in order to obtain the desired transfer function, as shown in Equation (3-9).

$$H_i(s) = \frac{\Delta i_{in}}{\Delta d} = \frac{s\left[\frac{V_{out}^{*}}{L}\right] + \frac{2V_{out}^{*}}{RLC}}{s^2 + s\left[\frac{1}{RC}\right] + \frac{1}{LC}\left(\frac{V_{in}^{*}}{V_{out}^{*}}\right)^2} \tag{3-9}$$

The denominator of $H_i(s)$ is equal to the denominator of $H_v(s)$ (since the *A* matrix is the same for both cases), and thus, the two poles of the current-controlled converter are also in the LHP; hence this system is also BIBO stable.

The location of the zero is found by setting the numerator of Equation (3-9) to zero; this yields the following result:

$$s_Z = -\frac{2}{RC} < 0 \quad \Rightarrow \textit{zero in LHP} \tag{3-10}$$

Thus, the input-current-controlled boost converter has a zero in the LHP, which is more desirable because arbitrarily good tracking is achievable. The physical explanation is that when the duty cycle of the switch is increased to increase input current, the current in the inductor increases as desired, due to the switch being closed for a longer period of time.

In conclusion, the input-current-control method for the boost converter is advantageous to the output-voltage-control method because (i) it is more suitable for intuitively controlling the power flow in the vehicle powertrain and (ii) it has both the poles and the zero in the LHP meaning the closed-loop system is stable and arbitrarily good tracking is achievable. Therefore, the vehicle simulator created in Chapter 4 to compare the powertrain topologies from Chapter 2 is structured such that the control strategy sends current requests to the DC/DC converter(s) to control the fuel cell (and in one case, the battery) output current, and thus, manage the power flows within the powertrain. Overall, Chapter 3 has provided insight into the design and control of DC/DC boost converters which is applied to the vehicle simulator models in Chapter 4.

Chapter 4

A Study on the Optimization of the Fuel Cell Vehicle Powertrain

One important contribution of this thesis is to provide a comprehensive comparison of the most promising fuel cell vehicle topologies. Chapter 2 provided a qualitative analysis to determine the most suitable topologies for three ESS types (battery-only, ultracapacitor-only, and battery-ultracapacitor) to be modeled and simulated in Chapter 4. Chapter 3 provided insight into the mass, cost, and control aspects of DC/DC boost converters which are used for modeling in Chapter 4. The goal of Chapter 4 is to use simulation results to identify the powertrain topology and component types and sizes that, in combination with a near-optimal control strategy, create a vehicle which maximizes fuel economy, durability, and performance, while minimizing cost. In order to provide the quantitative analysis, a vehicle simulator must be chosen or created. The following discussion reviews two commonly-used vehicle simulators and provides motivation for the creation of a new simulator in this thesis.

Software such as the Advanced Vehicle Simulator (ADVISOR) [41] and the Powertrain Systems Analysis Toolkit (PSAT) [42] are popular for simulating advanced vehicles such as hybrid-electric, battery-electric, and fuel cell vehicles. Both programs are based on MATLAB/Simulink and have been used by engineers in industry and academia. The first version of ADVISOR was developed in 1994 by the US National Renewable Energy Laboratory in order to assist the Department of Energy develop technologies for hybrid-electric vehicles. ADVISOR uses a backward-looking model, which means the vehicle follows the given drive cycle precisely, and the power required from each component is calculated backwards. PSAT was released in 2002 by Argonne National Laboratory. It uses a forward-looking vehicle model, which can be seen as an improvement over the approach used in ADVISOR. In PSAT, the “driver” gives appropriate control signals (accelerate, decelerate) based on a given drive cycle and the control strategy selected (conservative or performance). This allows the implementation of different control strategies, which can be compared in terms of overall efficiency and how close the vehicle tracks the drive cycle.

The main disadvantage that is common to both ADVISOR and PSAT is that they are based on pre-defined vehicle topologies and pre-defined control strategies. This means that it is not possible to model the novel battery-ultracapacitor topology presented in Section 2.6, which is one of the main goals of the quantitative analysis. Furthermore, ADVISOR and PSAT use very basic models, such as an efficiency look-up table based on input power, for the DC/DC converters which are so crucial to fuel cell vehicle powertrains. However, it is desirable to include more detailed models of efficiency, mass, and cost for the DC/DC converters in this analysis, since the power electronic components contribute significantly to the losses, mass, and cost of the powertrain. Though it is possible to alter the component models in PSAT and ADVISOR, it can be difficult and time-consuming to make these modifications and to ensure their correct operation within the software.

Therefore, for the preceding reasons, a forward-looking vehicle simulator is created in this thesis using MATLAB/Simulink for the purpose of comparing the most promising fuel cell vehicle architectures. To ensure the results are applicable in the real world, models are developed based on real components wherever possible and detailed power electronic converter models are used. For a good trade-off between accuracy and run-time, modeling details are included when they significantly affect the optimization goals (e.g., in precise modeling of the DC/DC converters) and are omitted otherwise (e.g., in simplified modeling of the inverter and motor).

4.1 Literature Review and Goals for the Optimization Study

Though many researchers have investigated the use of different powertrain topologies, component sizes, and control strategies in fuel cell vehicles, a detailed parametric study of the vehicle types must be conducted before a fair comparison of fuel cell vehicle types can be performed. A lot of work has been done to investigate optimal sizing and control strategies for fuel cell-battery [24][43][44][45], fuel cell-ultracapacitor [24][29][43][46], and fuel cell-battery-ultracapacitor [24][30][31][32] vehicles. Most studies implement a coarse parametric search on the component sizes and some also vary the control parameters. To ensure optimality (or near-optimality), the control and plant parameters should be varied simultaneously due to plant-controller coupling [47]. Other common deficiencies include not using a detailed model of the DC/DC converter(s) and not including cost in the analysis, though cost is a major obstacle for fuel cell vehicles. Furthermore, most studies analyze a single type of fuel cell vehicle and so cannot fairly compare the three ESS types.

Reference [24] comes closest to a fair comparison because it considers fuel economy, acceleration time, and ESS cost for the three vehicle types. However, it only compares two sizes of a battery ESS, two sizes of an ultracapacitor ESS, and one size of a battery-ultracapacitor ESS (which is shown to be superior to the other designs). Also, the fuel cell size is kept constant at 50kW, the controller is not altered for the different plant designs, and the changing mass and cost of the DC/DC converters are not considered. Most notably, this study uses lead-acid batteries in the analysis, even though new lithium-ion batteries have higher power density and energy density [26] and are quickly becoming the battery-of-choice for hybrid-vehicle applications.

The previous research adds significant knowledge to the field, but does not provide a comprehensive comparison of the three fuel cell vehicle types. This thesis aims to fill this gap by performing combined plant/controller optimizations on a fuel cell-battery, a fuel cell-ultracapacitor, and three fuel cell-battery-ultracapacitor vehicles (using the topologies selected in Chapter 2), and then comparing the best vehicles in each category to provide a fair conclusion on the merits of each ESS type. The parametric study includes a wide range of plant variables, so that all feasible component sizes are considered. The objective function used in the optimization is a weighted combination of the normalized acceleration time, fuel economy, and powertrain cost. In addition to the objective function, durability is considered by examining the battery current profile for each of the top vehicles to estimate battery life extension for the battery-ultracapacitor topologies.

4.2 Models

4.2.1 Vehicle Model

Figure 4-1 shows the five topologies which are modeled and simulated for the parametric analysis.

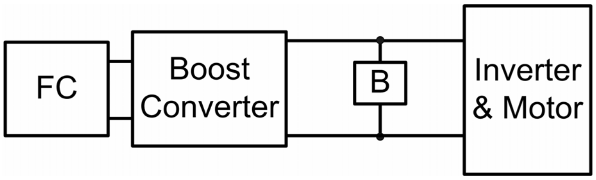

(a) FC-B Topology

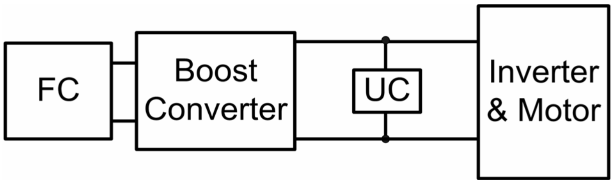

(b) FC-UC Topology

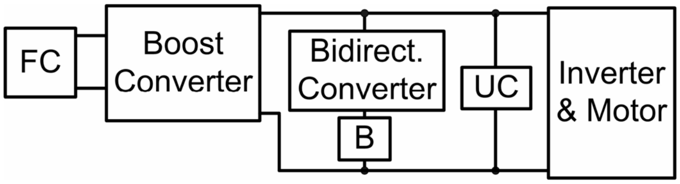

(c) FC-B-UC Topology 1 (from literature)

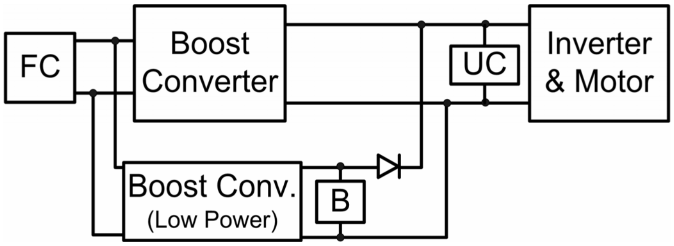

(d) FC-B-UC Topology 2 (novel topology Option 1)

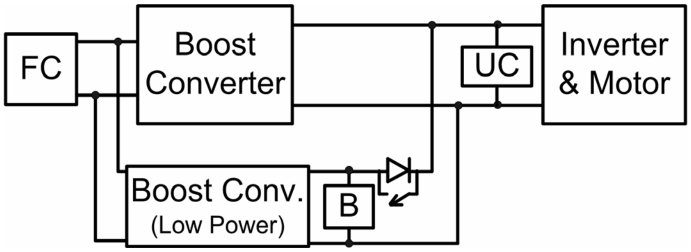

(e) FC-B-UC Topology 2 (novel topology Option 2)

Figure 4-1: The five vehicle powertrain topologies modeled and simulated in Chapter 4

In addition to the powertrain components shown in Figure 4-1, the vehicle model consists of a driver model and vehicle body block, a global control strategy block, and a motor inverter, motor, and vehicle body block, as shown in Figure 4-2 for the FC-B-UC vehicle (Topology 1). In general, the current from the ESS which is not controlled by a DC/DC converter (the ultracapacitor current for the vehicle model shown in Figure 4-2) can be indirectly controlled since it is the difference between the motor inverter current request and the sum of the output currents from the DC/DC converters for the fuel cell and battery. The driver model is a PI controller which uses the error signal (desired velocity minus actual velocity) to provide a control signal, ΔF_{PI}, which precisely tunes the approximated linear force command from the vehicle body model. The vehicle body model is based on the 2005 GM Equinox, a small SUV, and uses Equations (4-1) to (4-5) to approximate the linear force required to attain the desired speed.

Table 4-1 defines the terms in Equations (4-1) to (4-5) and gives the vehicle parameters.

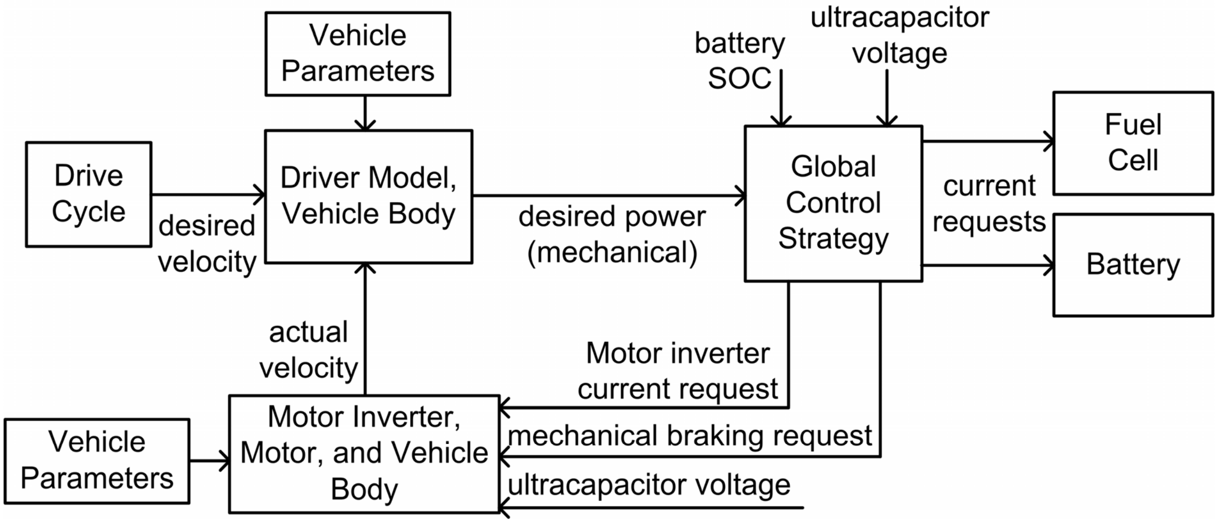

Figure 4-2: Overall vehicle model for a FC-B-UC vehicle

$$F_{aero} = \frac{1}{2}\rho_{air} A_{frontal} C_{drag} V^2 \tag{4-1}$$

$$F_{roll} = C_{roll} m_{veh} g \tag{4-2}$$

$$F_{accel} = m_{veh} \frac{dV}{dt} \tag{4-3}$$

$$F_{incline} = m_{veh} g \sin(\theta \frac{\pi}{180}) \qquad \textbf{(4-4)}$$

$$P_{mech} = (F_{aero} + F_{roll} + F_{accel} + F_{incline} + \Delta F_{PI})V \qquad \textbf{(4-5)}$$

Table 4-1: Vehicle Parameters

Term	Description	Value (if applicable)
F_{aero}	Force due to aerodynamic losses (N)	
ρ_{air}	Atmospheric density (kg/m^3)	1.2 kg/m^3
$A_{frontal}$	Vehicle frontal area (m^2)	2.686 m^2 (2005 GM Equinox)
C_{drag}	Vehicle coefficient of drag	0.47 (2005 GM Equinox)
V	Desired vehicle velocity (m/s)	(depends on drive cycle under test)
F_{roll}	Force due to rolling resistance losses (N)	
C_{roll}	Rolling resistance coefficient	0.004 (Michelin 235-710 R460A low rolling resistance tires)
m_{veh}	Gross vehicle mass (kg)	(depends on vehicle configuration)
g	Acceleration due to gravity (m/s^2)	9.81 m/s^2
F_{accel}	Force required for desired acceleration (N)	
$F_{incline}$	Force due to road incline (N)	
θ	Road inclination angle (degrees from horizontal)	(depends on drive cycle under test)

The global control strategy block converts the desired mechanical power signal into current requests for the power sources and the motor inverter. The details of the control strategies for each vehicle type are presented in future sections. Finally, the motor inverter, motor, and vehicle body block uses the bus voltage and current to calculate the instantaneous vehicle velocity. The motor inverter is modeled simply with a constant efficiency of 96% [25] and the motor speed-torque map is obtained from PSAT [43] for an induction motor. Also based on PSAT, the base vehicle mass is set to 1800kg, which includes the driver and all vehicle components except the fuel cell, DC/DC converter(s), and batteries and/or ultracapacitors. Since vehicle range is not part of the objective function, and range is determined mainly by the size of the hydrogen tank, the tank size is assumed constant and is included in the base vehicle mass of 1800kg.

4.2.2 Fuel Cell Model

To circumvent the many complicated details of fuel cell modeling, such as cell area, material type, and size of blowers, the model focuses on the net electrical output characteristic (current-voltage or I-V curve) and the efficiency curve. Typical efficiency and I-V curves for net power output are shown in Figure 4-3 and are based on Hydrogenics HyPM fuel cells [10]. The scaling in terms of percentage of maximum current and percentage of maximum voltage assumes the shapes of the efficiency and I-V curves to remain the same for different fuel cell power sizes. Thus, the same curves relating %V to %I and efficiency to %I can be used for different fuel cell sizes for each simulation run.

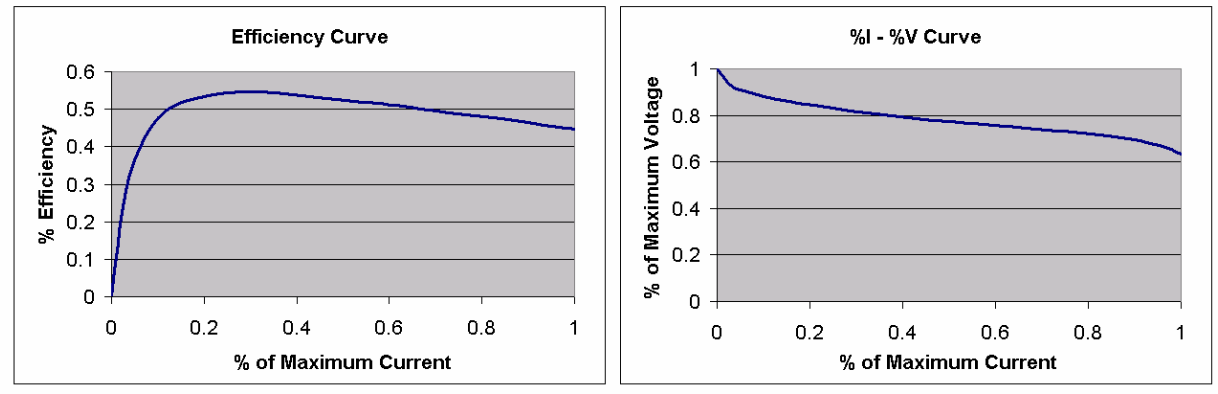

Figure 4-3: Fuel cell efficiency and %I-%V curves

Based on the actual current request to the fuel cell, the fuel cell voltage and efficiency can be found from %I-%V and %I-efficiency look-up tables. The energy equivalent of the hydrogen used can then be found in terms of the gasoline gallons equivalent (*gge*) and the fuel economy can be found in miles per gasoline gallon equivalent (*mpgge*) as follows:

$$E_{H2}(t_{final}) = \int_0^{t_{final}} \left(\frac{P_{fc}(t)}{\varepsilon_{fc}(t)} + \frac{P_{aux}}{\varepsilon_{avg}} \right) dt \quad joules \tag{4-6}$$

$$gge = \frac{1}{3600} \frac{Wh}{joule} \times K \frac{gge}{Wh} \times E_{H2}(t_{final}) \tag{4-7}$$

$$mpgge = \frac{miles}{gge + \left(\frac{E_{\Delta SOC}}{\varepsilon_{path}} \times K \right)} \tag{4-8}$$

Equation (4-6) calculates the energy content in joules of the hydrogen used to power the vehicle, where the instantaneous fuel cell efficiency, $\varepsilon_{fc}(t)$, is used to calculate the energy used by the fuel cell for purposes of propelling the vehicle, and the estimated average fuel cell efficiency, ε_{avg} (50%), is used to calculate the energy used by the fuel cell to power the vehicle auxiliary systems, an estimated constant, P_{aux} (2947W). The auxiliary power required is estimated at 2.5kW and is divided by the product of efficiencies of the components in the path from the fuel cell to the auxiliary system, i.e., DC/DC converter to low voltage system (94%), columbic efficiency of low-voltage battery (95%), and I^2R losses of low voltage battery (95%), to obtain P_{aux}. Equation (4-7) uses a constant, $K = 2.982 \times 10^{-5}$ [48] to convert electrical energy in watt-hours (Wh) to the energy equivalent in gallons of gasoline. In the calculation of the final *mpgge*, Equation (4-8) includes the change in energy (in Wh) of the battery and ultracapacitor states-of-charge (SOC), $E_{\Delta SOC}$, over the duration of the drive cycle, as well as the efficiency of the path to charge each ESS from the fuel cell, ε_{path}.

An automotive-grade fuel cell is capable of going from idle to full power in less than 4 seconds [10]. This time delay inherent in the fuel cell is simply modeled by appropriately limiting the rate of increase of the power request for the fuel cell.

Based on a review of various commercial fuel cells [10][11], it was determined that a linear scaling for mass would be suitable for the range of fuel cell power under study. Fuel cell cost is a difficult parameter to define due to the large discrepancies between present and predicted future costs [49][50]. However, since high cost is a major obstacle for fuel cell vehicles, it is imperative to include cost in the analysis so that the conclusions are useful for industry. Current fuel cell costs are estimated to be from \$3000/kW [49] to \$4500/kW [50] (all costs are in USD). However, [49] estimates that mass-production costs could be as low as \$225/kW, and [50] predicts costs could drop to \$400/kW by 2010. This thesis assumes a cost of \$400/kW, but also performs the optimization for costs ranging from \$225/kW to \$4500/kW. It is interesting to note that even at \$225/kW, fuel cells are by far the most costly source of power in the vehicle.

The lower bound on the fuel cell power variable is set to the minimum power required for the vehicle to cruise at 120km/h using Equations (4-1) to (4-5) with an estimated total vehicle mass of 2000kg. The mechanical power required is found to be 30.7kW, which is divided by the efficiencies of the components in the path from the fuel cell (DC/DC boost converter 96%, inverter 96%, motor 90%) to get the fuel cell electrical power required (37kW). The auxiliary power (P_{aux} = 2947W) is then added to obtain the total minimum fuel cell power required, which is about 40kW.

4.2.3 Ultracapacitor Model

The ultracapacitor model is based on Maxwell Technologies' BCAP0350 cell [19] and the cell parameters are shown in Table 4-2 [19]. These ultracapacitors have high durability, losing less than 20% of their capacitance after 500,000 cycles, at 10A and 25°C [19]. Since the acceptable motor voltage range is set to be 250V to 425V [25], and the ultracapacitor pack will be connected directly to the high voltage bus in all of the topologies to be simulated, the maximum ultracapacitor pack voltage should be 425V. Thus, 170 2.5-V cells are used in series to attain the maximum voltage of 425V. Therefore, the optimization variable is chosen to be the number of strings in parallel (uc_p). The terminal ultracapacitor voltage, $v_{uc}(t)$, is calculated using Equation (4-9) where C is the total capacitance based on uc_p and R_{uc} is the total internal resistance based on uc_p.

$$v_{uc}(t) = v_{uc}(0) + \frac{1}{C}\int_0^t i_{uc}(\lambda)d\lambda + i_{uc}(t)R_{uc} \tag{4-9}$$

Table 4-2: Maxwell Technologies' BCAP0350 Cell Parameters

Maximum Voltage	2.5 V
Rated Current (including safety margin)	85 A
Internal Resistance @ DC	0.0032 Ω
Mass	60 g
High Volume Cost (per cell)	$7

Based on correspondence with a Maxwell Technologies' representative, the upper current limit (for the duty cycles in these simulations) is set to 85A per cell, which includes a margin of safety necessary in automotive systems. Also, the high volume pricing is set to $7 per cell. However, this cost and the 60-g cell mass do not include any cell balancing or packaging. Thus, the BMOD0058 15-V pack, which contains six 2.5-V BCAP0350 cells in series, is considered to obtain cost and mass estimates for cell balancing and packaging. The 15-V pack mass is 680g which means there is approximately 53g extra per cell for cell balancing and packaging. Also, the high-volume cost estimate for the pack is $85, which means the extra cost for cell balancing and packaging is about $7 per cell. Thus, the final mass and cost used in the simulation is 113g and $14 per ultracapacitor cell. The extra 53g and $7 per cell will also be used in the battery model, since the cells are of similar size, and a battery module also requires cell balancing and a structured package.

4.2.4 Battery Model

The battery model used in this study is based on A123 Systems' high-power lithium-ion ANR26650MI cell [18], which shows high power density, high efficiency, and low cost compared to batteries used in previous vehicle studies [24][45][51]. The two variables, the number of cells in series ($batt_s$) and in parallel ($batt_p$), determine the total resistance and %voltage-SOC curves. Similar to the fuel cell model, the %voltage-SOC curve is a function of percentage of maximum voltage, so that the same curve can be used for different numbers of cells in series.

Figure 4-4 shows a basic diagram of the battery model. The battery current is measured and multiplied by the battery voltage. This power is integrated and then converted from joules to kWh, so that the energy into or out of the battery can be added to the initial energy in the battery (in kWh). The instantaneous amount of energy in the battery is then divided by the total battery capacity to get the battery SOC in percentage. The lookup table converts this %SOC to voltage, based on the discharge curve for the ANR26650MI cell. The columbic efficiency is also included and is estimated at 95% [52].

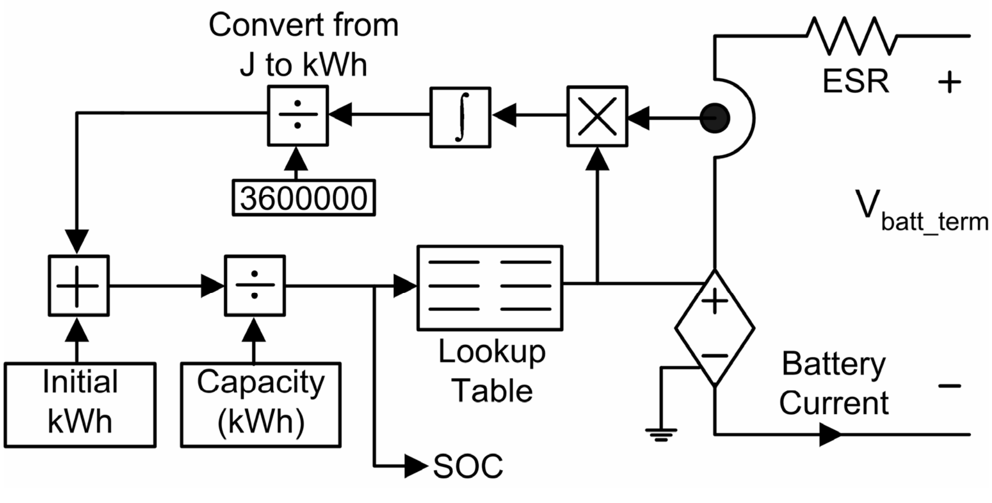

Figure 4-4: Simplified diagram of battery model

The battery cell parameters are shown in Table 4-3. Each cell has a mass of 70g and after adding 53g for cell balancing and packaging, the total mass is 123g per cell. The published low-volume cost is equivalent to \$18.33 per cell [18]. For higher-volume production, it is assumed the cost could be reduced to 70% of the low-volume cost, which is \$12.83. Finally, based on the cost of cell balancing and packaging for the ultracapacitor, \$7 is added to each cell to make the final estimated cost for high-volume production \$19.83 per cell. It should be noted that the battery pack may require more electronics for monitoring and control than the ultracapacitor pack (since the battery SOC cannot be easily determined by the terminal voltage) and a larger cooling system than that of the ultracapacitor pack (due to higher internal losses). However, it is beyond the scope of this thesis to perform the design of these systems, and thus it would not be possible to include accurate estimates for the mass and cost of these systems. Therefore, though the extra mass and cost of the monitoring and cooling systems are noted qualitatively, they are excluded from the quantitative analysis.

Table 4-3: A123 Systems' ANR26650MI Lithium-Ion Battery Cell Parameters

Capacity	2.3 Ah
Maximum Voltage	3.6 V
Nominal Voltage	3.3 V
Maximum current discharge rate	70 A
Maximum current discharge rate (pulse for 10 seconds)	120A
Maximum current charge rate	10 A
Internal Resistance @ 10A DC	0.01 Ω
Mass	70 g
Low Volume Cost (per cell)	\$18.33

A123 Systems states a maximum continuous current limit of 70A per cell and a maximum pulse current limit of 120A per cell [18]. However, since the conditions of this test are not known or available, it must be assumed that these maximum currents were obtained under ideal conditions. Also, in any design, and especially in a vehicle, a margin of safety must be included. Therefore, to include a margin of safety and to account for non-ideal conditions (such as high ambient temperatures), the maximum current limit for the battery cell is set to 80A in this study. The maximum recommended charge rate is 10A [18].

For the battery ESS topology, the $batt_s$ variable ranges from 105 to 115, since at 3.3V/cell, this gives a nominal bus voltage range of 346.5V to379.5V (with room to charge and discharge without violating the motor inverter voltage limits). For the battery-ultracapacitor ESS (Topology 1), a 2-quadrant DC/DC converter is used between the battery and the high-voltage bus, and the battery voltage is chosen to be lower than the bus voltage. The $batt_s$ variable ranges from 75 to 100. When $batt_s$ = 75, which corresponds to a battery terminal voltage of 247.5V, the ultracapacitor can always discharge to 250V, making optimal use of the stored energy available between the motor inverter voltage limits. However, when the battery's voltage drop at high current is taken into account, it can be seen that a higher terminal voltage battery (100 × 3.3 = 330V) can still allow the ultracapacitor to make full use of its energy storage during high power demands, since both the battery and the ultracapacitor usually provide power during these times. The advantage of using more batteries in series is an increase in power leading to faster acceleration, whereas the disadvantage is that when the bus power returns to zero before becoming negative during regenerative braking, the ultracapacitor is charged by the battery to the battery open-circuit voltage. This means that when regenerative braking begins, the ultracapacitor voltage will be higher than 250V, leaving less room available for energy storage from regenerative braking. For the novel battery-ultracapacitor ESS (topology 2), the range for $batt_s$ is 100 to 115. The lower limit is derived in Section 5.6 and is based on ensuring the battery terminal voltage is above the lower inverter voltage limit (250V) when the battery is providing maximum positive power.

Battery degradation is difficult to quantify, as the degradation will be different for each specific battery type, and limited data is available from A123 Systems. Cycle tests show a 5% reduction in capacity after 1000 deep cycles at 2.3-A charge and discharge at 25°C, and a 24% reduction in capacity after 1000 deep cycles at 3-A charge and 5-A discharge at 60°C [18]. However, in a hybrid vehicle, batteries are regularly subjected to much higher currents, which degrades the battery even faster, though deep cycle charges and discharges are rare. Nevertheless, it can be qualitatively stated that the battery degrades more quickly when cycled more frequently and at higher currents.

4.2.5 DC/DC Converter Model

The DC/DC boost converter model used to process fuel cell power in the powertrain is based on the circuit shown in Figure 3-2. For the bi-directional battery DC/DC converter, an anti-parallel switch is placed across the boost diode to create a two-quadrant converter, as shown in Figure 4-5. To reduce complexity and run-time, the converter models in the vehicle simulator are based on hard-switched designs. However, soft-switching can be used to increase efficiency and/or reduce mass. Chapter 6 reviews soft-switching methods from the literature and presents a novel regenerative snubber circuit with experimental results.

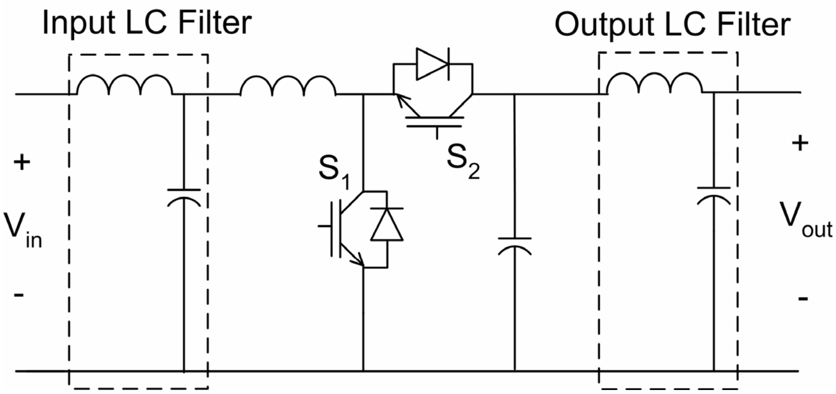

Figure 4-5: A bi-directional DC/DC converter

It is important to use an accurate DC/DC converter model because the dynamic converter losses will have an effect on the overall vehicle fuel economy [53] and a high-power converter can add significant mass and cost to the powertrain. For example, to determine the actual advantage of using a smaller fuel cell or battery, the fact that the associated DC/DC converter will be lighter and cheaper must be taken into account. To accomplish accurate DC/DC converter modeling, the following three approaches have been taken:

1) The high-power inductors are a main contributor to mass and cost in the converter [39], and the inductor size depends on voltage boost, average DC current, and AC ripple current. Thus, design rules were developed to derive an equation for the minimum inductance of the main boost inductor based on the minimum input voltage and the maximum input current. First, the current level where the converter operation is on the verge of discontinuity, $I_{critical}$, is chosen to be 10% of the maximum input current. At this operating point, the current ripple in the inductor has a peak-to-peak value of ($2I_{critical}$). Equations (4-10) to (4-14) are then used to find L_{min}.

$$\frac{V_{out}}{V_{in}} = \frac{1}{1-d} \tag{4-10}$$

$$Maximum\ Duty\ Cycle = d_{\max} = \frac{V_{out,\max} - V_{in,\min}}{V_{out,\max}} \tag{4-11}$$

$$V_{out,\max} - V_{in,\min} = L_{\min}\left(\frac{di}{dt}\right)_{\max} \tag{4-12}$$

$$\left(\frac{di}{dt}\right)_{\max} = \frac{2I_{critical}}{T(1-d_{\max})} \quad \textbf{(4-13)}$$

$$L_{\min} = \frac{V_{out,\max}V_{in,\min} - V_{in,\min}^{2}}{2V_{out,\max}I_{critical}f} \quad \textbf{(4-14)}$$

The switching frequency, *f*, is constant at 10kHz, and $V_{out,max}$ = 400V. The maximum output voltage is set lower than the maximum bus voltage of 425V because the fuel cell and/or battery will rarely be operating at very high bus voltages, since these voltages mainly occur at the end of a deceleration or at the beginning of an acceleration and the ultracapacitor (or battery directly connected to the bus in the FC-B topology) is mainly accepting or providing power at these times. Furthermore, if the fuel cell and/or battery are operating when the bus voltage is above 400V, they will surely not be at maximum power (i.e., minimum voltage) since constant torque, not constant maximum power, is required from the motor at the beginning of an acceleration.

Based on varying the two inductor design variables (inductance and average DC current – ripple current is assumed constant at 20%), 20 in-depth inductor designs were performed. These designs resulted in the corresponding mass, DC resistance, and core losses for each design. The 20 results were expanded using interpolation to generate a 2-dimensional look-up table for the mass and losses of each inductor. For the filter inductors, a similar procedure was used, but the inductance was easily calculated based on a constant filter capacitance. The inductor cost is estimated at $66/kg, for high-volume production [54].

2) The IGBT and diode models and costs are based on real components from Powerex [55]. The models are based on the dual IGBT modules: CM100DUS-12F, CM150DUS-12F, CM200DU-12NFH, CM300DU-12NFH, and CM400DU-12NFH. The $V_{CE,sat}$ curves, $V_{FW,diode}$ curves, reverse recovery losses, and switching losses are extracted from the device datasheets. The switch used for a particular simulation run is chosen as the device with the closest (but not lower) current rating to the maximum fuel cell and battery currents for that run.

3) To calculate converter efficiency, and hence output current, many vehicle models [41][42] use a look-up table that calculates the efficiency based on the input current of the converter. This is inaccurate in general because the efficiency is also a function of the voltage boost required. Also, since in this study the converter components are different for each simulation run, a more accurate way

to determine output current is to use the fundamental equations of the boost converter (derived from equations in [56] by adding the voltage drop characteristics of semiconductor devices):

$$Duty\ Cycle = d = \frac{V_{out} - V_{in} + V_{FW,diode}}{V_{out} + V_{FW,diode} - V_{CE,sat}} \tag{4-15}$$

$$P_{conduction\ loss,IGBT} = d \times V_{CE,sat} \times I_{in} \tag{4-16}$$

$$P_{conduction\ loss,diode} = (1-d) \times V_{FW,diode} \times I_{in} \tag{4-17}$$

$$I_{out} = \frac{I_{in}V_{in} - P_{total\ losses}}{V_{out}} \tag{4-18}$$

where curves for $V_{FW,diode}$ and $V_{CE,sat}$ are obtained from the Powerex datasheets. In addition to conduction losses, switching losses in the IGBT and diode, inductor losses, and capacitor losses are included in the calculation of $P_{total\ losses}$.

Based on the findings in Section 3.1, the mass multiplication factor of the converter is set to 1.85 and the cost multiplication factor of the converter is set to 1.7. This means that the mass and cost of each converter is the sum of the mass and cost of the basic components (IGBT, diode, inductors, and capacitors) multiplied by the appropriate factor to account for copper bus bars, connectors, the enclosure, and the cooling system.

The models of the diode and switch used in the novel FC-B-UC topology are also based on real components. The diode connected to the battery in the novel FC-B-UC topology is modeled from the Powerex diode LS411260 (0.816kg, \$90, rated for 600A), which has a low forward conducting voltage. The heatsink for the diode is estimated to be \$20 and have a mass of 0.8kg. The switch used to charge the battery from regenerative braking energy in the novel FC-B-UC topology (Option 2) is modeled from the International Rectifier IGBT IRG4PC50S (6g, \$5.25, rated for 40A). The total cost of this switch is estimated at \$20.25 to include the cost of the IGBT, driver, driver circuitry, and heat sink, and the total mass for these components is estimated at 0.206kg. The low-power DC/DC boost converter for battery charging is estimated to cost \$140 (including \$10 for the heatsink) and have a mass of 1kg (plus 0.3kg for the heatsink). The constant efficiency is estimated at 96%.

4.3 Control Strategies

Many studies have been conducted on optimizing control strategies for fuel cell vehicles [30][44][45][46]. In reality, real-time control strategies (those which do not know the drive cycle a priori) can only produce near-optimal results [30]. In this thesis, the control strategies developed for each vehicle are based on rules in order to make the best use of the power sources given their power, energy, efficiency, and durability characteristics. A similar control architecture is used for all vehicles but the FC-B vehicle control is based on vehicle velocity whereas the control strategy for the other three vehicles is based on ultracapacitor voltage. Two parameters are varied in each control strategy to allow for the controller to be chosen for each plant that results in the highest fuel economy, while ensuring $E_{\Delta SOC}$ is greater than or equal to zero (since an ESS which is allowed by the control strategy to continually charge up can quickly become fully charged and unable to accept the maximum amount of regenerative braking energy available).

4.3.1 General Control Architecture

This section discusses the general control strategies that are used for all vehicle types in the simulation. The following two sections present additional details for the two FC-B-UC vehicle topologies, including the methods used for splitting the general ESS power requests between the battery and the ultracapacitor. The goal of the general control architecture is to provide similar control for all vehicle types, so that a fair comparison can be made based on the fuel economy results.

Figure 4-6 shows a block diagram of the general control architecture for positive power requests. The "× ÷" block divides the "×" input by the "÷" input. The control architecture ensures that the current limits of the fuel cell, battery, and ultracapacitor are not exceeded using the saturation blocks (shown in Figure 4-6) to calculate the available fuel cell and ESS power. The motor inverter current request is calculated from the available fuel cell and ESS power so that the power limits of these sources are not exceeded. An adaptive low-pass filter is used to separate the desired electrical power into a fuel cell component and an ESS component. The general philosophy behind the use of the adaptive filter is to ensure that the ESS provides more power at the beginning of an acceleration (due to the fuel cell power increase rate limit and to make room in the ESS for the capture of regenerative braking energy) and less power when cruising at a relatively steady velocity (since it is inefficient to use the ESS excessively due to the losses involved in charging and discharging).

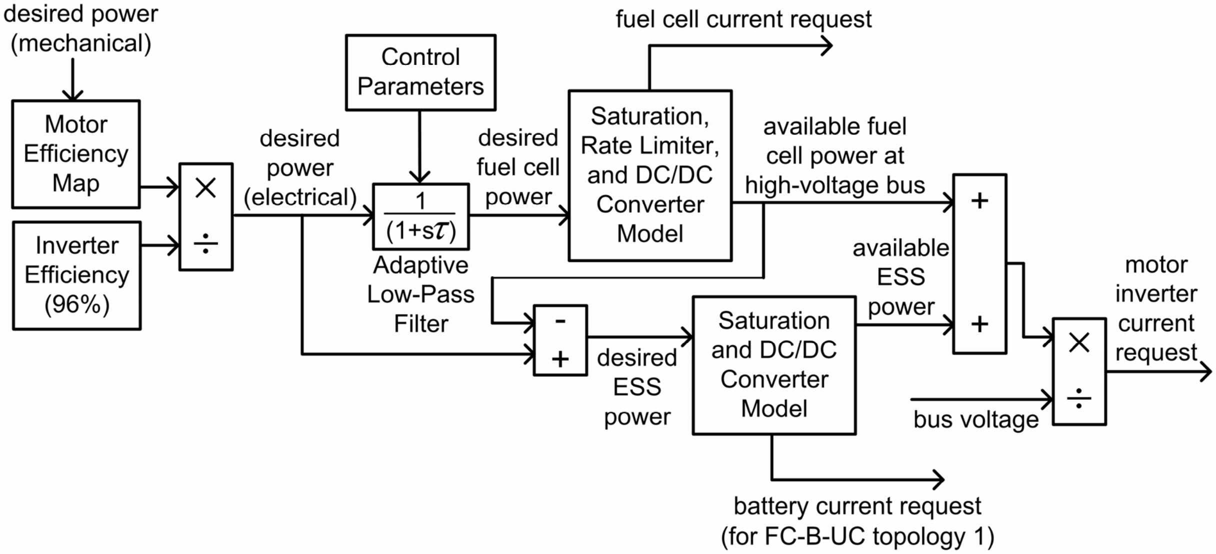

Figure 4-6: General control architecture

For the FC-B and FC-B-UC vehicles, extra functionality is added such that when the desired fuel cell power is less than a certain level (4kW in this case), the desired fuel cell power is set to zero and the ESS provides all of the required power. This ensures that the fuel cell is not operated in the low-efficiency region at very low power. In reality, these efficiency gains should be weighed with the decrease in fuel cell durability resulting from repeatedly turning the fuel cell on and off, which is beyond the scope of this thesis. The FC-UC vehicle does not include this functionality because there is generally not enough energy storage available in the ultracapacitor to propel the vehicle at low speeds.

In the case of the FC-B-UC vehicles, it is desirable to use the ultracapacitor more often, since it is more efficient and has a longer lifetime than the battery. Thus, the control method for the FC-B-UC vehicles is the same as control method for the FC-UC vehicle, as the same goal exists: use more power from the ultracapacitor when the ultracapacitor voltage is high (so that there is room to capture regenerative braking energy) and use less power from the ultracapacitor when the ultracapacitor voltage is low to prevent depleting the ultracapacitor fully if possible. Thus, for the FC-UC and FC-B-UC vehicles, the ultracapacitor terminal voltage, v_{olt}, is chosen as the control input for the adaptive filter. When the ultracapacitor terminal voltage is high, a larger filter time constant, τ, is used and thus the ESS component of the required power is large and the fuel cell provides little or no power. When the ultracapacitor voltage is low, a smaller time constant is used to ensure it is not further depleted unless necessary to provide the desired electrical power.

For the FC-B vehicle, the vehicle velocity, v_{el}, is chosen as the control input, as a similar effect will be obtained as using the ultracapacitor voltage as the control input for the UC-based vehicles: more battery power is provided at the beginning of each acceleration (when the vehicle's velocity is relatively low) and little or no battery power is provided when the vehicle is cruising at typical city or highway speeds.

For all vehicle types, the time constant τ is blended smoothly from "high" to "low" using the two control parameters, *filter* and *scale* (<1), which are varied in the multiple simulation runs to obtain the best controller for each plant. The range of the control input, v_{olt} or v_{el}, which can be labelled as v in general, is divided into n = 9 sections, as shown in Table 4-4. Table 4-4 shows how *filter* and *scale* are used to determine the time constant for a given vehicle and section number n. For example, for the FC-UC vehicle, $\tau = filter \times scale^3$ for the section V_5 = 380 V. For FC-UC and FC-B-UC vehicles, *filter* is varied from 3 to 18 and for FC-B vehicles, *filter* is varied from 18 to 30. The *scale* parameter determines how quickly the time constant decreases as n increases. In the simulation runs, the *scale* parameter is varied between 0.3 and 0.8 for all vehicle types.

Table 4-4: Time Constant Calculation for Adaptive Filter

	FC-UC and FC-B-UC Vehicles		**FC-B Vehicle**	
n	**Ultracapacitor Voltage, V**	**Time Constant (τ)**	**Vehicle Velocity, km/h**	**Time Constant (τ)**
1	$V_1 = 420$	*filter*	$V_1 = 0$	*filter*
2	$V_2 = 410$	*filter*	$V_2 = 5$	*filter*
3	$V_3 = 400$	*filter*	$V_3 = 10$	$filter \times scale^2$
4	$V_4 = 390$	*filter*	$V_4 = 15$	$filter \times scale^3$
5	$V_5 = 380$	$filter \times scale^3$	$V_5 = 20$	$filter \times scale^4$
6	$V_6 = 370$	$filter \times scale^6$	$V_6 = 25$	$filter \times scale^5$
7	$V_7 = 360$	$filter \times scale^6$	$V_7 = 30$	$filter \times scale^6$
8	$V_8 = 350$	$filter \times scale^6$	$V_8 = 35$	$filter \times scale^7$
9	$V_9 = 340$	$filter \times scale^7$	$V_9 = 40$	$filter \times scale^7$

In order to avoid having abrupt changes in τ as the ultracapacitor voltage or vehicle velocity changes, a Gaussian function, shown in Figure 4-7, is used to smoothly blend the results from the $n = 1$ to 9 sections. In Equations (4-19) to (4-21), v represents the general control input (ultracapacitor voltage or vehicle velocity depending on the vehicle type), V_n represents the constant for each section n as shown in Table 4-4 (e.g., 380 for V_5 in FC-UC vehicle), and W_n represents the weighting for each section, as obtained from the Gaussian function in Equation (4-19) and Figure 4-7. P_e represents the total electrical power request, and P_{fn} is the result of P_e being filtered by each low-pass filter n (using the appropriate τ from Table 4-4 for each section n). $P_{f,overall}$ is the overall filtered result which is a combination of each P_{fn} using the Gaussian function weighting, as shown in Equation (4-20). Finally, the pseudo-code in Equation (4-21) ensures that the effect of the filtering is to use the ESS to provide power to the motor when desired (by requesting less fuel cell power than required at the motor) and not to charge the ESS unintentionally from the fuel cell when $P_{f,overall} > P_e$.

$$W_n = e^{\left(-\frac{(v-V_n)^2}{50}\right)} \tag{4-19}$$

$$P_{f,overall} = \frac{\sum_{9}^{n=1} W_n P_{fn}}{\sum_{9}^{n=1} W_n} \tag{4-20}$$

```
if $P_{f,overall} \le P_e$ then
    desired fuel cell power $= P_{f,overall}$
else                                                    (4-21)
    desired fuel cell power $= P_e$
end if
```

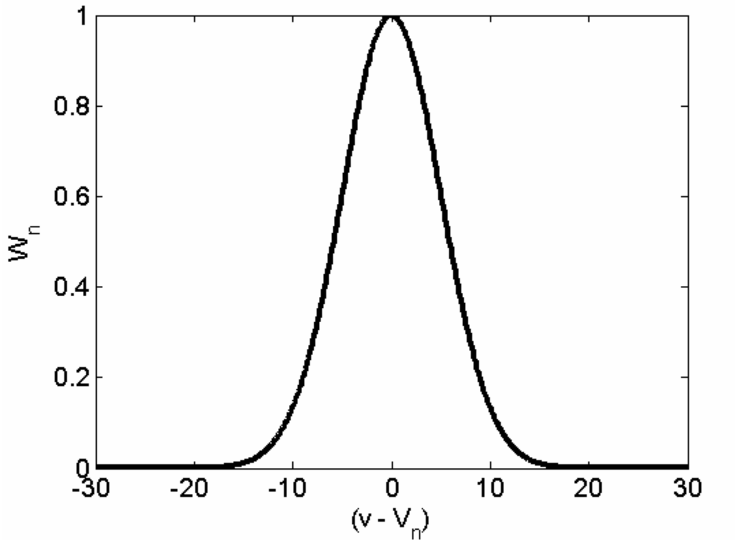

Figure 4-7: Gaussian function to determine weighting W_n for each section n based on control input v

The preceding control architecture calculates the desired fuel cell power signal shown in Figure 4-6 for positive power requests. When the desired power is negative (i.e., when the vehicle is braking) an algorithm must be used to split the power between mechanical braking and regenerative braking components. Mechanical braking is required because at times, the inertia of the induction motor can prevent it from providing all of the negative braking power needed to satisfy the driver's request. For example, at high speeds, the motor is generating higher electro-motive force (EMF) and thus has more ability to provide negative torque as required. However, at low speeds, a large amount of torque is needed to approach and reach a stop, and this torque is usually not available from the motor due to the lower EMF produced at lower speeds. ADVISOR uses a speed-mechanical braking map, as shown in [57], to determine the power split between mechanical and regenerative braking. For this vehicle simulator, a similar map, shown in Figure 4-8 is used to provide this power split during braking. Also, when the ESS SOC is close to 100%, mechanical braking is used for all of the braking requirements, so that the ESS is not overcharged.

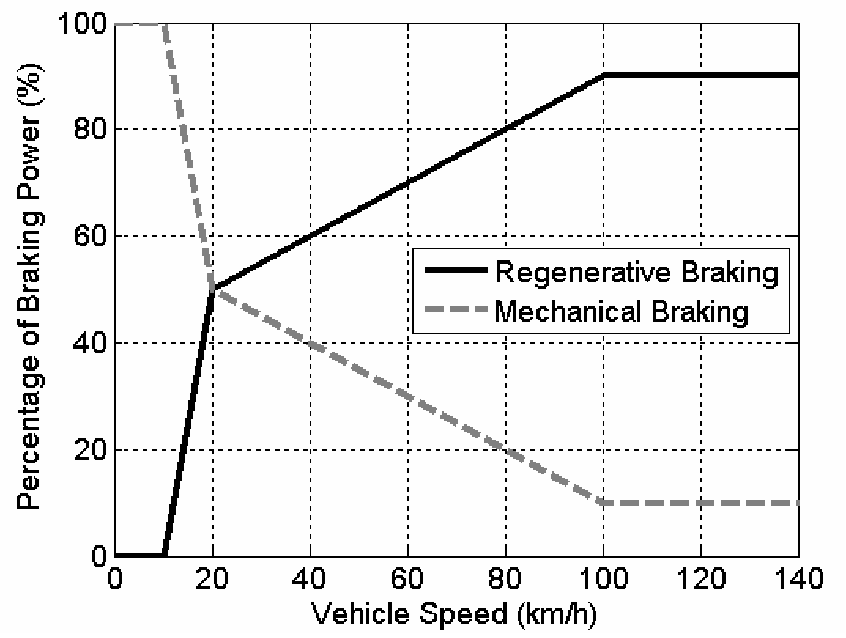

Figure 4-8: Map for determining the mechanical and regenerative braking power components

There are two more control rules that are common to all the vehicle types. The first rule is that the ESS is not charged by the fuel cell at any point during the drive cycle for this study. Common ESS-charging strategies include charging when the ESS SOC is low and when the fuel cell efficiency is high. However, it was found that including ESS-charging from the fuel cell in the calculation of the fuel economy introduced some unfairness because over the relatively short drive cycle under test (490 seconds) some vehicles would be charged more than others and possibly at efficiencies different from the average estimated efficiency for each vehicle type, ε_{path}.

The second common rule is that the controller requests a maximum of 136kW at the inverter, or the high-voltage bus. When the efficiencies of the inverter (96%) and the motor (about 92% at this power level) are considered, the result is 120kW of mechanical power out of the motor. This corresponds to using two 60-kW motors as specified in [25]. Without this limit, very large ESS systems (i.e., with many batteries and/or ultracapacitors in parallel) would obtain a fast acceleration time by putting out very large amounts of power to compensate for the high ESS mass. However, since the mass and cost of the inverter and motor are fixed in this study, these results would be misleading since they would have been obtained using a much larger motor than is required in vehicles with smaller and lighter ESSs. The maximum power level was tested for validity as follows: a 2000kg FC-B vehicle was simulated with the 136kW bus power limit, and the 0-60mph resulting acceleration time was found to be 7.718 seconds, which is less than the 8.9 second 0-60mph acceleration time of the stock ICE Equinox. Therefore, it can be concluded that this power limit is reasonable as it allows improved acceleration times over the stock vehicle. It should be noted that this 136-kW power limit is only reached in the acceleration tests, as the power levels required in the drive cycle simulation are much lower (< 60kW).

4.3.2 Control of Fuel cell-Battery-Ultracapacitor (FC-B-UC) Vehicle – Topology 1

The philosophy of the chosen control strategy is to use the ultracapacitors to handle the bulk of the transient power demands, including acceleration and braking requirements. This ensures that the high efficiency and high durability of the ultracapacitors are fully utilized, and the lifetime of the battery is extended as a result of not being subjected to many high current charges or discharges. Thus, the "desired ESS power" from Figure 4-6 is essentially equal to the desired ultracapacitor power in most cases so that the ultracapacitor provides all of the ESS (transient) power within its current and voltage limits. If the ultracapacitor voltage reaches the lower limit (250V), the battery provides the remaining power required. The battery also provides power if the fuel cell cannot meet its power request due to current limitations during times of very high power demand (e.g., hard acceleration).

When the required motor power is negative, the ultracapacitor accepts the regenerative braking energy at a rate below its current limit (85A per ultracapacitor string) as long as the ultracapacitor voltage is below 425V. Beyond this point, the battery accepts any extra regenerative braking energy below its charging current limit (10A per battery string).

4.3.3 Control of Fuel Cell-Battery-Ultracapacitor (FC-B-UC) Vehicle – Topology 2

As mentioned in Section 2.6, the regenerative braking control strategy for the novel topology is very straightforward. For Option 1 (without battery switch), the ultracapacitor absorbs all of the regenerative braking energy until its voltage reaches 425V, and then mechanical braking takes over if required. For Option 2 (with battery switch), if the battery and ultracapacitor terminal voltages are within about 2V of each other (i.e., the battery provided power during the previous acceleration) then the switch is turned on when the inverter power becomes negative during braking. The battery and ultracapacitor both absorb regenerative braking energy until the battery upper current limit is reached, at which point the switch is opened and the ultracapacitor absorbs the rest of the braking energy. If the ultracapacitor is not discharged down to the battery voltage during the previous acceleration, then the ultracapacitor absorbs all regenerative braking energy up to 425V, just as for Option 1.

There are two positive-power control rules that are applied based on whether the battery is providing power. When the battery is not providing power, the control rule is very simple: the ESS saturation block in Figure 4-6 saturates the ESS power (i.e., the ultracapacitor power) to the maximum ultracapacitor current multiplied by the instantaneous ultracapacitor terminal voltage, v_{uc}. However, when the battery is also providing positive power, an extra calculation is required within the ESS saturation block to ensure the battery and ultracapacitor current limits are not exceeded (since it is not possible to independently control the battery and ultracapacitor currents). The derivation of the required calculation is based on the circuit shown in Figure 4-9. The required inputs for the calculation are: internal battery voltage (v_b), internal ultracapacitor voltage (v_c), battery internal resistance (R_b), ultracapacitor internal resistance (R_c), forward diode voltage drop (V_d), which can be approximated as a constant or read from a look-up table, and the total ESS current output desired, i_{ESS}. The internal ultracapacitor voltage can be easily found since the terminal voltage and output current are measurable, and the internal ultracapacitor resistance is known. The internal battery voltage can be found using the battery SOC, which is monitored in any topology.

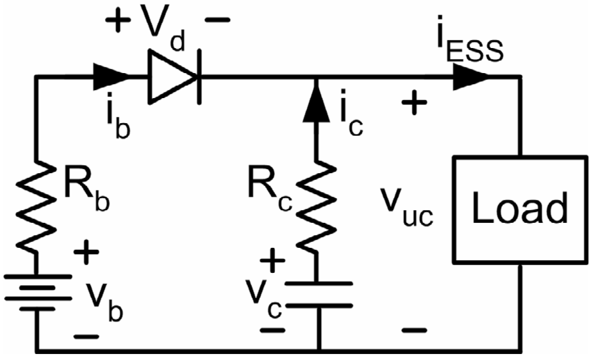

Figure 4-9: B-UC circuit diagram for deriving maximum ESS power available

KVL and KCL are applied to the circuit of Figure 4-9 to obtain Equations (4-22) and (4-23).

$$KVL: \quad v_c - i_c R_c = v_b - i_b R_b - V_d \qquad \textbf{(4-22)}$$

$$KCL: \quad i_c + i_b = i_{ESS} \qquad \textbf{(4-23)}$$

The expression for i_b is found by combining Equation (4-22) and Equation (4-23) and solving for i_b, as shown in Equation (4-24). The same procedure is used to solve for i_c in Equation (4-25).

$$i_b = \frac{v_b - v_c - V_d + i_{ESS} R_c}{R_c + R_b} \tag{4-24}$$

$$i_c = \frac{v_c - v_b + V_d + i_{ESS} R_b}{R_c + R_b} \tag{4-25}$$

Now, the battery current in Equation (4-24) is set to the maximum allowable current ($i_b = i_{b,max}$), and Equation (4-24) is re-arranged to solve for the total ESS current available when the battery is providing maximum current, i_{ESS1}, as shown in Equation (4-26). Similarly, i_c is set to $i_{c,max}$ in Equation (4-25) and the total ESS current available, i_{ESS2}, is calculated as shown in Equation (4-27).

$$i_{ESS1} = \frac{i_{b,\max}(R_c + R_b) - v_b + v_c + V_d}{R_c} \tag{4-26}$$

$$i_{ESS2} = \frac{i_{c,\max}(R_c + R_b) - v_c + v_b - V_d}{R_b} \tag{4-27}$$

Since the goal is to ensure that neither $i_{c,max}$ nor $i_{b,max}$ is exceeded, the total ESS current requested should be the minimum of i_{ESS1} and i_{ESS2}. This means that the block will saturate the total desired ESS current such that one current limit is met, but neither the limit for the battery nor that for the ultracapacitor is exceeded. Thus, the final calculation for the available ESS power signal from the ESS saturation block in Figure 4-6 is as shown in Equation (4-28).

$$available\ ESS\ power = v_{uc} \times \min(i_{ESS1}, i_{ESS2}) \tag{4-28}$$

Finally, although the battery is not charged from the fuel cell in this study as previously mentioned, the battery-charging conditions are described below to emphasize the simplicity of the charging algorithm. The battery is charged from the fuel cell at a constant power level (e.g., 1kW in this vehicle) when the following conditions are met:

1) The battery is not providing power to the motor.
2) The fuel cell is operating in a high-efficiency region.
3) The battery state of charge is below 99%.

This battery charging strategy helps to ensure that the battery never becomes depleted, as it is often being trickle-charged. The trickle-charge approach also helps to lengthen the battery lifetime.

4.4 Combined Plant/Controller Optimization

4.4.1 Objective Function, Parameters, and Constraints

The objective function chosen for the study, $F(x)$, is given by Equation (4-29). It combines aspects of performance (measured by acceleration time), fuel economy, and powertrain cost.

$$F(x) = (0.2\times(1-accel)) + (0.45\times mpgge) + (0.35\times(1-cost)) \qquad \textbf{(4-29)}$$

The goal is to maximize $F(x)$. The terms *accel*, *mpgge*, and *cost* refer to normalized scores between 0 and 1, based on the minimum and maximum quantities obtained. For each term, the score of 1 corresponds to the highest quantity obtained, such as the longest acceleration time, the highest fuel economy, or the highest cost. The coefficients of the terms in $F(x)$ were chosen to reflect the importance of maximizing fuel economy and minimizing cost, but can be generalized to any values summing to one to reflect different design priorities. The objective function is used to distinguish the top vehicle designs for each vehicle type from the thousands of simulations run. Then, the top group of vehicle designs for each vehicle type (using the optimal controller for each vehicle design) is analyzed in more detail. The vehicle completes the first 505 seconds of the Federal Urban Driving Schedule (FUDS), shown in Figure 4-10 [43], to obtain the fuel economy score, and a 0-60mph acceleration test to obtain the acceleration score. A summary of the variables and their bounds used in the parametric study is given in Table 4-5.

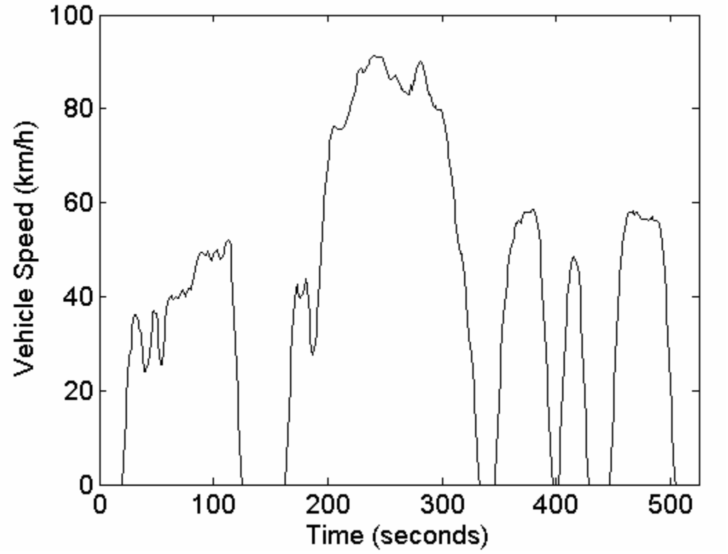

Figure 4-10: First 505 seconds of the Federal Urban Driving Schedule

Table 4-5: Parametric Study Variables and Bounds

Vehicle Topology	Variable	Lower Bound	Step Size	Upper Bound
FC-B	*fc_kW*	40	5	80
	$batt_s$	105	5	115
	$batt_p$	1	1	7
	filter	10	2	30
	scale	0.3	0.1	0.8
FC-UC	*fc_kW*	40	5	80
	uc_p	4	1	12
	filter	3	1	16
	scale	0.3	0.1	0.8
FC-UC-B Topology 1 (from literature)	*fc_kW*	40	5	80
	$batt_p$	1	1	6
	$batt_s$	75	5	100
	uc_p	1	1	6
	filter	3	1	16
	scale	0.3	0.1	0.8
FC-UC-B Topology 2 (novel topology – Options 1 and 2)	*fc_kW*	40	5	80
	$batt_p$	1	1	6
	$batt_s$	100	5	115
	uc_p	1	1	6
	filter	3	1	16
	scale	0.3	0.1	0.8

4.4.2 Parametric Study Results

In terms of fuel cell size, the results show that the vehicles with the highest objective function score, regardless of the ESS type, have a fuel cell size of 40kW, for all fuel cell costs from \$225/kW to \$4500/kW. This result can be explained as follows: since cost is a large factor in this optimization, and the fuel cell is the most costly source of power in the vehicle, a smaller and lower-cost fuel cell is required to meet the optimization objectives. Most automobile manufacturers use a significantly larger fuel cell for a smaller vehicle platform [7]. However, the results reported here show that when costs are considered, a smaller fuel cell can still give the performance required (assuming there is an adequately-sized ESS) while minimizing cost. This result holds even when fuel cell costs are assumed to drop to \$225/kW. It is projected that a larger fuel cell size would only become cost-effective if the fuel cell costs drop below the ESS costs, which is far from the case today. For the remainder of this study, the fuel cell cost is fixed at \$400/kW and the fuel cell size is fixed at 40kW. Thus, the fuel cell cost is fixed at \$16,000 and the fuel cell DC/DC boost converter cost is fixed at \$2343.60. Therefore, the following cost comparisons for each vehicle exclude these fixed costs and instead consist of the battery and/or ultracapacitor cost and the power electronics used with the ESS in each topology.

To begin the analysis of all the ESS options, an in-depth comparison of the results for the three battery-ultracapacitor vehicles (Topology 1 from the literature, novel Topology 2 without switch – Option 1, and novel Topology 2 with switch – Option 2) is presented. The most promising results are then compared to the best results for the fuel cell-battery and fuel cell-ultracapacitor vehicles. For each vehicle powertrain design, the optimal controller has been chosen (i.e., the controller which resulted in the highest fuel economy).

Some general conclusions can be made regarding the effect of the number of battery cells in series ($batt_s$) for both Topologies 1 and 2. For Topology 1, when $batt_s$ is increased from 75 to 100 (with $batt_p$ and uc_p held constant) the simulation results are affected in three ways:

1) The 0-60mph acceleration time decreases due to the extra power available from the higher number of batteries.

2) The fuel economy decreases slightly. This is the result of two contributing factors: (i) the ESS has a higher overall mass and thus more energy is required for the vehicle to follow the drive cycle, and (ii) the resistance of each battery string is increased and thus there are slightly more losses in the battery pack.

3) The ESS cost increases due to the higher number of batteries.

When $batt_s$ is increased from 100 to 115 for Topology 2, similar effects are seen with one main difference: the 0-60mph acceleration time decreases and the ESS cost increases, but the fuel economy decreases *significantly* when uc_p = 2 or 3. The explanation of this effect is as follows: the available amount of regenerative braking energy cannot be fully absorbed by the ESS when the nominal battery voltage is relatively high because a high battery voltage prevents the ultracapacitor from discharging enough during an acceleration to create sufficient room for the forthcoming regenerative braking energy. Thus, for the remainder of this study, $batt_s$ for the novel FC-B-UC Topology 2 is set to 100, as this generally guarantees a high fuel economy result. It is important to note that the fact that the overall optimal number of battery cells in series in this case is equal to the minimum number possible (100) is not a general conclusion, since different drive cycles or vehicle systems (i.e., with different acceleration/deceleration profiles or voltage constraints) will yield different conclusions. This is one of the reasons that a general analytical optimization method is derived in Chapter 5.

Therefore, the number of battery cells in series for Topology 2 has been fixed for the ensuing comparison, but the number of battery cells in series for Topology 1 does not have to be fixed since the advantages and disadvantages of increasing $batt_s$ magnify in small, smooth increments as $batt_s$ increases. It should be noted that Topology 1 can in some cases achieve a faster acceleration time than Topology 2 with the same $batt_s$ even though the vehicle has a higher mass because both the battery and ultracapacitor can put out high power at the very beginning of the acceleration in Topology 1, whereas in Topology 2, the ultracapacitor must be discharged to the battery voltage before the battery can put out power. However, this is not a disadvantage for Topology 2 because when $batt_s$ is reduced in Topology 1 so that the acceleration times are approximately equal, the novel Topology 2 still shows advantages in fuel economy and cost. Therefore, since similar 0-60mph acceleration times are a metric which generally allow for a fair comparison between vehicles (since it may be a requirement/desire of the customer), $batt_s$ for Topology 1 has been chosen in each comparison so that the 0-60mph acceleration time is as close as possible to the corresponding acceleration time of the Topology 2 vehicle with $batt_s$ = 100. The top 7 vehicle groups (in terms of $batt_p$ and uc_p) are compared in Figure 4-11 for each FC-B-UC topology simulated. The box at the bottom of the figure shows which value of $batt_s$ has been chosen for Topology 1 for each group so that the acceleration times for each group are similar across vehicle topologies.

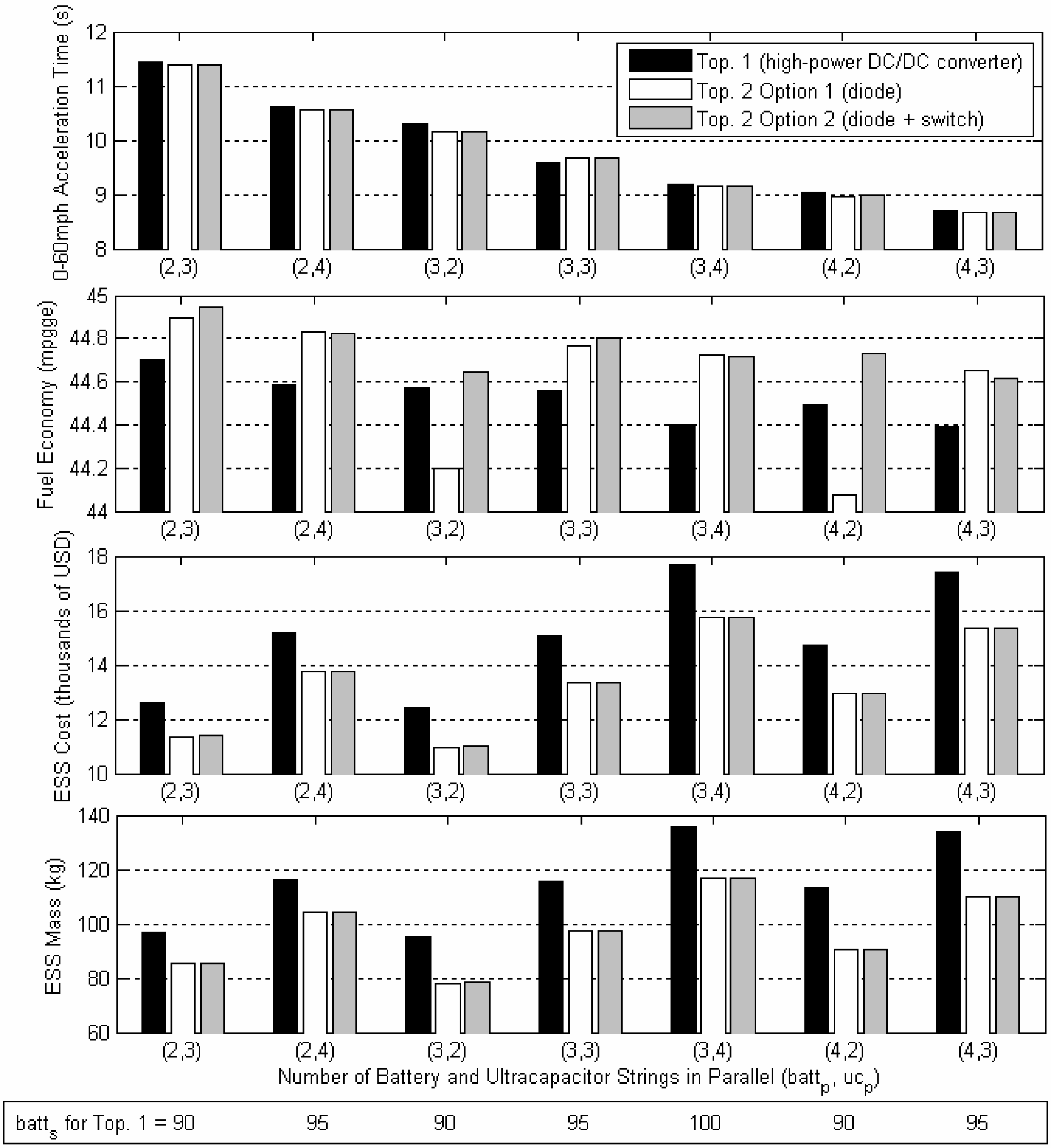

Figure 4-11: Acceleration time, fuel economy, ESS cost, and ESS mass results for the three FC-B-UC vehicles simulated

Figure 4-11 shows that the novel Topology 2 generally scores higher in fuel economy than Topology 1 (from the literature) for each comparison group when the acceleration times are kept approximately the same. The average fuel economy increase for the groups compared is 0.226 mpge or 5.1%. The reasons for these results are: (i) Topology 2 has a lower mass than Topology 1 since no high-power DC/DC converter is required for the battery (which has an average mass of 17kg to 30kg for $batt_\mathrm{p}$ ranging from 2 to 4), meaning less overall energy is used to propel the vehicle, and (ii) there is a higher-efficiency battery discharge path (through the diode) and a higher efficiency battery charge path (through the low-power DC/DC converter and, for Option 2, the switch for accepting regenerative braking energy). The general trend is that fuel economy decreases for both topologies as the number of battery strings in parallel ($batt_p$) increases, due to the extra mass of the batteries.

It can also be seen that there is a large discrepancy between the fuel economy score for Option 1 and Option 2 of the novel Topology 2 when the number of ultracapacitor strings in parallel (uc_p) is low. For $uc_p = 2$, the fuel economy score for Option 1 is significantly lower than that of both Option 2 and Topology 1 because the ultracapacitor is unable to store all of the regenerative braking energy because the capacitance is too low. In Option 2, the anti-parallel switch is present to allow the battery to accept some regenerative braking energy, meaning that the ultracapacitor is not fully charged, and no regenerative braking energy is wasted. However, when $uc_p = 4$, Option 1 (diode-only) achieves a higher fuel economy score because the ultracapacitor has enough capacitance to absorb all of the regenerative braking energy, and there are less losses compared to Option 2 because no regenerative braking energy is stored in the battery (which is generally less efficient than the ultracapacitor). Overall, the novel Topology 2 gives two options, where both or at least one option yields higher fuel economy scores than Topology 1 from the literature.

Figure 4-11 also presents a comparison of ESS cost for each topology within each comparison group. It is shown that for each of the top combinations of ($batt_p$, uc_p) compared, the novel Topology 2 ESS cost (including the battery, ultracapacitor, low-power DC/DC converter, diode, and switch) is significantly less than the ESS cost for Topology 1. The average cost savings for the groups shown is \$1675, or 11.14%. Therefore, the novel Topology 2 fuel cell vehicle design offers an increase in fuel economy (by an average of 5.1% for the designs compared) and a decrease in ESS cost (by an average of 11.14%) compared to the Topology 1 vehicle with the same $batt_p$ and uc_p, while maintaining a similar 0-60mph acceleration time.

To further investigate the operation of each vehicle topology, the ultracapacitor voltage, ultracapacitor current, battery voltage, and battery current are shown for each topology over the drive cycle in Figure 4-12. In Figure 4-12, $batt_p$ = 3, uc_p = 3, $batt_s$ = 100 for Topology 2, and $batt_s$ = 95 for Topology 1 (to keep the acceleration times approximately the same across the different topologies). It can be seen that in all topologies, the ultracapacitor provides the majority of the transient current requirements, as expected, so that the battery is rarely used and its lifetime is extended. Topology 1 does use the battery more frequently than Topology 2 at low power, where the battery is used to propel the vehicle to avoid operating the fuel cell in the low-efficiency region. In Topology 2, ESS current is requested at these times to propel the vehicle, but the ultracapacitor is never discharged enough in this drive cycle for the battery to provide power. Figure 4-12 also shows how the novel Topology 2 Option 2 absorbs regenerative braking current into the battery as opposed to Option 1. The switch is opened when the battery current reaches -30A in this case, which is the battery pack's current limit since the maximum charging current is 10A per battery and this simulation uses three strings of batteries in parallel. It can be concluded that though the use of the anti-parallel switch in Option 2 gives higher fuel economy than Option 1 in some cases (i.e., lower capacitance), it ensures the battery is used more often for high-current charge pulses, decreasing the battery lifetime. Thus, it is important to note that both Option 1 and Option 2 of the novel topology offer some advantages and disadvantages (another disadvantage for Option 2 being the cost and complexity of adding the switch and associated control), and the selection of the optimal option will be based on a particular vehicle design.

It has been shown that the novel diode-based Topology 2 for a fuel cell-battery-ultracapacitor vehicle is an improvement over the best topology selected from the literature, Topology 1 using a high-power DC/DC converter to connect the battery to the high voltage bus, due to the reduction in ESS cost and increase in vehicle fuel economy. Now, the diode-based Topology 2 is compared to the top fuel cell-battery and fuel cell-ultracapacitor vehicles from the parametric study to give an overall analysis of the best fuel cell vehicle designs. To simplify the comparison, Option 2 (diode + switch) is selected for the FC-B-UC vehicle since it achieves high fuel economy for all sizes of ultracapacitor.

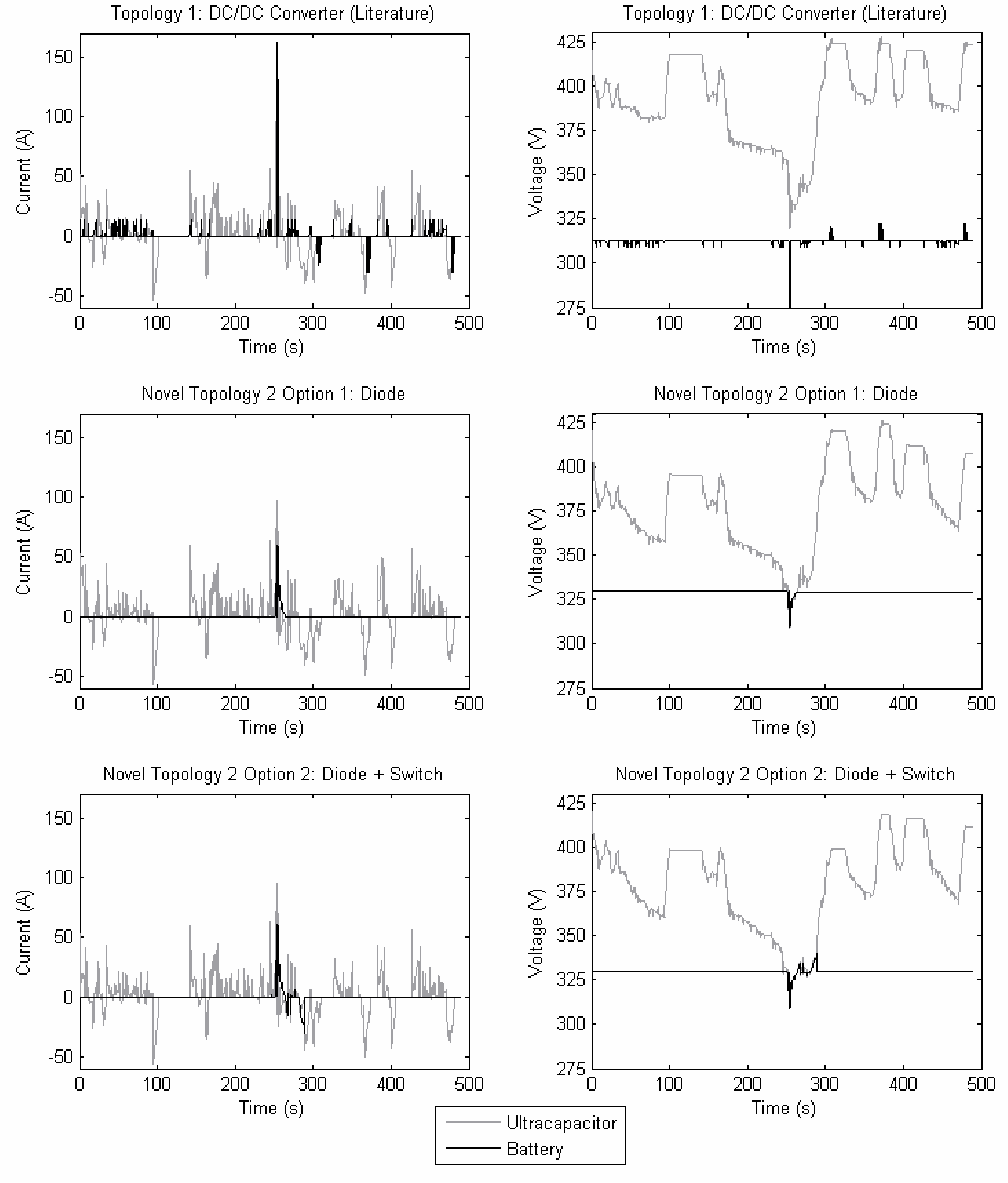

Figure 4-12: Battery and ultracapacitor currents and voltages for the three FC-B-UC topologies

The simulation results of the FC-B parametric study give a unique relationship between the number of battery cells in series ($batt_s$) and the fuel economy. When there is a lower number of battery strings in parallel (e.g., $batt_p$ = 2, 3, or 4), the fuel economy score increases as $batt_s$ increases from 105 to 115. This effect is contrary to the expected result that fuel economy would decrease as $batt_s$ increases due to (i) a higher resistance in the battery pack and thus more I^2R losses during battery charge and discharge and (ii) a higher ESS mass and thus more energy needed to propel the vehicle. One should realize that another factor is also at work: the battery is severely limited in the amount of regenerative braking current it can accept (10A for the batteries used in this study). Thus, when $batt_p$ is low, some regenerative braking energy is wasted since the maximum battery charge current is $batt_p \times 10$. But when $batt_s$ is higher, the battery terminal voltage is higher, and thus more power can be accepted by the battery at the current charge limit of $batt_p \times 10$. This means that over time, less regenerative braking energy is wasted, leading to a higher fuel economy score. However, when $batt_p$ is higher (e.g., 5 or 6), the battery charge current limit of $batt_p \times 10$ is high enough to accept nearly all of the regenerative braking power for all values of $batt_s$ and thus the negative effect of the higher battery resistance and higher ESS mass cause the fuel economy score to decrease as $batt_s$ increases, as initially expected. Therefore, in the following analysis, $batt_s$ has been chosen for each $batt_p$ value such that the highest fuel economy score is used (i.e., $batt_s$ = 115 when $batt_p$ = 3 and $batt_s$ = 105 when $batt_p$ = 5).

Figure 4-13 shows the acceleration time, fuel economy, ESS cost, and ESS mass results for the top three vehicles of each vehicle type compared: FC-B, FC-UC, and FC-B-UC using novel Topology 2 Option 2. The size of each ESS ($batt_s$, $batt_p$, and/or uc_p) are shown within the bar graphs, according to the labelling at the bottom of the figure. The results show that a fuel cell-ultracapacitor vehicle cannot compete with the other two vehicle types when the new lithium-ion batteries are considered for the ESS. In order to attain an acceleration similar to other vehicle types, the fuel cell-ultracapacitor vehicle must have at least 7 or 8 strings of ultracapacitors in parallel to provide the amount of extra energy required for acceleration. This large number of ultracapacitors increases the cost and mass of the vehicle. The higher mass produces fuel economy scores lower than in the other two vehicle types, despite the efficient operation of the ultracapacitors. This phenomenon has also been noted in [15] and [30].

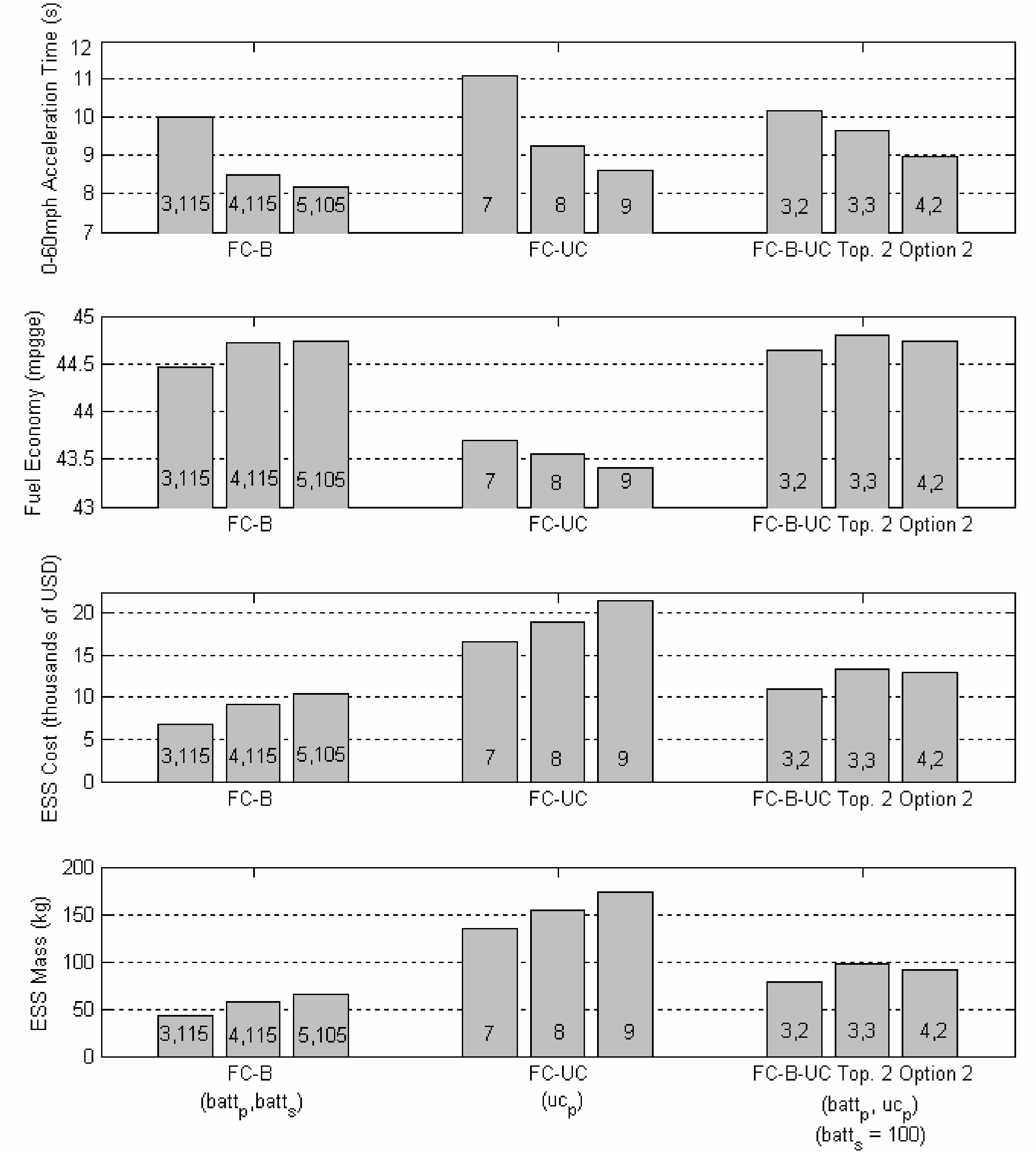

Figure 4-13: Simulation results for top 3 vehicles of each type: FC-B, FC-UC, and FC-B-UC

The results of the study indicate that the main comparison is between the fuel cell-battery and fuel cell-battery-ultracapacitor vehicles. The first item to note is that the FC-B ESS generally has a lower mass than the FC-B-UC ESS for the top optimization results shown in Figure 4-13, and this affects both the acceleration time and the fuel economy comparison. The top FC-B vehicles in this study have generally shorter 0-60 mph acceleration times than the top FC-B-UC vehicles. (It is important to note that the vehicle plant for each type of vehicle could always be designed to match the acceleration performance of another vehicle by increasing the ESS size, but this is not considered in this analysis of optimization results because a larger ESS increases the cost of the vehicle, meaning the optimization objectives are not met.) The generally shorter acceleration times for the FC-B vehicles are due to the lower vehicle mass and the higher battery energy storage. However, it is important to note from a philosophical standpoint that as society moves towards a more enlightened sustainable transportation architecture, metrics such as 0-60mph acceleration times may, and hopefully should, become less important compared to more practical issues such as fuel economy, durability, and cost.

With regards to fuel economy scores, the top FC-B-UC vehicles have a slight advantage over the FC-B vehicles. This is due to the use of the more efficient ultracapacitors, which are especially advantageous during regenerative braking since the charge current is not limited any lower than the discharge current (85A in this study, compared to 10A charge current per battery string). However, the higher vehicle mass of the FC-B-UC vehicles compared to the FC-B vehicles means that more energy is required to propel the vehicle, so the fuel economy advantage is not as large as it could be if the ESS masses were the same.

The initial ESS cost of the FC-B-UC vehicles using the novel Topology 2 (Option 2) is slightly higher than the initial cost of the FC-B vehicles. However, the durability of each system must be examined to reveal the long-term running costs of each vehicle type. It is well-known that frequent battery charging and discharging (especially at higher currents) degrades the battery lifetime [15], though battery manufacturers currently do not publish relevant data for hybrid ESS systems for quantification of this degradation [18].

Figure 4-14 shows the battery current for a selected FC-B and FC-UC-B (Topology 2 Option 2) vehicle for the drive cycle under test. The battery in the FC-B-UC vehicle is used for only a very small fraction of the time that the battery in the FC-B vehicle is used. Further, if Option 1 (diode with no anti-parallel switch) were considered, the battery would be used even less since it would never be charged at high currents during regenerative braking (though the fuel economy would remain approximately the same for the $uc_p = 3$ vehicle). Figure 4-14 also shows that the maximum positive and negative battery current magnitudes are significantly smaller in the FC-B-UC vehicle compared to the FC-B vehicle since the ultracapacitor handles much of the high-power transient requirements.

Since the battery in the FC-B-UC vehicle is used much less frequently than the battery in the FC-B vehicle, it can be expected that the battery in the FC-B-UC vehicle will last much longer than the battery in the FC-B vehicle. Therefore, if the battery in the FC-B vehicle must be replaced one or two times over the life of the vehicle, and the battery in the FC-B-UC vehicle does not have to be replaced due to extended lifetime from the use of the ultracapacitors, it can be concluded by referencing the costs shown in Figure 4-13 that the lifetime cost of the FC-B-UC vehicles is less than the lifetime cost of the FC-B vehicles, despite the higher initial cost.

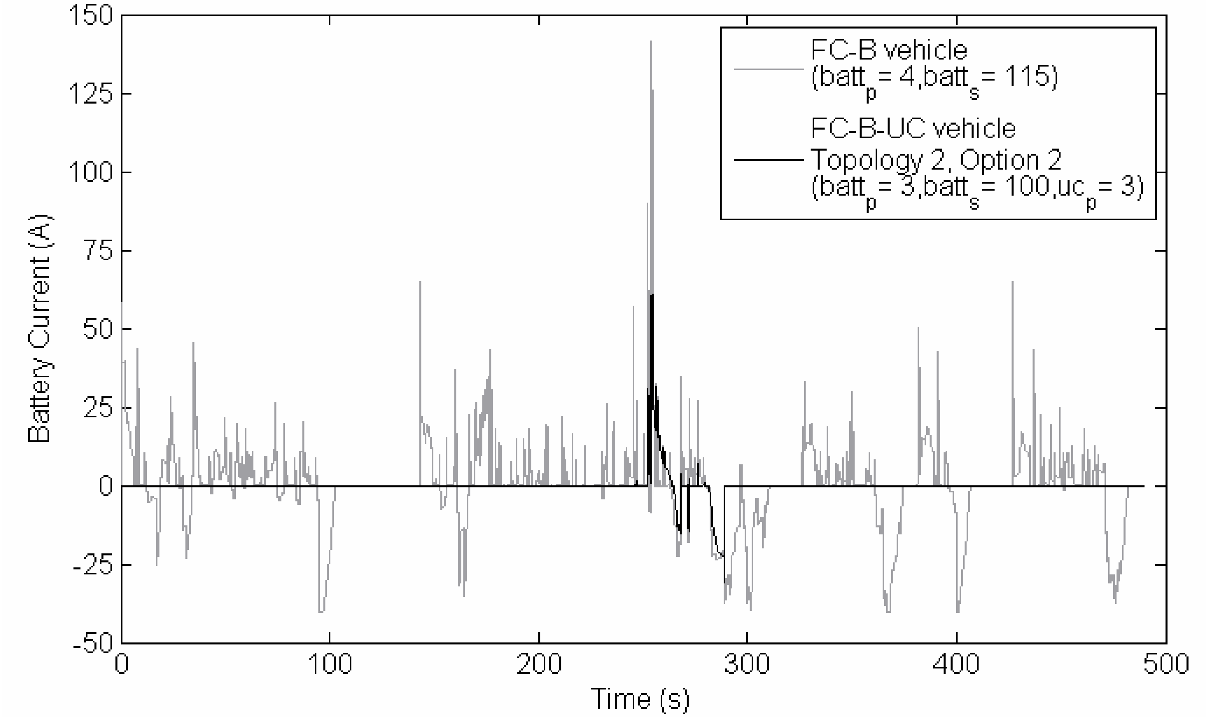

Figure 4-14: Comparison of battery currents in FC-B and FC-B-UC vehicles

Furthermore, recent developments in ultracapacitor technology strengthen the case for combining batteries and ultracapacitors in an ESS. For example, Maxwell Technologies has introduced a new line of large cell ultracapacitors which can handle over 1 million charge/discharge cycles and also have lower cost than the cells used in this study [19]. The 350-F BCAP0350 cell used in this study has a high-volume cost of \$0.02/Farad (\$7/cell), but the new cells (i.e., 3000-F BCAP3000) have a high-volume cost of \$0.015/Farad (based on correspondence with Maxwell Technologies). Though it is anticipated that both lithium-ion batteries and ultracapacitors will achieve technical improvements and reduced costs in the future, it is relevant to note that some advances with regards to new large ultracapacitor cells are here today.

4.5 Summary

This chapter has provided an in-depth and detailed comparison of near-optimal fuel cell-battery, fuel cell-ultracapacitor, and fuel cell-battery-ultracapacitor vehicles. A large-scale parametric study was conducted to determine the optimal component sizing and controllers for the chosen vehicle topologies. Power electronic converter details were included in the models to increase the accuracy of the results. Acceleration time, fuel economy, and cost were included in the objective function. Estimated battery durability was also used to approximate lifetime costs. The simulation results lead to the following conclusions:

(1) Due to the present and predicted future high relative cost of fuel cells compared to batteries and ultracapacitors, the optimal fuel cell size is approximately the minimum power required for cruising at high speeds and powering the auxiliary vehicle systems. For the SUV used in this study, the ideal fuel cell size was 40kW.

(2) A fuel cell-ultracapacitor vehicle is the least-desirable vehicle choice due to the relatively high powertrain cost and low fuel economy resulting from the high vehicle mass. This result is due to the low energy density of ultracapacitors compared to recent advancements in specific power, efficiency, and cost of lithium-ion batteries.

(3) The novel FC-B-UC diode-based topology presented in Chapter 2 is an overall improvement over the best FC-B-UC topology found in the literature, which uses a high-power DC/DC converter to connect the battery to the high-voltage bus. The novel topology yields higher fuel economy and has a lower cost than the topology from the literature when the acceleration time is kept constant. The only disadvantage of the novel topology, Option 1, is that a smaller ultracapacitor may not be able to store all of the regenerative braking energy for a certain drive cycle. However, this problem is remedied by the use of Option 2, which uses a switch to allow

battery charging from regenerative braking at certain times so that the ultracapacitor generally has room to store all remaining regenerative braking energy.

(4) The fuel cell-battery and fuel cell-battery-ultracapacitor vehicles are close competitors. The optimized fuel cell-battery vehicle is generally less costly initially and can offer better acceleration (for a given ESS cost range), yet the optimized fuel cell-battery-ultracapacitor vehicle (using novel Topology 2) has slightly higher fuel economy and most importantly can extend the battery lifetime due to less battery stress. Based on an analysis of the battery currents in both vehicle types, it is probable that the battery life extension will translate into fewer required replacements of the battery over the vehicle lifetime, and thus the lifetime cost of the FC-B-UC vehicle using novel Topology 2 is estimated to be less than the lifetime cost of the FC-B vehicle.

Chapter 5

Analytical Optimization Method for Novel Powertrain Topology

5.1 Introduction to Optimization Method

The novel fuel cell vehicle powertrain topology for a battery-ultracapacitor ESS presented in Chapter 2 and simulated in Chapter 4 is unique in that no power management mechanism is employed to control the power flow from the battery or the ultracapacitor independently. However, as discussed in Chapters 2 and 4, the topology can adequately fulfill the ideal requirements of the ESS: the ultracapacitor provides power more often, and the battery provides power when the ultracapacitor is depleted. Thus, the diode between the battery and ultracapacitor provides appropriate control during normal driving conditions. Since the time when the diode begins conducting depends on the battery voltage, the ultracapacitor voltage, and the ultracapacitor capacitance, the control is essentially embedded in the design of the ESS system. This means that an optimal design can ensure the optimal behaviour of the system, since no real-time control is available beyond the overall ESS current request. This chapter presents an analytical model of the general battery-diode-ultracapacitor system which allows for optimization of the battery and ultracapacitor sizes, given the parameters of a system. The optimization results can be used directly in a design, or as an analytically-derived starting point for further design refinement. Thus, this optimization method is not restricted to the ESS for fuel cell vehicles, but can be applied to any system using the battery-diode-ultracapacitor circuit.

The optimization of the ESS includes maximizing the efficiency, minimizing the mass, and minimizing the cost. Therefore, the objective function to be maximized is:

$$Obj = (x \cdot a \cdot Eff - b \cdot Cost - y \cdot c \cdot Mass) \tag{5-1}$$

$$a + b + c = 1 \tag{5-2}$$

where *a*, *b*, and *c* represent weightings that can be assigned based on the importance of maximizing the efficiency or minimizing the mass and cost, and *x* and *y* are parameters used to scale the different quantities being compared. These weightings and parameters are discussed in detail in Section 5.7. The efficiency term, *Eff*, is a combination of the calculated efficiency in an acceleration phase and a regenerative braking phase. The maximization of the objective function is subject to numerous constraints that are derived in Section 5.6. The objective function can be maximized according to the given constraints by using a non-linear program (NLP) solver, such as Maple's *NLPSolve*.

The first step is to obtain the power profile of the ESS. A vehicle simulator can be used to obtain the overall power required at the motor for a specific vehicle and drive cycle. Some mechanism (for example, an adaptive low-pass filter as used in Chapter 4) is used in the main vehicle controller to separate the power required at the load (the motor) into the fuel cell component and the ESS component. The ESS component will generally include the higher-frequency power requests and the peak power requests. In general, any method can be used to obtain the ESS power flow component. Figure 5-1 shows the proposed novel topology (Option 1) with the fuel cell and ESS power flow components, and Equation (5-3) shows the relationship between the power flow components. With the ESS power flow component isolated, the optimization method can focus on the ESS only, as shown in Figure 5-2 for Option 1. Figure 5-3 shows the ESS electrical circuits for Option 1 (diode-only) and Option 2 (diode + switch), including the parasitic resistances in the battery and ultracapacitor, *Rb* and *Rc*, which form the basis of the optimization method. The derivation of the efficiency during the acceleration phase is the same for both Option 1 and 2. For the regenerative braking phase, two separate efficiency equations are derived, one for Option 1 and the other for Option 2.

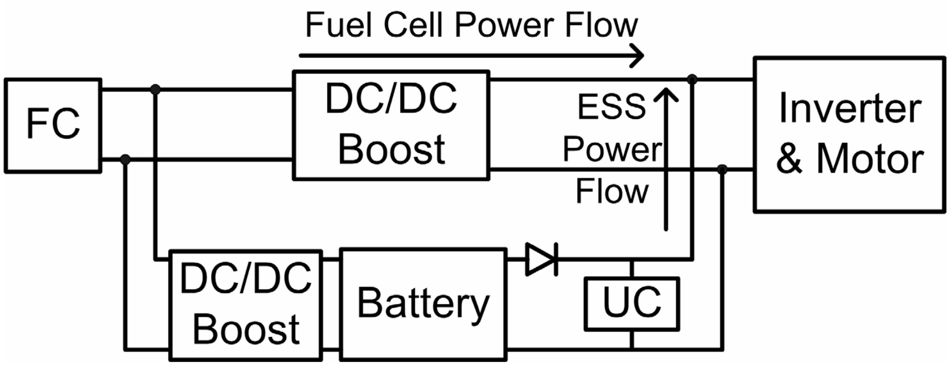

Figure 5-1: Novel topology with fuel cell and ESS power flow components

$$P_{fuelcell} + P_{ESS} = P_{motor} \quad \textbf{(5-3)}$$

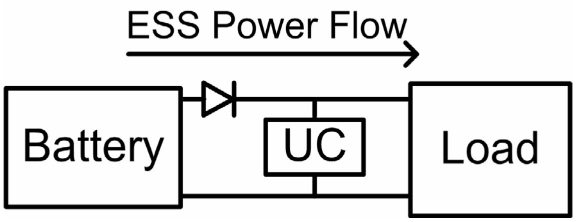

Figure 5-2: Battery-diode-ultracapacitor ESS – the focus of the optimization method

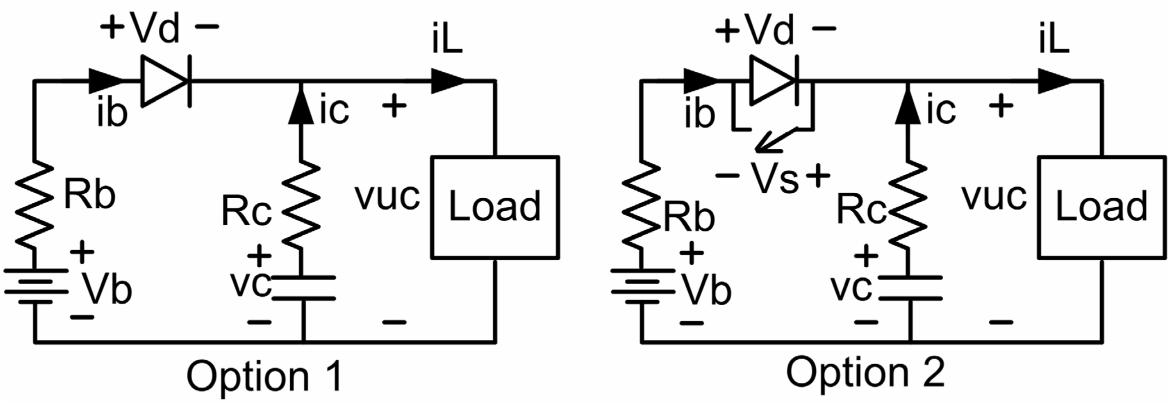

Figure 5-3: Electrical circuit of the ESS for Option 1 and Option 2

The internal battery voltage, *Vb*, is assumed to be constant, because over the relatively short period of acceleration or regenerative braking that is analyzed in the optimization method, the charge of each battery cell will not vary significantly, since the battery has a relatively large amount of energy storage. The voltage across the battery terminals will, however, vary due to the voltage drop across the internal resistance of the battery, *Rb*, when current, *ib*, is flowing into or out of the battery. Due to the much smaller energy content of the ultracapacitor, the internal ultracapacitor voltage, *vc*, will vary based on its charge, and the ultracapacitor terminal voltage, *vuc*, will also vary due to current, *ic*, flowing into or out of the ultracapacitor. Figure 5-3 is used to derive the following equations:

$$ib + ic = iL \quad \textbf{(5-4)}$$

$$vuc \cdot iL = P_{load} \quad \textbf{(5-5)}$$

5.2 Variables and Component Equations

In order to make the optimization method as general as possible, the system and component parameters can be defined to identify the specific case to be optimized. In general, the battery and ultracapacitor banks are comprised of numerous cells connected in series and in parallel. Thus, the component variables are defined on a per-cell basis. Table 5-1 shows the system variables and Table 5-2 shows the component variables.

Table 5-1: System Variables

Variable Symbol	Variable Name (units)	Variable Description
Vup	Upper load voltage (V)	The maximum voltage allowable at the motor inverter, depends on specific motor inverter used
$Vlow$	Lower load voltage (V)	The minimum voltage allowable at the motor inverter, depends on specific motor inverter used
P	Maximum positive power (W)	From the ESS power flow profile, the magnitude of the largest positive power peak during an acceleration
E	Maximum positive energy (J)	From the ESS power flow profile, the magnitude of the largest positive energy output (before the power goes negative for regenerative braking)
Pr	Maximum negative power (W)	From the ESS power flow profile, the magnitude of the largest negative power peak during regenerative braking
Er	Maximum negative energy (J)	From the ESS power flow profile, the magnitude of the largest negative energy input (before the power goes positive for acceleration)
a	Efficiency weighting term	Chosen by the designer to reflect the importance of maximizing efficiency (value from 0 to 1)
b	Cost weighting term	Chosen by the designer to reflect the importance of minimizing cost (value from 0 to 1)
c	Mass weighting term	Chosen by the designer to reflect the importance of minimizing mass ($c = 1-a-b$)

Table 5-2: Component Variables (to be defined based on component datasheets)

Component	Variable Symbol	Variable Name (units)
Battery	*Vcellb*	Nominal battery cell voltage (V)
	Rcellb	Battery cell internal resistance (Ω)
	ibcell	Maximum discharging battery current per cell (A)
	ibcellneg	Maximum charging battery current per cell (A)
	massbcell	Mass per battery cell (kg)
	costbcell	Cost per battery cell ($)
	columbiceff	Estimated columbic efficiency of battery (0 – 1)
Ultracapacitor	*Vcellc*	Voltage of cell when fully charged (V)
	Rcellc	Ultracapacitor cell internal resistance (Ω)
	iccell	Maximum current per ultracapacitor cell (A)
	Ccell	Capacitance per ultracapacitor cell (F)
	massccell	Mass per ultracapacitor cell (kg)
	costccell	Cost per ultracapacitor cell ($)
Diode	*Vd*	Forward voltage drop at rated current (kept constant to simplify model) (V)
	massdperA	Mass of diode per rated amp (kg/A)
	costdperA	Cost of diode per rated amp ($/A)
Switch	*Vs*	Collector-emitter saturation voltage of the switch at rated current (kept constant to simplify model) (V)
	massSperA	Mass of switch per rated amp (kg/A)
	costSperA	Cost of switch per rated amp ($/A)

The battery is defined by the number of cells connected in series, *Bs*, and the number of strings connected in parallel, *Bp*. The *Bs* variable determines the voltage of the battery, *Vb*, and thus plays an important role in deciding how the system will operate, since the battery will start conducting when the ultracapacitor voltage reaches (*Vb-Vd*). The *Bp* variable is important in determining the mass and cost of the system, but has little role to play in the operation, as long as the number of strings in parallel are sufficient to provide the maximum current required from the battery. For these reasons, *Bs* is chosen as an optimization variable, and *Bp* is defined by Equation (5-6).

$$Bp = ceil\left(\frac{P}{Vlow \cdot ibcell} \right) \tag{5-6}$$

Equation (5-6) shows a conservative value for *Bp* because the maximum positive power, *P*, will usually be provided by either the ultracapacitor, or by both the battery and the ultracapacitor. Hence, it is unlikely that the battery will be required to provide the full maximum power. For this reason, there is the option to use the *round* function to round down to the nearest integer, rather than the *ceil* function shown in Equation (5-6) which rounds up to the nearest integer.

The battery optimization variable, *Bs*, is used in two equations to describe the battery:

$$Vb = Vcellb \cdot Bs \tag{5-7}$$

$$Rb = \frac{Rcellb \cdot Bs}{Bp} \tag{5-8}$$

The ultracapacitor is also defined by the number of cells connected in series, *Cs*, and the number of strings connected in parallel, *Cp*. However, in this case, the number of cells in series, *Cs*, is fixed based on the maximum voltage of the system:

$$Cs = ceil\left(\frac{Vup}{Vcellc} \right) \tag{5-9}$$

The ultracapacitor optimization variable is *Cp*, since the number of strings in parallel determines the capacitance of the ultracapacitor bank, and hence how much energy is available from the ultracapacitor before the battery begins to provide power. Equations (5-10) and (5-11) define the overall internal resistance of the ultracapacitor bank, *Rc*, and the overall capacitance, *C*.

$$Rc = \frac{Rcellc \cdot Cs}{Cp} \tag{5-10}$$

$$C = \frac{Ccell \cdot Cp}{Cs} \tag{5-11}$$

The overall mass and cost of the system can also be described in terms of the optimization variables *Cp* and *Bs*, as shown in Equations (5-12) and (5-13) for Option 1. The mass and cost of the diode are the products of the maximum possible current through the diode (*ibcell·Bp*) and the mass and cost of the diode on a per-amp basis. Equations (5-14) and (5-15) show the mass and cost relations for Option 2, which include the mass and cost of the switch. The mass and cost of the switch are the products of the maximum possible current through the switch (*ibcellneg·Bp*) and the mass and cost of the switch on a per-amp basis.

$$Mass = Cp \cdot Cs \cdot massccell + Bp \cdot Bs \cdot massbcell + massdperA \cdot ibcell \cdot Bp \tag{5-12}$$

$$Cost = Cp \cdot Cs \cdot costccell + Bp \cdot Bs \cdot costbcell + costdperA \cdot ibcell \cdot Bp \tag{5-13}$$

$$\begin{aligned} Mass = {} & Cp \cdot Cs \cdot massccell + Bp \cdot Bs \cdot massbcell + massdperA \cdot ibcell \\ & \cdot Bp + massSperA \cdot ibcellneg \cdot Bp \end{aligned} \tag{5-14}$$

$$\begin{aligned} Cost = {} & Cp \cdot Cs \cdot costccell + Bp \cdot Bs \cdot costbcell + costdperA \cdot ibcell \cdot Bp \\ & + costSperA \cdot ibcellneg \cdot Bp \end{aligned} \tag{5-15}$$

5.3 Derivation of Efficiency During Acceleration Phase

In order to derive an analytical expression for efficiency in terms of the optimization variables *Bs* and *Cp*, the circuit in Figure 5-3 must be examined and the load must be defined. The desired expression for efficiency will only be in terms of variables *Bs* and *Cp*, and thus cannot be a function of time. Therefore, the load must be modeled as a constant source, such as constant voltage, constant power, or constant current. Since the voltage of the ultracapacitor, which is connected to the high-voltage bus, changes as current enters and leaves the ultracapacitor, it is not possible to use a constant voltage source. In regards to using a constant power source, there are two major problems: (i) it is not possible to obtain a closed-form solution for the ultracapacitor voltage, *vc(t)*, that is of a practical size to use in the rest of the efficiency derivation, and (ii) as shown in the example power profile in Figure 5-4, the ESS power varies greatly over a drive cycle and thus using a constant power load could give misleading results in terms of the expected efficiency over a drive cycle with maximum power output *P*. On the other hand, the use of a constant current load allows a tractable solution of the differential equation for *vc(t)*. Also, using a constant current load in the model implicitly and elegantly accounts for the fact that though the ESS must be capable of providing maximum power *P*, it is nearly always operating at a power less than *P* over the drive cycle. In the model, this corresponds to the power output declining from *P* as the bus (ultracapacitor) voltage declines, which more accurately matches the actual power profile of the load. Finally, a constant current load occurs in a real vehicle during the first portion of vehicle acceleration, as it is common to request constant torque from the motor, which corresponds to a constant current request. Therefore, for the reasons presented above, this analytical method to derive efficiency in terms of total energy output, *E*, uses a constant current load for the ESS. It is verified in Section 5.8 that this assumption does in fact lead to general conclusions on the effect of the sizing of *Bs* and *Cp* that agree with the theoretical expectations for an ESS operating in a vehicle with a variable power and variable current load. Thus, the optimization results are shown to be applicable to a general drive cycle with maximum power output *P*, with variable ESS power and current.

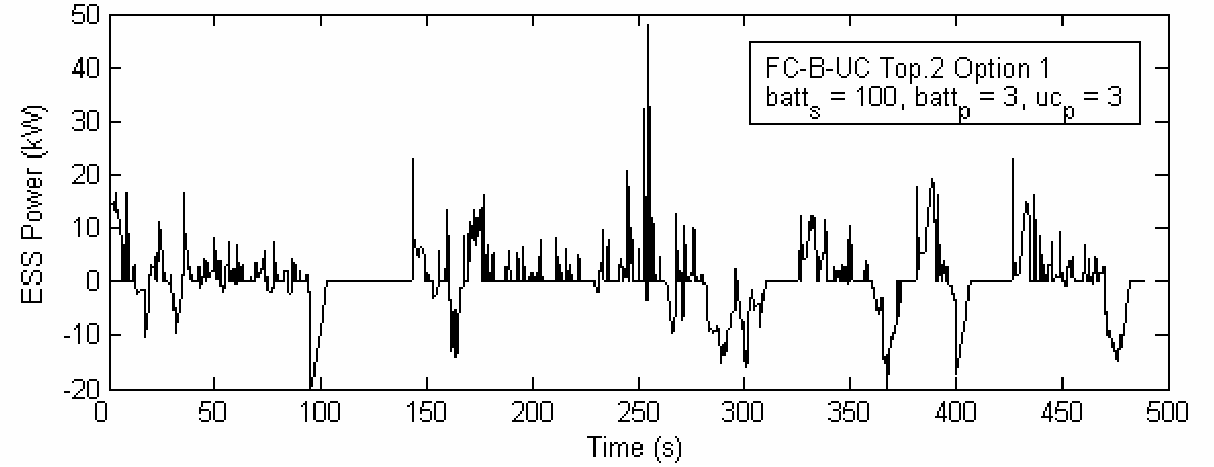

Figure 5-4: ESS power profile example

To find the constant load current *IL*, for the acceleration phase, it is assumed that the ultracapacitor is initially charged to *Vup*. Only the ultracapacitor-load loop in Figure 5-3 is considered, since the battery does not provide power initially. Writing a KVL equation around this loop for the initial condition *vc* = *Vup* and solving for *IL* yields:

$$vuc = Vup - IL \cdot Rc \tag{5-16}$$

$$vuc = \frac{P}{IL} \tag{5-17}$$

$$\frac{P}{IL} = Vup - IL \cdot Rc \tag{5-18}$$

$$IL = \frac{Vup - \sqrt{Vup^2 - 4 \cdot Rc \cdot P}}{2 \cdot Rc} \tag{5-19}$$

(It has been verified numerically that the desired value of *IL* is obtained when the square root quantity is subtracted from *Vup*.)

The acceleration phase is divided into two phases so that analytical expressions can be obtained based on which components are providing power:

Phase 1: from time *0* to *t1*, only the ultracapacitor is providing *IL*

Phase 2: from time *t1* to *t2*, both the battery and the ultracapacitor are providing *IL*

The transition from Phase 1 to Phase 2 occurs when the ultracapacitor internal voltage, *vc*, reaches the transition voltage *vct1*, and the diode begins conducting (i.e., the battery begins providing power):

$$vct1 = Vb - Vd + IL \cdot Rc \tag{5-20}$$

In order to determine how much energy is transferred to the load in Phase 1, it is required to find the time *t1*, when the battery begins providing power. Within Phase 1, the following equations hold:

$$ic = IL \tag{5-21}$$

$$C \cdot \frac{d}{dt} vc(t) = -IL \tag{5-22}$$

Solving the differential equation in (5-22) for *vc(t)* gives:

$$vc(t) = -\frac{IL \cdot t}{C} + C1 \tag{5-23}$$

The constant *C1* can be found by noting that at $t = 0$, $vc = Vup$; hence

$$C1 = Vup \tag{5-24}$$

Substituting Equation (5-24) in Equation (5-23) and solving for *t* yields the general expression relating time and ultracapacitor voltage, *vc*, in Phase 1, as shown in Equation (5-25).

$$t = \frac{(-vc(t) + Vup) \cdot C}{IL} \tag{5-25}$$

In order to find time *t1*, the internal ultracapacitor voltage, *vc*, must be replaced by the transition voltage *vct1* as shown in Equation (5-26).

$$t1 = \frac{(-vct1 + Vup) \cdot C}{IL} \tag{5-26}$$

In order to obtain the final expression for *t1*, Equations (5-19) and (5-20) can be substituted into Equation (5-26), as shown in Equation (5-27).

$$t1 = \frac{2\left(-Vb + Vd + \frac{1}{2}Vup + \frac{1}{2}\sqrt{Vup^2 - 4\cdot Rc\cdot P} \right)\cdot C\cdot Rc}{Vup - \sqrt{Vup^2 - 4\cdot Rc\cdot P}} \tag{5-27}$$

It is now possible to find the energy transferred to the load in Phase 1, *E1*, by substituting Equations (5-19), (5-25) (re-arranged such that *vc* is a function of *t*), and (5-27) into the expression for *E1*, given by Equation (5-28), and simplifying to reach Equation (5-29).

$$E1 = \int_0^{t1} IL\cdot(vc(t) - IL\cdot Rc)\,\mathrm{d}t \tag{5-28}$$

$$\begin{aligned} E1 = &-\frac{1}{2}\,C\,Vb^2 + C\,Vb\,Vd - \frac{1}{2}\,C\,Vd^2 + \frac{1}{4}\,C\,Vup^2 \\ &+ \frac{1}{4}\,C\,Vup\,\sqrt{Vup^2 - 4\,Rc\,P} - \frac{1}{2}\,C\,Rc\,P \end{aligned} \tag{5-29}$$

Equations (5-27) and (5-29) are used in Phase 2 to calculate the overall acceleration efficiency in terms of the optimization variables, *Cp* and *Bs*. The full circuit in Figure 5-3 (Option 1) is considered when deriving the equations for Phase 2, since both the battery and ultracapacitor are providing power to the load:

KVL:

$$Vb - ib(t)\cdot Rb - Vd = vc(t) - ic(t)\cdot Rc \tag{5-30}$$

KCL:

$$ib(t) = IL - ic(t) \tag{5-31}$$

$$ic(t) = -C\cdot\frac{\mathrm{d}}{\mathrm{d}\,t}vc(t) \tag{5-32}$$

Substituting Equations (5-31) and (5-32) into Equation (5-30) gives the following differential equation:

$$Vb - \left(IL + C\cdot\frac{d}{dt}vc(t)\right)\cdot Rb - Vd = vc(t) + C\cdot\frac{d}{dt}vc(t)\cdot Rc \tag{5-33}$$

The solution to Equation (5-33) is given by Equation (5-34).

$$vc(t) = Vb - Vd - Rb\cdot IL + \left(e^{-\frac{t}{C\cdot(Rb+Rc)}}\right)\cdot C2 \tag{5-34}$$

In order to solve for the integration constant *C2*, it can be noted that at *t = t1*, *vc(t) = vct1* (Equation 5-20). Also, to simplify the equations, a time-shift is performed so that for the Phase 2 equations, *t1* = 0, meaning that *t2* is the amount of time spent in Phase 2 (i.e., *t2* is the amount of time that both the battery and ultracapacitor are providing power). The resulting relation is shown as Equation (5-35).

$$C2 = IL\cdot(Rc + Rb) \tag{5-35}$$

Thus, the general expression relating internal ultracapacitor voltage with time in Phase 2 (where time has been shifted such that *t1* = 0) is:

$$vc(t) = Vb - Vd - Rb\cdot IL + IL\cdot(Rc + Rb)\cdot e^{-\frac{t}{C\cdot(Rb+Rc)}} \tag{5-36}$$

It is useful to differentiate Equation (5-36) with respect to time in order to define expressions for *ic(t)* and *ib(t)* using Equations (5-32) and (5-31) as follows:

$$\frac{d}{dt}vc(t) = -\frac{e^{-\frac{t}{C\cdot(Rb+Rc)}}\cdot IL}{C} \tag{5-37}$$

$$ic(t) = e^{-\frac{t}{C\cdot(Rb+Rc)}}\cdot IL \tag{5-38}$$

$$ib(t) = IL\cdot\left(1 - e^{-\frac{t}{C\cdot(Rb+Rc)}}\right) \tag{5-39}$$

The goal is to find the overall efficiency of the acceleration phase, which is defined as:

$$Effaccel = \frac{E}{Esupplied} \tag{5-40}$$

where *E* is the required energy output of the ESS (system variable from Table 5-1) and *Esupplied* is the total energy output from the battery and ultracapacitor over both Phase 1 and Phase 2, given in Equation (5-41). The difference between *E* and *Esupplied* is due to losses in the diode, the battery internal resistance, and the ultracapacitor internal resistance.

$$Esupplied = Ecap + Ebatt \tag{5-41}$$

The capacitor-energy equation (Equation (5-42)) is used to find the amount of energy provided by the ultracapacitor by time *t2*, which is the time when energy *E* has been absorbed by the load. Equation (5-36) is used in Equation (5-43) with *t* = *t2* to give the total change in ultracapacitor energy over both phases, *Ecap*. The total energy change of the battery is simply the time-integral of the battery output power, as given by Equation (5-44). Using Equation (5-39) to represent *ib* in terms of *t* in Equation (5-44), results in Equation (5-45).

$$\Delta Energy = \frac{1}{2}\cdot C\cdot\left(V_2^2 - V_1^2\right) \tag{5-42}$$

$$Ecap = \frac{1}{2}\cdot C\cdot\left(Vup^2 - \left(Vb - Vd - Rb\cdot IL + IL(Rc + Rb)\cdot e^{-\frac{t2}{C\,(Rb+Rc)}}\right)^2\right) \tag{5-43}$$

$$Ebatt = \int_0^{t2} ib(t)\cdot Vb\,\mathrm{d}t \tag{5-44}$$

$$Ebatt = Vb\ IL\ C\ (Rb + Rc)\cdot\left(e^{-\frac{t2}{C\,(Rb+Rc)}} - 1\right) + Vb\ IL\ t2 \tag{5-45}$$

It is necessary to find an expression for *t2* in terms of *Cp* and *Bs* so that the expression for efficiency (Equation (5-40)) is only in terms of optimization variables *Cp* and *Bs*. Therefore, it is necessary to find *E2*, the amount of energy absorbed by the load in Phase 2, in order to find *t2*, the amount of time spent in Phase 2. The amount of energy absorbed by the load in Phase 1, *E1* (Equation (5-29)), can be used to obtain an expression for *E2* as follows:

$$E2 = E - E1 \tag{5-46}$$

Also, it is useful to define *PL(t)* as the power absorbed by the load during Phase 2 so that it can be used to find another expression for *E2*, as shown in Equations (5-47) to (5-49). Note that Equations (5-34) and (5-38) have been used to expand (5-48) and obtain (5-49).

$$PL(t) = IL \cdot (vc(t) - ic(t) \cdot Rc) \tag{5-47}$$

$$E2 = \int_0^{t2} PL(t)\, \mathrm{d}t \tag{5-48}$$

$$E2 = C \cdot IL^2 \cdot Rb\left(Rb + Rc\right) + IL \cdot t2 \cdot (Vb - Vd) - IL^2 \cdot Rb \cdot t2 - IL^2 \cdot Rb \cdot C \cdot \mathrm{e}^{-\frac{t2}{C\,(Rb + Rc)}} \cdot (Rc + Rb) \tag{5-49}$$

Equations (5-46) and (5-49) can be used to get an expression in terms of *t2*, *Cp*, and *Bs*. Thus, it is possible to solve for *t2* in terms of *Cp* and *Bs* to get Equation (5-50).

$$
\begin{aligned}
t2 = -\Bigg(& -\mathrm{LambertW}\Bigg(\bigg(C\,IL^{2}\,Rb\,(Rb + Rc) \\
& \cdot \mathrm{e}^{-\frac{1}{IL\,(Vb - Vd - Rb\,IL)\,C\,(Rb + Rc)}\left(E + \frac{1}{2}\,C\,Vb^{2} - C\,Vb\,Vd + \frac{1}{2}\,C\,Vd^{2} - \frac{1}{4}\,C\,Vup^{2} - \frac{1}{4}\,C\,Vup\,\sqrt{Vup^{2} - 4\,Rc\,P} + \frac{1}{2}\,C\,Rc\,P - C\,Rb^{2}\,IL^{2} - IL^{2}\,Rc\,C\,Rb\right)}\bigg) \Big/ \big(IL\,(Vb - Vd - Rb\,IL)\,C\,Rb \\
& + IL\,(Vb - Vd - Rb\,IL)\,C\,Rc\big)\Bigg) - \bigg(E + \frac{1}{2}\,C\,Vb^{2} \\
& - C\,Vb\,Vd + \frac{1}{2}\,C\,Vd^{2} - \frac{1}{4}\,C\,Vup^{2} \\
& - \frac{1}{4}\,C\,Vup\,\sqrt{Vup^{2} - 4\,Rc\,P} + \frac{1}{2}\,C\,Rc\,P - C\,Rb^{2}\,IL^{2} \\
& - IL^{2}\,Rc\,C\,Rb\bigg) \Big/ \big(IL\,(Vb - Vd - Rb\,IL)\,C\,(Rb + Rc)\big)\Bigg) \\
& C\,(Rb + Rc)
\end{aligned}
\tag{5-50}
$$

The *Lambert* function satisfies the relation given in Equation (5-51).

$$
\mathrm{LambertW}(x) \cdot \mathrm{e}^{\mathrm{LambertW}(x)} = x
\tag{5-51}
$$

Substituting Equation (5-50) into Equations (5-43) and (5-45) gives expressions for *Ecap* and *Ebatt* in terms of *Cp* and *Bs*, and thus Equation (5-40) can be used to find overall acceleration efficiency, *Effaccel*, in terms of the system and component constants and the optimization variables *Cp* and *Bs*.

5.4 Derivation of Efficiency During Regenerative Braking Phase – Option 1

Since only the ultracapacitor can accept regenerative braking energy for the novel topology Option 1, this analysis will focus on the ultracapacitor-load loop in Figure 5-3. Two things will affect the efficiency of the regenerative braking phase: losses in *Rc* and the ultracapacitor being fully charged before regenerative braking is completed (this has the potential to have a large effect if the ultracapacitor is too small). Thus, constraints will be derived to ensure the ultracapacitor is large enough so that it is not fully charged to *Vup* before the regenerative load has input energy *Er* into the system.

The first step in modeling the regenerative braking phase is to determine the starting point of the ultracapacitor voltage, which is found using the following reasoning: after an acceleration in which the battery has provided some positive power (and thus the ultracapacitor terminal voltage has dropped to at least the battery internal voltage minus the diode forward voltage), it can be assumed that there will be a short period, of perhaps a few seconds in the case of a vehicle ESS, where the battery-ultracapacitor ESS provides little or no power before regenerative braking begins. During this time, if the ultracapacitor internal voltage, *vc*, has dropped below the battery voltage, *Vb*, (which is usually the case when considering the maximum power and energy requirements of the system) the battery will charge the ultracapacitor up to the battery voltage minus the diode forward conducting voltage (*Vb-Vd*). In the case where the battery was providing power for such a short time that the ultracapacitor internal voltage is still higher than the battery voltage (and thus the battery does not charge the ultracapacitor through the diode), it can be assumed that the ultracapacitor internal voltage will still end up very close to the battery voltage. For these reasons, a very accurate assumption for the ultracapacitor voltage at the beginning of the regenerative braking phase is determined to be *Vb*-*Vd*.

For the regenerative braking phase, the load is again modeled as a constant current source, with the current, *IR*, now entering the ultracapacitor (and battery for Option 2), as shown in Figure 5-5 for Option 1 and Option 2. Similar reasoning is used as in the acceleration phase derivation to justify the use of a constant current source. The current *IR* is calculated by assuming that the maximum power *Pr*, is achieved when the ultracapacitor internal voltage, *vc*, reaches its maximum voltage, *Vup*, as shown in Equations (5-52) an (5-53). Note that in Equation (5-53), the negative sign for the square root has been ruled out due to the fact that a negative value for *IR* is not acceptable.

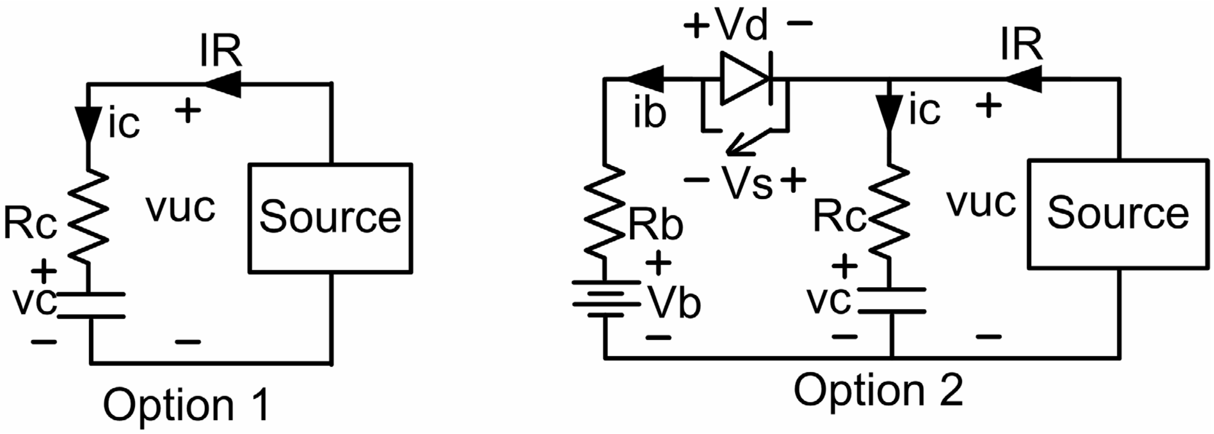

Figure 5-5: Electrical circuit for regenerative braking phase for Option 1 and Option 2

$$Vup + IR \cdot Rc = \frac{Pr}{IR} \tag{5-52}$$

$$IR = \frac{-Vup + \sqrt{Vup^2 + 4 \cdot Rc \cdot Pr}}{2 \cdot Rc} \tag{5-53}$$

It is important to note that in order for the ultracapacitor to get fully charged to *Vup*, the actual bus voltage (or ultracapacitor terminal voltage) will exceed *Vup* due to the voltage rise across the parasitic resistance in the ultracapacitor. In a real vehicle, the regenerative braking power would be decreased as the ultracapacitor approached the maximum bus voltage to ensure the bus voltage never exceeded *Vup* for safety reasons. The solution in this modeling scenario will be to disregard the bus limit of *Vup* for this transient spike, since the goal is to find the efficiency, and it is known that the proper safety limits would be in place in a real vehicle.

It should also be noted that in the acceleration Phase 1 calculation, *vc* ranged from *Vup* to *vct1*, and the energy output to the load from the ultracapacitor was calculated, *E1*. In the regenerative braking phase, it is again desired to fix the ultracapacitor starting and ending voltage, to *Vb*-*Vd* and *Vup* respectively, and hence it is not possible to fix the energy input from the load to the desired *Er*, since we have already set *IR* based on *Pr*. However, a constraint is derived in Section 5.6 to ensure the energy input from the load, *Ein*, is equal to the specified regenerative braking energy, *Er*.

The differential equation to describe the system in Figure 5-5 (Option 1) during regenerative braking is derived and solved as follows:

$$ic = IR \tag{5-54}$$

$$C \cdot \frac{d}{dt} vc(t) = IR \tag{5-55}$$

$$vc(t) = \frac{IR \cdot t}{C} + C3 \tag{5-56}$$

When $t = 0$, $vc = Vb\text{-}Vd$; therefore the constant $C3 = Vb\text{-}Vd$ and the general expression for $vc(t)$ is:

$$vc(t) = \frac{IR \cdot t}{C} + Vb - Vd \tag{5-57}$$

The end-point of the regenerative braking analysis is defined as the time when $vc(t) = Vup$, as shown in Equation (5-58). The end-time, $t1$, can then be solved for as shown in Equation (5-59).

$$Vup = \frac{IR \cdot t1}{C} + Vb - Vd \tag{5-58}$$

$$t1 = \frac{(Vup - Vb + Vd) \cdot C}{IR} \tag{5-59}$$

When IR is expanded, the expression for $t1$ is as shown in Equation (5-60).

$$t1 = \frac{2\,(Vup - Vb + Vd)\,C\,Rc}{-Vup + \sqrt{Vup^2 + 4\,Rc\,Pr}} \tag{5-60}$$

It is then possible to calculate the total energy sent into the system from the constant current load, Ein, by substituting Equation (5-57) into Equation (5-61), resulting in Equation (5-62).

$$Ein = \int_0^{t1} IR \cdot (vc(t) + IR \cdot Rc)\, dt \tag{5-61}$$

$$Ein = \frac{1}{2}\,C\,(Vup - Vb + Vd)^2 + \left(\frac{1}{2}\sqrt{Vup^2 + 4\,Rc\,Pr} + Vb - Vd - \frac{1}{2}\,Vup\right)(Vup - Vb + Vd)\,C \tag{5-62}$$

The energy that has actually been stored in the ultracapacitor, *Euc*, can be calculated using Equation (5-63).

$$Euc = \frac{1}{2}\cdot C\cdot\left(Vup^2 - (Vb - Vd)^2\right) \tag{5-63}$$

The efficiency of the regenerative braking phase for Option 1 can then be found by substituting Equations (5-62) and (5-63) into Equation (5-64). The simplified result for the efficiency of regenerative braking for Option 1 is shown as Equation (5-65). As desired, Equation (5-65) is a function of only the two optimization variables, *Cp* and *Bs*, since *Rc* is a function of *Cp* and *Vb* is a function of *Bs*.

$$Effbrake = \frac{Euc}{Ein} \tag{5-64}$$

$$Effbrake = \frac{Vup + Vb - Vd}{Vb - Vd + \sqrt{Vup^2 + 4\,Rc\,Pr}} \tag{5-65}$$

5.5 Derivation of Efficiency During Regenerative Braking Phase – Option 2

For Option 2, which uses the diode and the anti-parallel switch to connect the battery to the high-voltage bus, the regenerative braking phase is divided into two phases so that analytical expressions can be obtained based on which components are accepting power:

Phase 1: from time *0* to *t1*, both the battery and the ultracapacitor are accepting *IR*

Phase 2: from time *t1* to *t2*, only the ultracapacitor is accepting *IR*

The transition from Phase 1 to Phase 2 occurs when the battery switch opens due to the battery current reaching its upper charging limit.

The derivation of efficiency for Phase 1 of regenerative braking begins by writing the KVL and KCL equations of the Option 2 circuit shown in Figure 5-5.

KVL:

$$Vb + ib(t) \cdot Rb + Vs = vc(t) + ic(t) \cdot Rc \qquad \textbf{(5-66)}$$

KCL:

$$ib(t) + ic(t) = IR \qquad \textbf{(5-67)}$$

The first goal is to find *vc(t)* as a function of time for Phase 1. To do this, *ic(t)* and *ib(t)* can be written in terms of *vc(t)*, as shown in Equations (5-68) and (5-69), and substituted into Equation (5-66). After solving the differential equation, the resulting expression for *vc(t)* is given by Equation (5-70).

$$ic(t) = C \cdot \frac{d}{dt} vc(t) \qquad \textbf{(5-68)}$$

$$ib(t) = IR - C \cdot \frac{d}{dt} vc(t) \qquad \textbf{(5-69)}$$

$$vc(t) = Vb + Rb \cdot IR + Vs + e^{-\frac{t}{C\,(Rb + Rc)}} \cdot C4 \qquad \textbf{(5-70)}$$

The integration constant, *C4*, can be found from Equation (5-70) by noting that *vc(0) = Vb-Vd*. The resulting expression for *C4* is shown as Equation (5-71) and the final expression for *vc(t)* in Phase 1 is shown as Equation (5-72).

$$C4 = -Vd - Vs - Rb \cdot IR \qquad \textbf{(5-71)}$$

$$vc(t) = Vb + Rb \cdot IR + Vs + (-Vd - Vs - Rb \cdot IR) \cdot \mathrm{e}^{-\frac{t}{C\,(Rb + Rc)}} \tag{5-72}$$

Now, using Equations (5-69) and (5-72), it is possible to obtain the expression for *ib(t)*, as shown in Equation (5-73).

$$ib(t) = IR + \frac{(-Vd - Vs - Rb\ IR)\ \mathrm{e}^{-\frac{t}{C\,(Rb + Rc)}}}{Rb + Rc} \tag{5-73}$$

While the battery is accepting regenerative braking current in Phase 1, the battery current, *ib(t)*, is continually rising since the ultracapacitor voltage is rising and the battery internal voltage, *Vb*, is approximately constant. To avoid exceeding the charging battery current limit (*ibcellneg*), the switch must be opened when *ib(t) = ibcellneg* × *Bp*, where *Bp* is the number of battery strings in parallel. The opening of the switch marks the end of battery charging for this regenerative braking event and thus the end of Phase 1. Equation (5-73) is used to determine *t1*, the time at the end of Phase 1, as shown in Equations (5-74) and (5-75).

$$Bp \cdot ibcellneg = IR + \frac{(-Vd - Vs - Rb\ IR)\ \mathrm{e}^{-\frac{t1}{C\,(Rb + Rc)}}}{Rb + Rc} \tag{5-74}$$

$$t1 = -\ln\left(\frac{(-Bp\ ibcellneg + IR)\ (Rb + Rc)}{Vd + Vs + Rb\ IR}\right) C\,(Rb + Rc) \tag{5-75}$$

Now that *t1* and *vc(t)* in Phase 1 are known, it is possible to calculate the total regenerative braking energy sent into the ESS during Phase 1, *Ein1*, using Equation (5-76). The resulting expression for *Ein1* is given by Equation (5-77).

$$Ein1 = \int_0^{t1} IR \cdot (vc(t) + IR \cdot Rc)\ \mathrm{d}t \tag{5-76}$$

$$\begin{aligned}
\mathit{Ein1} = -C\,\mathit{IR}\,\Bigg(&-\mathit{Rb}\,\mathit{IR}\,\mathit{Rc} + \mathit{Vd}\,\mathit{Rc} + \mathit{Vd}\,\mathit{Rb} + \mathit{Vs}\,\mathit{Rc} + \mathit{Vs}\,\mathit{Rb} \\
&+ 2\,\mathit{Rb}\,\mathit{Rc}\,\mathit{Bp}\,\mathit{ibcellneg} \\
&+ \mathit{Vb}\ln\left(\frac{(-\mathit{Bp}\,\mathit{ibcellneg} + \mathit{IR})\,(\mathit{Rb} + \mathit{Rc})}{\mathit{Vd} + \mathit{Vs} + \mathit{Rb}\,\mathit{IR}}\right)\mathit{Rb} \\
&+ \mathit{Vb}\ln\left(\frac{(-\mathit{Bp}\,\mathit{ibcellneg} + \mathit{IR})\,(\mathit{Rb} + \mathit{Rc})}{\mathit{Vd} + \mathit{Vs} + \mathit{Rb}\,\mathit{IR}}\right)\mathit{Rc} \\
&+ \mathit{Vs}\ln\left(\frac{(-\mathit{Bp}\,\mathit{ibcellneg} + \mathit{IR})\,(\mathit{Rb} + \mathit{Rc})}{\mathit{Vd} + \mathit{Vs} + \mathit{Rb}\,\mathit{IR}}\right)\mathit{Rb} \\
&+ \mathit{Rb}^2\,\mathit{IR}\ln\left(\frac{(-\mathit{Bp}\,\mathit{ibcellneg} + \mathit{IR})\,(\mathit{Rb} + \mathit{Rc})}{\mathit{Vd} + \mathit{Vs} + \mathit{Rb}\,\mathit{IR}}\right) \\
&+ 2\,\mathit{Rb}\,\mathit{IR}\ln\left(\frac{(-\mathit{Bp}\,\mathit{ibcellneg} + \mathit{IR})\,(\mathit{Rb} + \mathit{Rc})}{\mathit{Vd} + \mathit{Vs} + \mathit{Rb}\,\mathit{IR}}\right)\mathit{Rc} - \mathit{Rc}^2\,\mathit{IR} \\
&+ \mathit{Vs}\ln\left(\frac{(-\mathit{Bp}\,\mathit{ibcellneg} + \mathit{IR})\,(\mathit{Rb} + \mathit{Rc})}{\mathit{Vd} + \mathit{Vs} + \mathit{Rb}\,\mathit{IR}}\right)\mathit{Rc} \\
&+ \mathit{Rb}^2\,\mathit{Bp}\,\mathit{ibcellneg} \\
&+ \mathit{IR}\,\mathit{Rc}^2\ln\left(\frac{(-\mathit{Bp}\,\mathit{ibcellneg} + \mathit{IR})\,(\mathit{Rb} + \mathit{Rc})}{\mathit{Vd} + \mathit{Vs} + \mathit{Rb}\,\mathit{IR}}\right) \\
&+ \mathit{Rc}^2\,\mathit{Bp}\,\mathit{ibcellneg}\Bigg)
\end{aligned} \tag{5-77}$$

Equations (5-73) and (5-75) are used to find the amount of energy absorbed by the battery during Phase 1. The amount of energy is multiplied by the columbic efficiency, *columbiceff*, since the effect of the columbic losses is to reduce the amount of useful energy stored in the battery that is available for the next acceleration. Equation (5-78) shows the integral expression for the battery energy stored and Equation (5-79) shows the expanded expression.

$$\mathit{Ebatt} = \mathit{columbiceff} \cdot \int_0^{t1} \mathit{ib}(t) \cdot \mathit{Vb}\,\mathrm{d}t \tag{5-78}$$

$$Ebatt = -columbiceff\ Vb\ C\left(Vd + Vs + IR\ln\left(-\frac{(Bp\ ibcellneg - IR)\,(Rb + Rc)}{Vd + Vs + Rb\ IR}\right)Rb + IR\ln\left(-\frac{(Bp\ ibcellneg - IR)\,(Rb + Rc)}{Vd + Vs + Rb\ IR}\right)Rc + Bp\ ibcellneg\ Rb + Bp\ ibcellneg\ Rc - IR\ Rc\right) \quad \textbf{(5-79)}$$

The energy stored in the ultracapacitor over both phases is found using Equation (5-80), since the initial and final ultracapacitor voltages are fixed at *Vup* and *Vb-Vd*, respectively.

$$Ecap = \frac{1}{2}\cdot C\cdot\left(Vup^2 - (Vb - Vd)^2\right) \quad \textbf{(5-80)}$$

The next step is to find *t2*, the length of Phase 2, which is needed to find the energy input to the ESS during Phase 2, *Ein2*. Note that a time shift is again performed such that *t1* = 0. The time *t2* is defined as the time when the ultracapacitor is charged to *Vup*, marking the end of Phase 2 and the regenerative braking event. Therefore, in order to find *t2*, *vc(t)* in Phase 2 must first be found, so that *vc(t2)* can be set equal to *Vup* to solve for *t2*. Since in Phase 2 only the ultracapacitor is accepting regenerative braking power, the equation for *vc(t)* is the same as for Option 1 (Equation (5-56)) except with a different integration constant, *C5*, as shown in Equation (5-81).

$$vc(t) = \frac{IR\cdot t}{C} + C5 \quad \textbf{(5-81)}$$

The constant *C5* is equal to *vc(t1)* since *t1* is shifted to be equal to 0 for the Phase 2 derivations. Equation (5-72), which gives the expression for *vc(t)* in Phase 1, is used to solve for *C5*. The complete expression for *vc(t)* in Phase 2, including the value of *C5*, is shown in Equation (5-82).

$$vc(t) = \frac{IR\cdot t}{C} + Vb + Vs + Bp\ ibcellneg\cdot(Rb + Rc) - IR\ Rc \quad \textbf{(5-82)}$$

Now, *t2* can be found by setting *vc(t) = Vup* and *t = t2* in Equation (5-82) and solving for *t2*, as shown in Equation (5-83).

$$t2 = -\frac{(-Vup + Vb + Vs + Bp\ ibcellneg\ (Rb + Rc) - IR\ Rc)\ C}{IR} \tag{5-83}$$

The expressions for *t2* and *vc(t)* in Phase 2 are used in Equation (5-84) to find *Ein2*, the energy into the ESS during Phase 2. The expanded expression for *Ein2* is shown in Equation (5-85).

$$Ein2 = \int_0^{t2} IR \cdot (vc(t) + IR \cdot Rc)\, \mathrm{d}t \tag{5-84}$$

$$\begin{aligned} Ein2 = &-Vb\ C\ Bp\ ibcellneg\ Rc - \frac{1}{2}\ C\ Vs^2 + \frac{1}{2}\ C\ Vup^2 \\ &- \frac{1}{2}\ C\ Vb^2\ \ - Vb\ C\ Vs - \frac{1}{2}\ C\ Bp^2\ ibcellneg^2\ Rc^2 \\ &+ C\ Vup\ IR\ Rc - \frac{1}{2}\ C\ Bp^2\ ibcellneg^2\ Rb^2 + \frac{1}{2}\ C\ Rc^2\ IR^2 \\ &- Vb\ C\ Bp\ ibcellneg\ Rb - C\ Vs\ Bp\ ibcellneg\ Rc \\ &- C\ Vs\ Bp\ ibcellneg\ Rb - C\ Bp^2\ ibcellneg^2\ Rb\ Rc \end{aligned} \tag{5-85}$$

Now, the overall efficiency of regenerative braking for Option 2, *Effbrake*, is calculated using Equation (5-86). *Ecap* (Equation (5-80)), *Ebatt* (Equation (5-79)), *Ein1* (Equation (5-77)), and *Ein2* (Equation (5-85)) have been found in terms of the system and component constants and the optimization variables, *Bs* and *Cp*, and thus, *Effbrake* is a function of only *Bs* and *Cp*.

$$Effbrake = \frac{Ecap + Ebatt}{Ein1 + Ein2} \tag{5-86}$$

5.6 Constraints

Five constraints are required to guarantee that the optimal values for *Bs* and *Cp* are within a range which ensures the desired operation of the system. The constraints are entered into the non-linear program solver when performing the optimization.

1) Calculation of minimum number of battery cells in series: *Bsmin*

This constraint is to ensure that at rated current, the battery terminal voltage will not drop below the minimum bus voltage, *Vlow*. Since *Bsmin* must be an integer, the *ceil* function is used to round up the value found for *Bsmin* to the next integer.

$$(Vcellb - Rcellb \cdot ibcell)Bsmin \geq Vlow \qquad \textbf{(5-87)}$$

$$Bsmin = \text{ceil}\left(\frac{Vlow}{Vcellb - Rcellb \cdot ibcell} \right) \qquad \textbf{(5-88)}$$

$$Constraint\ 1 : Bs \geq Bsmin \qquad \textbf{(5-89)}$$

2) Calculation of minimum number of ultracapacitor strings in parallel: *Cpmin*

This constraint is to ensure that there are enough strings of ultracapacitors in parallel to handle the highest expected ultracapacitor current, *IL* (so that the ultracapacitor maximum current limit, *iccell*, is never exceeded). It is helpful to define Equations (5-90) and (5-91) to obtain *Rc* as a function of *Cp*. The maximum ultracapacitor current is equal to *IL* and in Equation (5-92), *icmax* is set equal to the expression for *IL* from Equation (5-19). Since *icmax* = *iccell* × *Cp*, it is possible to solve for the minimum value of *Cp*, *Cpmin*, as shown in Equations (5-93) and (5-94). The *ceil* function is used to round the value found for *Cpmin* up to the nearest integer, which gives a safety factor in the case that the ultracapacitor is not fully charged to Vup when current *IL* is required.

$$Rc = \frac{\alpha}{Cp} \qquad \textbf{(5-90)}$$

$$\alpha = Rccell \cdot Cs \qquad \textbf{(5-91)}$$

$$icmax = \frac{Vup - \sqrt{Vup^2 - \frac{4 \cdot P \cdot \alpha}{Cp}}}{\frac{2 \cdot \alpha}{Cp}} \tag{5-92}$$

$$iccell \cdot Cpmin \geq \frac{Vup - \sqrt{Vup^2 - \frac{4 \cdot P \cdot \alpha}{Cpmin}}}{\frac{2 \cdot \alpha}{Cpmin}} \tag{5-93}$$

$$Cpmin = ceil\left(\frac{P}{iccell \cdot \left(Vup - iccell \cdot \alpha \right)} \right) \tag{5-94}$$

$$Constraint\ 2 : Cp \geq Cpmin \tag{5-95}$$

3) Calculation of maximum number of battery cells in series: *Bsmax* (based on *Cp*)

This constraint is to ensure that the battery does not provide power at the very beginning of the acceleration phase (since the goal is to have the ultracapacitor provide the power initially). This constraint must be adhered to in order to obtain meaningful optimization results since the equations have been derived under the assumption that only the ultracapacitor provides power initially in Phase 1. This constraint is set by ensuring that the internal voltage of the ultracapacitor at the end of Phase 1, *vct1*, is less than *Vup*, as shown in Equation (5-96) and (5-97). When *IL* is expanded and the battery voltage, *Vb*, is set to *Vcellb·Bsmax*, as shown in Equation (5-98), *Bsmax* can be solved for, as shown in Equation (5-99). Also, since *Bs* is an integer, the *floor* function is used in Equation (5-99) to round down to the nearest integer.

$$vct1 < Vup \tag{5-96}$$

$$Vb - Vd + IL \cdot Rc < Vup \tag{5-97}$$

$$Vcellb \cdot Bsmax - Vd + \frac{1}{2} Vup - \frac{1}{2}\sqrt{Vup^2 - \frac{4\,\alpha P}{Cp}} < Vup \tag{5-98}$$

$$Bsmax = \text{floor}\left(\frac{1}{2} \frac{2\,Vd + Vup + \sqrt{Vup^2 - \frac{4\,\alpha\,P}{Cp}}}{Vcellb} \right) \tag{5-99}$$

$$Constraint\ 3 : Bs \le Bsmax \tag{5-100}$$

4) Constraint to ensure battery provides power during acceleration phase

It is necessary to ensure the battery provides power at some point in the acceleration phase, otherwise, the equation for efficiency derived in Section 5.3 will not hold, since it assumes that the ultracapacitor voltage reaches the transition voltage, *vct1*, before the required acceleration energy, *E*, is supplied to the load. In a real vehicle, this means that at high power, it is expected that the battery provides power at some point, or there is no point in having the battery. If the battery does not provide power at all in the acceleration phase, it means that *Cp* is too large and/or *Bs* is too small, and thus the ultracapacitor voltage does not become low enough for the diode to conduct before energy *E* is provided to the load. Constraint 4 is used to prevent this from happening. Equation (5-29) gives an expression for the energy output to the load during Phase 1 of acceleration (when only the ultracapacitor is providing power), *E1*, in terms of *Cp* and *Bs*. In order to ensure that the system enters Phase 2 of the acceleration, where the battery can also provide power, it is necessary to set the total energy output to the load during the acceleration phase, *E*, to be greater than or equal to *E1*, as shown in Equation (5-101). It is useful to define the relations in Equations (5-102) and (5-103) to get capacitance, *C*, in terms of *Cp*.

$$E \ge E1 \tag{5-101}$$

$$\beta = \frac{Ccell}{Cs} \tag{5-102}$$

$$C = \beta \cdot Cp \tag{5-103}$$

When *E1* is expanded in terms of *Cp* and *Bs*, the final expression for Constraint 4 is obtained, as shown in Equation (5-104).

$$E \geq -\frac{1}{2}\,\beta\, Cp\, Vcellb^2\, Bs^2 + \beta\, Cp\, Vcellb\, Bs\, Vd - \frac{1}{2}\,\beta\, Cp\, Vd^2 + \frac{1}{4}\,\beta\, Cp\, Vup^2 + \frac{1}{4}\,\beta\, Cp\, Vup \sqrt{Vup^2 - \frac{4\,\alpha\, P}{Cp}} - \frac{1}{2}\,\beta\,\alpha\, P \tag{5-104}$$

5) Constraint to ensure ultracapacitor can absorb required regenerative braking energy, *Er*

This constraint has two versions: one for Option 1 (diode-only) and the other for Option 2 (diode and switch), since the energy storage equations are different for each option. For Option 1, Equation (5-62) calculates the total energy put into the system from the constant current load during the regenerative braking phase, *Ein*, as a function of *Cp* and *Bs*. This end of this phase is defined as the time when the ultracapacitor becomes charged to *Vup*. The relation in Equation (5-105) puts constraints on *Bs* and *Cp* in order to ensure the ultracapacitor becomes charged to *Vup* at precisely the time that energy *Er* has been put into the system. The constraint for Option 1 is shown in Equation (5-106) with *Ein* expanded as a function of *Cp* and *Bs*.

$$Er = Ein \tag{5-105}$$

$$Er = \frac{1}{2}\, C\, (Vup - Vb + Vd)^2 + \left(\frac{1}{2}\sqrt{Vup^2 + 4\, Rc\, Pr} + Vb - Vd - \frac{1}{2}\, Vup\right)(Vup - Vb + Vd)\, C \tag{5-106}$$

The constraint for Option 2 uses the same principle, but in this case, *Er* is set to be equal to the sum of the energy put into the system in Phase 1 (battery and ultracapacitor accepting power) and in Phase 2 (only ultracapacitor accepting power), *Ein1* + *Ein2*, given in Equations (5-77) and (5-85).

5.7 Objective Function

The objective function, repeated here as Equation (5-107), includes the overall efficiency, cost, and mass of the system. To account for the case when the energy transfer in the acceleration phase, *E*, is not equal to that in the regenerative braking phase, *Er*, the overall efficiency is obtained by taking a weighted average of *Effaccel* and *Effbrake* as shown in Equation (5-108).

$$Obj = (\, x \cdot a \cdot Eff - b \cdot Cost - y \cdot c \cdot Mass \,) \tag{5-107}$$

$$Eff = \frac{(E \cdot Effaccel + Er \cdot Effbrake\,)}{E + Er} \tag{5-108}$$

The numerical quantities being compared in the objective function (efficiency in percentage, cost in dollars, and mass in kilograms) are of very different magnitudes. Thus, a method is derived to add appropriate scaling, in the form of constants *x* and *y*, to the objective function. The goal is to ensure that the weighting coefficients, *a*, *b*, and *c*, have the desired effect, that is, to allow the designer to more heavily weigh a certain metric by adjusting the coefficients. The principle of the scaling method is to choose *x* and *y* such that the difference in cost, mass, and efficiency is approximately the same when *Bs* and *Cp* are varied from the minimum to maximum values. Thus, the first step is to calculate approximate maximum values for *Bs* and *Cp*, which is difficult to do precisely, because the upper bound on each optimization variable, *Bs* and *Cp*, depends dynamically on the value of the other optimization variable, based on Constraints 3 to 5.

From Constraint 3, it is possible to find an approximate constant value for *Bsmax*, *Bsmaxappro*x, by substituting *Cpmin* in for *Cp* in Equation (5-99), as shown in Equation (5-109). It is then possible to estimate an average value for *Bs*, *Bsavg*, as shown in Equation (5-110).

$$Bsmaxapprox = floor\left(\frac{1}{2} \frac{2\,Vd + Vup + \sqrt{Vup^2 - \dfrac{4\,\alpha\,P}{Cpmin}}}{Vcellb} \right) \tag{5-109}$$

$$Bsavg = \frac{1}{2}(Bsmin + Bsmaxapprox\,) \tag{5-110}$$

A clear result of having an ultracapacitor which is too large would be that the battery never provides current during the acceleration phase, which is prevented by ensuring Constraint 4 is met. Constraint 4 can be solved to provide an approximation of *Cpmax*, i.e., *Cpmaxapprox*, when *Bs* = *Bsavg*, as shown in Equation (5-111).

$$\begin{aligned} Cpmaxapprox = ceil\Big(\Big(& -2\,\beta\, Vcellb\; Bsavg\; Vd\,\alpha\, P + \beta\, Vd^{2}\,\alpha\, P \\ & + \beta\, Vcellb^{2}\, Bsavg^{2}\,\alpha\, P - Vup^{2}\, E + 2\, Vcellb^{2} \cdot Bsavg^{2} \cdot E \\ & - 4\, Vcellb\; Bsavg\; Vd\; E + 2\, Vd^{2}\, E \\ & + \big(Vup^{4}\, E^{2} - 4\,\beta\, Vcellb\; Bsavg\; Vd\,\alpha\, P\; Vup^{2}\, E + 2\,\beta\, Vd^{2}\,\alpha\, P\; V \\ & + Vd^{2}\, Vup^{2}\,\beta^{2}\,\alpha^{2}\, P^{2}\big)^{1/2}\Big) \Big/ \Big(\big(4\, Vcellb^{3}\, Bsavg^{3}\, Vd \\ & - 2\, Vcellb\; Bsavg\; Vd\; Vup^{2} + Vcellb^{2}\, Bsavg^{2}\, Vup^{2} \\ & + 4\, Vcellb\; Bsavg\; Vd^{3} + Vd^{2}\, Vup^{2} - 6\, Vcellb^{2}\, Bsavg^{2}\, Vd^{2} \\ & - Vd^{4} - Vcellb^{4}\, Bsavg^{4}\big)\,\beta\Big)\Big) \end{aligned} \qquad \textbf{(5-111)}$$

The actual minimum cost and mass, and approximations for the maximum cost and mass can then be found as shown in Equations (5-112) to (5-115).

$$\begin{aligned} mincost = {} & costccell \cdot Cs \cdot Cpmin + costbcell \cdot Bp \cdot Bsmin + costdperA \\ & \cdot ibcell \cdot Bp \end{aligned} \qquad \textbf{(5-112)}$$

$$\begin{aligned} maxcost = {} & costccell \cdot Cs \cdot Cpmaxapprox + costbcell \cdot Bp \cdot Bsmaxapprox \\ & + costdperA \cdot ibcell \cdot Bp \end{aligned} \qquad \textbf{(5-113)}$$

$$\begin{aligned} minmass = {} & massccell \cdot Cs \cdot Cpmin + massbcell \cdot Bp \cdot Bsmin \\ & + massdperA \cdot ibcell \cdot Bp \end{aligned} \qquad \textbf{(5-114)}$$

$$\begin{aligned} maxmass = {} & massccell \cdot Cs \cdot Cpmaxapprox + massbcell \cdot Bp \\ & \cdot Bsmaxapprox + massdperA \cdot ibcell \cdot Bp \end{aligned} \qquad \textbf{(5-115)}$$

The next step is to define the difference in efficiency, cost, and mass of the system that is expected as *Bs* and *Cp* are varied. The differences in cost, Δ*Cost*, and mass, Δ*Mass*, are easily defined based on Equations (5-112) to (5-115), as shown in Equations (5-116) and (5-117). However, before performing the optimization, it is difficult to determine the maximum and minimum efficiencies. In general, a higher *Cp* value will lead to higher efficiency because the parasitic resistance in the ultracapacitor is lower when more strings are connected in parallel. However, substituting the maximum and minimum *Cp* and *Bs* values into the equation for overall efficiency does not provide reliable results because the constraints on *Cs* and *Bs* are not being applied. Thus, it appears adequate to numerically estimate *maxeff* and *mineff*, with the possibility of refining the estimate in later optimizations. For example, simulations show that an ESS efficiency range of 0.92 to 0.98 is reasonable for the fuel cell powered SUV under study with a 40-kW fuel cell. It is important to note that this approximation only affects the calculation of scaling constants x and y, and thus the effect of changing the weightings a, b, and c. There is no approximation required in the actual efficiency calculation.

$$\Delta Cost = maxcost - mincost \tag{5-116}$$

$$\Delta Mass = maxmass - minmass \tag{5-117}$$

$$\Delta Eff = maxeff - mineff \tag{5-118}$$

Equation (5-119) is used to solve for x and y, on the premise that the overall difference in efficiency, cost, and mass should be similar so that the weightings a, b, and c have the desired effect. The solutions for x and y are shown in Equations (5-120) and (5-121) respectively.

$$x \cdot \Delta Eff = \Delta Cost = y \cdot \Delta Mass \tag{5-119}$$

$$x = \frac{\Delta Cost}{\Delta Eff} \tag{5-120}$$

$$y = \frac{\Delta Cost}{\Delta Mass} \tag{5-121}$$

5.8 Numerical Examples of the Optimization Method

The optimization method will be demonstrated by providing numerical examples of two systems. Example 1 consists of results for Option 1 and Option 2 of the novel topology for the system specified in the third column of Table 5-3 and Example 2 consists of results for both options for the system specified in the fourth column of Table 5-3. The only differences between Example 1 and Example 2 are in the values for the efficiency (*a*), cost (*b*), and mass (*c*) weightings, which affects only the objective function. Both Example 1 and Example 2 use the power profile shown in Figure 5-4 to obtain the values for *P*, *E*, *Pr*, and *Er*. Table 5-4 lists the component variable values used in both examples. The battery is modeled from the same A123 System lithium-ion cells used in Chapter 4 and the ultracapacitor is modeled from the same Maxwell Ultracapacitor 350-F cells used in Chapter 4.

The mathematical software *Maple 11* is used to perform the optimization using the non-linear program solver, *NLPSolve*. The command used to solve the optimization problem is shown in Equation (5-122), where *obj* is set equal to the objective function to be maximized given in Section 5.7, and *constraints* is set equal to the five constraints derived in Section 5.6. The initial search points are set to *Bsmin* and *Cpmin* to accelerate the solver runtime.

$$\begin{gathered} Optimization[NLPSolve](\mathrm{obj}, \ \mathrm{constraints}, \mathrm{assume} = \mathrm{nonnegative}, \\ initialpoint = \{Bs = Bsmin, Cp = Cpmin\}, maximize) \end{gathered} \tag{5-122}$$

Table 5-3: System Variable Values

Variable Symbol	Variable Name (units)	Variable Value (Example 1)	Variable Value (Example 2)
Vup	Upper load voltage (V)	425 V	425 V
Vlow	Lower load voltage (V)	250 V	250 V
P	Maximum positive power (W)	48,000 W	48,000 W
E	Maximum positive energy (J)	200,000 J	200,000 J
Pr	Maximum negative power (W)	20,870 W	20,870 W
Er	Maximum negative energy (J)	200,000 J	200,000 J
a	Efficiency weighting term	0.45	0.60
b	Cost weighting term	0.35	0.25
c	Mass weighting term	0.2	0.15

Table 5-4: Component Variable Values From Component Datasheets

Component	Variable Symbol	Variable Value
Battery	*Vcellb*	3.3 V
	Rcellb	0.01 Ω
	ibcell	80 A
	ibcellneg	10 A
	massbcell	0.123 kg
	costbcell	\$ 19.83 (USD)
	columbiceff	0.95
Ultracapacitor	*Vcellc*	2.5 V
	Rcellc	0.0032 Ω
	iccell	85 A
	Ccell	350 F
	massccell	0.113 kg
	costccell	\$ 14 (USD)
Diode	*Vd*	1 V
	massdperA	0.00136 kg/A
	costdperA	\$ 0.15/A (USD)
Switch	*Vs*	1 V
	massSperA	0.00015 kg/A
	costSperA	\$ 0.125/A (USD)

Equations (5-123) to (5-128) give the calculated values for *Bp*, *Cs*, *Bsmin*, *Cpmin*, *Bsmaxapprox*, and *Cpmaxapprox* for both Option 1 and Option 2. The maximum approximations for *Bs* and *Cp* are given for the purpose of showing the approximate search space.

$$Bp = ceil\left(\frac{P}{Vlow \cdot ibcell}\right) = 3 \tag{5-123}$$

$$Cs = ceil\left(\frac{Vup}{Vcellc}\right) = 170 \tag{5-124}$$

$$Bsmin = ceil\left(\frac{Vlow}{Vcellb - Rcellb\ ibcell} \right) = 100 \tag{5-125}$$

$$Cpmin = ceil\left(\frac{P}{iccell \cdot (Vup - iccell \cdot \alpha)} \right) = 2 \tag{5-126}$$

$$Bsmaxapprox = 118 \tag{5-127}$$

$$Cpmaxapprox = 5 \tag{5-128}$$

The efficiency of the acceleration phase, *Effaccel* from Equation (5-40), is examined in Figure 5-6. The *Effaccel* function is the same for both Option 1 and Option 2 since the only difference between the options is in the calculation of efficiency during the regenerative braking phase. Figure 5-6 shows that when *Cp* is large and *Bs* is small, the efficiency becomes greater than 1 (100%), which cannot be true in a real system. The explanation is as follows: when *Cp* is large and *Bs* is small, the ultracapacitor is able to provide the total energy required, *E*, without the ultracapacitor voltage decreasing to the battery voltage, since it has a large capacitance and the battery has a low voltage. Since the *Effaccel* equation was derived under the assumption that the ultracapacitor voltage decreases enough to allow the diode to conduct before energy *E* is supplied to the load, the equation does not hold when this assumption is not true, and *Effaccel* reaches meaningless values above 100%. Constraint 4, given in Equation (5-104), specifies the relationship between *Bs* and *Cp* to ensure that the equation for *Effaccel* is indeed valid, and thus the non-linear program solver is restricted to this valid search space.

When considering the valid range where *Effaccel* is less than 100%, two general conclusions can be made. Figure 5-6 shows that for a constant *Cp*, efficiency increases as *Bs* increases. The reasoning is as follows: a higher number of batteries in series, *Bs*, creates a higher battery voltage, and hence a higher bus voltage when the battery is providing power. Since the load current, *IL*, is constant for a given *Cp*, a higher bus voltage means higher power is provided at the load. Thus, the ratio of power provided to the load to I^2R power lost in the battery and ultracapacitor increases as *Bs* increases, meaning the efficiency also increases. This relation is also true in the case of a real vehicle where the current required is not constant: for a given power requirement, a higher bus voltage means lower current is needed to fulfill the power requirement, meaning I^2R losses are reduced as *Bs* increases, and the efficiency in the acceleration phase increases as *Bs* increases.

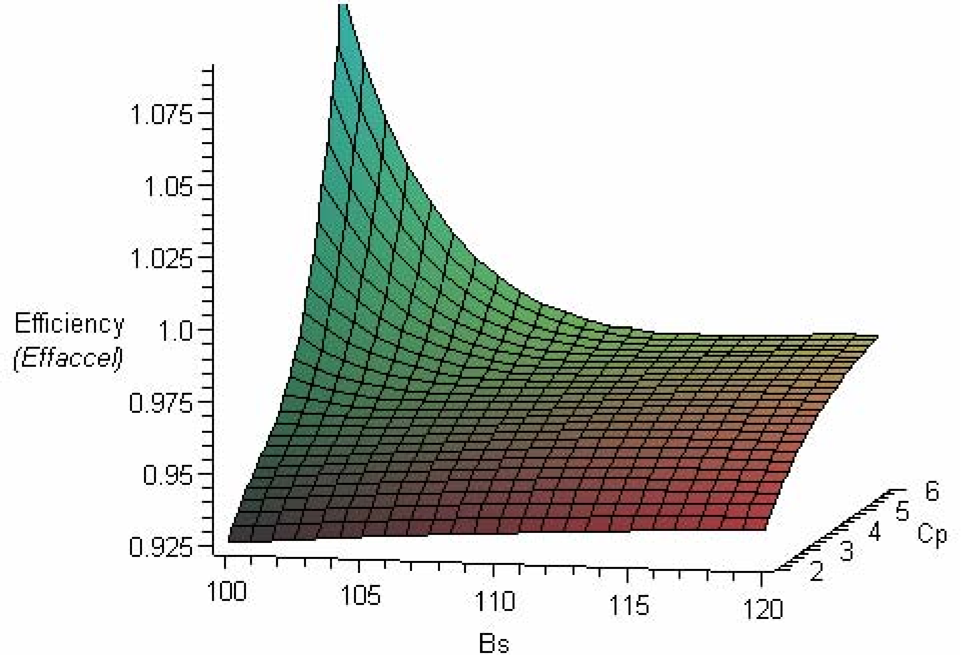

Figure 5-6: Efficiency of acceleration phase for Options 1 and 2 (Examples 1 and 2)

The second general conclusion is regarding the relationship between *Cp* and *Effaccel* (ignoring the invalid region where *Effaccel* > 100%). Figure 5-6 shows that for a constant *Bs*, *Effaccel* increases as *Cp* increases. The reasoning is as follows: a larger *Cp* means a lower overall internal resistance in the ultracapacitor pack, meaning I^2R losses are reduced. Lower I^2R losses in the ultracapacitor lead to higher overall efficiency in the acceleration phase, for both the model and for a real vehicle.

The efficiency during the regenerative braking phase for Option 1, *Effbrake* from Equation (5-65), is shown in Figure 5-7. Figure 5-7 shows that for a constant value of *Cp*, efficiency increases as *Bs* increases. This occurs for the same reason as in the acceleration phase: higher *Bs* creates a higher battery voltage and thus a higher ultracapacitor starting voltage since $vc(0) = Vb\text{-}Vd$ in the regenerative braking phase. This higher bus voltage means that more power is transferred from the load to the ultracapacitor than for a lower bus voltage, while the I^2R losses in the ultracapacitor remain the same. Again, this relationship holds true in a real vehicle that may have a certain regenerative braking power input because a higher ultracapacitor voltage means less current is required and lower I^2R losses are produced. However, a higher battery voltage means there is less room in the ultracapacitor to store regenerative braking energy before the ultracapacitor become fully charged to *Vup*. Figure 5-7 does not include this factor, but Constraint 5 is used in the optimization procedure to ensure that the battery voltage is low enough so that the ultracapacitor can accept the required regenerative braking energy, *Er*, before reaching *Vup*.

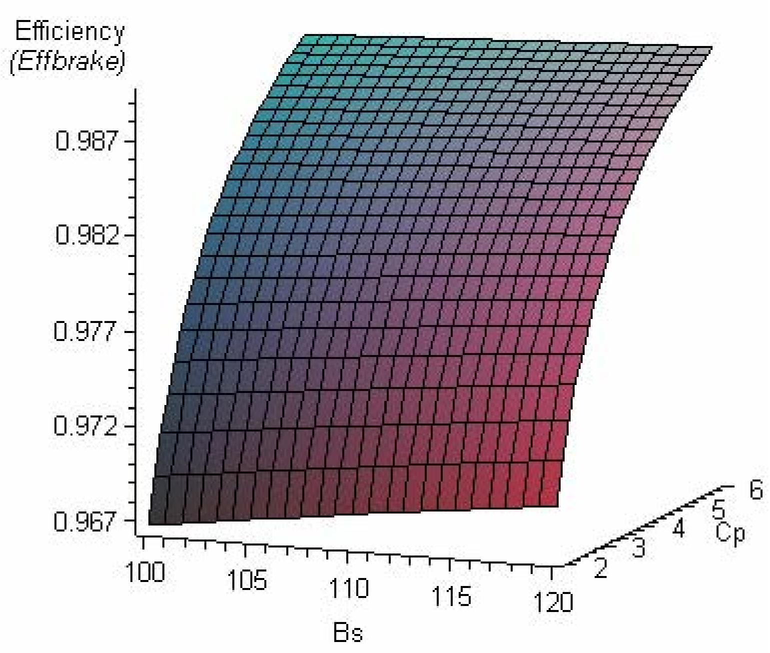

Figure 5-7: Efficiency of regenerative braking phase for Option 1 (Examples 1 and 2)

The efficiency during the regenerative braking phase for Option 2, *Effbrake* from Equation (5-86), is shown in Figure 5-8. In contrast to the relationship between *Bs* and *Effbrake* for Option 1, Figure 5-8 shows that for a constant value of *Cp*, efficiency increases as *Bs decreases*. This occurs because when the battery voltage, and hence initial ultracapacitor voltage, is low, there is more room for the more efficient ultracapacitor to accept regenerative braking energy after the less efficient battery has finished accepting regenerative braking energy (due to the battery reaching it's negative current limit). This concept is best illustrated by examining the efficiencies and energy transfers associated with each phase of the regenerative braking event, as shown in Table 5-5 (data for *Cp* = 3). The data in Table 5-5 shows that in each phase (Phase 1 – battery and ultracapacitor accepting power, Phase 2 – only ultracapacitor accepting power), the efficiency is higher when *Bs* is higher, verifying that the principles discussed previously for the acceleration phase and the regenerative braking phase for Option 1 still apply to this case. For example, the efficiency in Phase 1, *Effbrake1*, is higher when *Bs* = 120 than when *Bs* = 100 since the bus voltage is higher. However, it can be seen that the proportion of energy stored in the ultracapacitor is much larger when *Bs* is small and thus the generally higher ultracapacitor charging efficiency has a larger role in determining the overall efficiency. Thus, the overall efficiency is higher when *Bs* is lower. Again, Constraint 5 is used to ensure that the ESS system is adequately sized to accept the required regenerative braking energy, *Er*.

Figure 5-7 and Figure 5-8 show that the efficiency during regenerative braking for both options increases as *Cp* increases. This result matches the result found for the acceleration phase, and the reasoning is the same: a larger *Cp* means a lower overall internal resistance in the ultracapacitor pack, meaning I^2R losses are reduced.

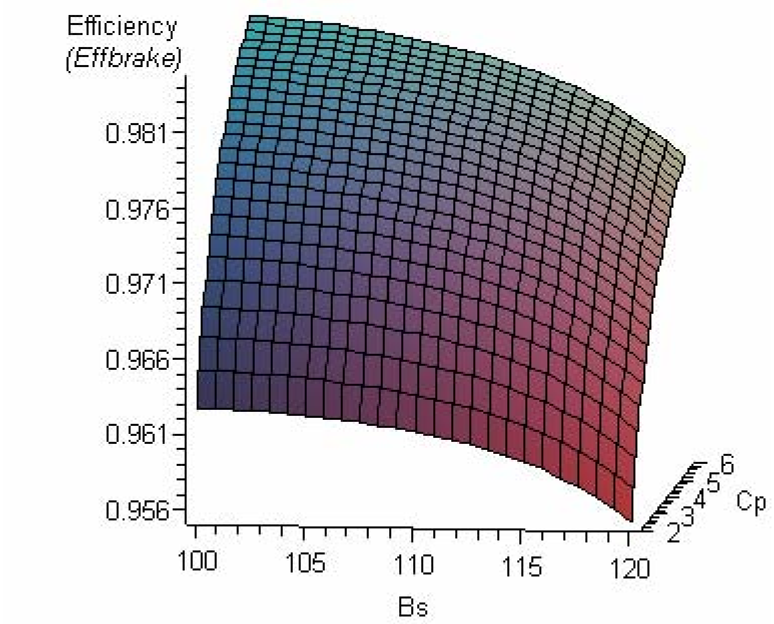

Figure 5-8: Efficiency of regenerative braking phase for Option 2 (Examples 1 and 2)

Table 5-5: Analysis of Regenerative Braking Efficiency for Option 2

	Description	**Value for *Bs* = 100**	**Value for *Bs* = 120**
Ebatt	Energy stored in battery during Phase 1	14,754.62 J	20,713.2 J
Ecap1	Energy stored in ultracapacitor in Phase 1	17,921.52 J	26,494.12 J
Ein1	Energy sent into ESS in Phase 1	34,538.13 J	49,670.59 J
Effbrake1	Efficiency of braking in Phase 1 $= \dfrac{Ebatt + Ecap1}{Ein1}$	94.61%	95.04%
Ecap2	Energy stored in ultracapacitor in Phase 2	205,617.29 J	49,476.46
Ein2	Energy sent into ESS in Phase 2	210,322.03 J	50,515.85
Effbrake2	Efficiency of braking in Phase 2 $= \dfrac{Ecap2}{Ein2}$	97.76%	97.94%
Effbrake	Total efficiency of regenerative braking = $\dfrac{Ein1 \cdot Effbrake1 + Ein2 \cdot Effbrake2}{Ein1 + Ein2}$	97.32%	96.5%

Figure 5-9 and Figure 5-10 show the overall efficiency, *Eff*, as calculated in Equation (5-108), for both Option 1 and Option 2, respectively. The main difference is that for Option 1, efficiency increases as *Bs* increases (since this happens in both the acceleration and regenerative braking phases), but for Option 2 there is no clear increase/decrease relationship for efficiency as *Bs* increases. This is because the total efficiency is a combination of the acceleration and regenerative braking efficiencies, and for Option 2, efficiency increases as *Bs* increases in the acceleration phase and efficiency decreases as *Bs* increases in the regenerative braking phase. It is useful to note that the expression for efficiency in terms of *Bs* and *Cp* is derived to provide a fair assessment of the effect of battery and ultracapacitor sizing on the ESS efficiency during a common acceleration-braking cycle for the given drive cycle, and that the actual efficiency over different acceleration-braking cycles will not necessarily match this result; however, the general trends will still apply.

Figure 5-11 and Figure 5-12 show the objective function for Example 1, as calculated in Equation (5-107), for Option 1 and Option 2, respectively. Table 5-6 shows the optimization results for *Bs* and *Cp* when the non-linear program solver command (Equation (5-122)) is applied for the objective function for both options for Examples 1 and 2.

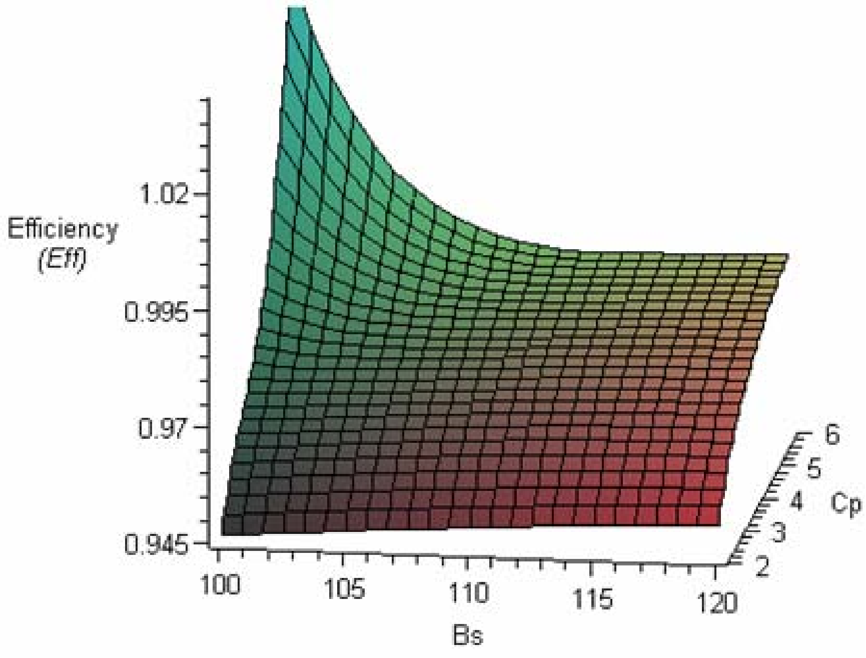

Figure 5-9: Overall efficiency for Option 1 (Examples 1 and 2)

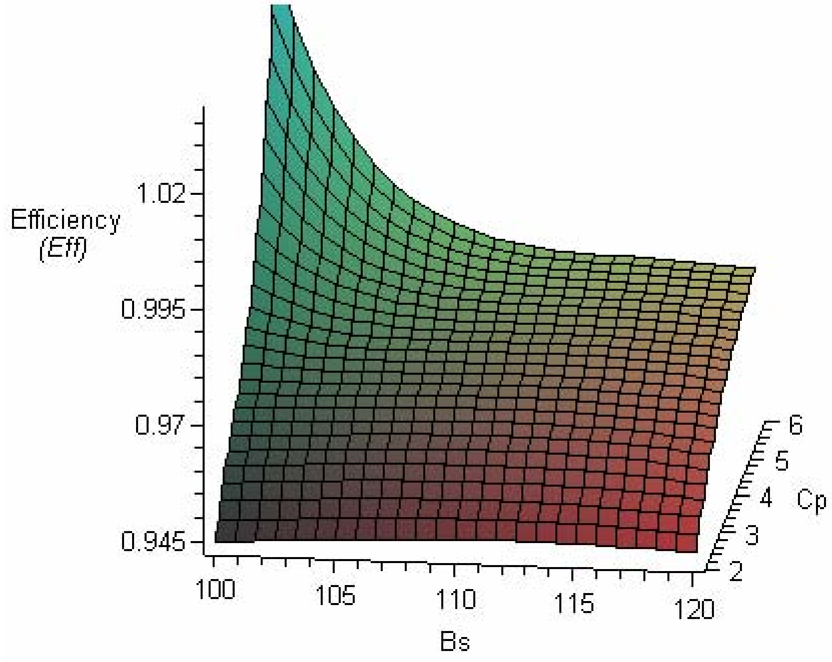

Figure 5-10: Overall efficiency for Option 2 (Examples 1 and 2)

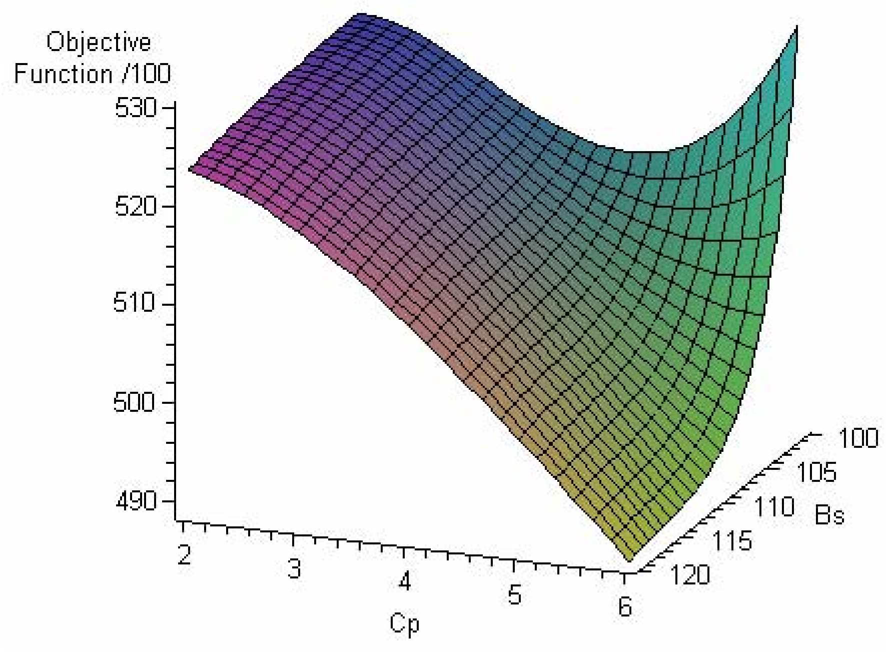

Figure 5-11: Example 1 objective function for Option 1

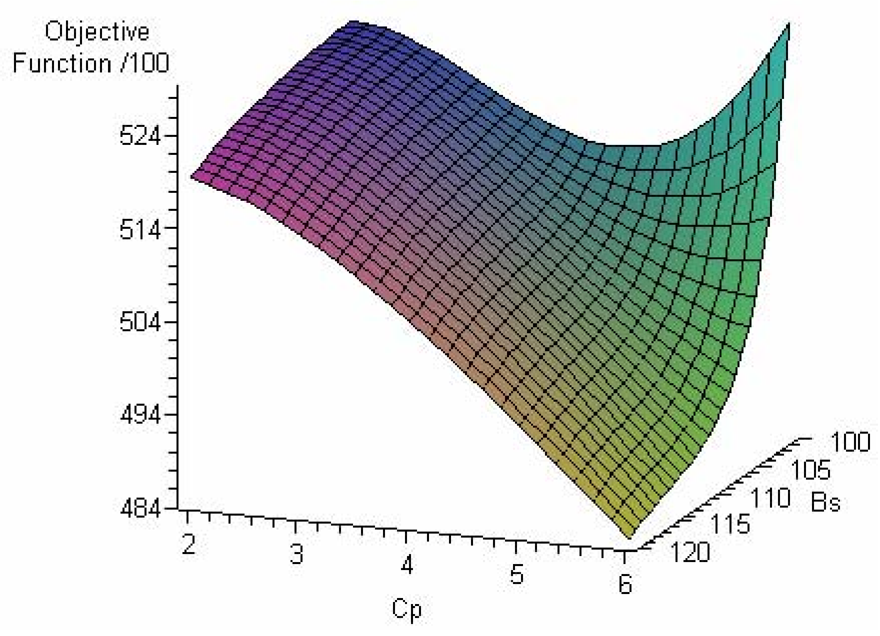

Figure 5-12: Example 1 objective function for Option 2

Table 5-6: Optimization Results for Example 1 and Example 2

Optimization Variable	**Example 1** ***Efficiency:*** $a = 0.45$ ***Cost:*** $b = 0.35$ ***Mass:*** $c = 0.2$		**Example 2** ***Efficiency:*** $a = 0.60$ ***Cost:*** $b = 0.25$ ***Mass:*** $c = 0.15$	
	Option 1	**Option 2**	**Option 1**	**Option 2**
Bs	100	100	103.425	104.114
Cp	2.615	2.436	2.929	2.755

Note that for both examples, Constraint 1 has set the minimum number of battery cells in series, *Bsmin*, to 100 to avoid exceeding the lower voltage of the system (*Vlow* = 250 V) when the battery is providing rated current. In Example 1, the optimal result for the objective function subject to the constraints is obtained when *Bs* = 100, as shown in Table 5-6. Thus, in this case, Constraint 1 is the limiting factor in reaching an optimal value for *Bs*. This result matches the results of the parametric study in Chapter 4, where the optimal *Bs* value was also found to be 100, given the same weightings on efficiency (0.45), cost (0.35), and mass (0.2). The optimal results for *Cp* for Example 1 show that when *Bs* is the same for both Option 1 and Option 2, the optimal *Cp* value is lower for Option 2. This is the expected result because Option 2 uses the battery to store some regenerative braking energy, and thus requires a smaller ultracapacitor to ensure that the total regenerative braking energy, *Er*, is accepted by the ESS.

In Example 2, a higher weighting is placed on efficiency (0.6) in the objective function, and thus smaller weightings are used for cost (0.25) and mass (0.15). For Option 1, it was shown that both acceleration and regenerative braking efficiency increase as *Bs* and *Cp* increase within the search space under study. Thus, it is expected that the optimization results for Example 2 produce larger optimal *Bs* and *Cp* values than for Example 1, since maximizing efficiency is now a higher priority and minimizing cost and mass is now a lower priority. The optimization results shown in Table 5-6 match this expectation, and thus it is shown that the optimal *Bs* value does not always coincide with *Bsmin* from Constraint 1.

For Option 2, it was found that the overall efficiency (including both acceleration and regenerative braking phases) is higher when *Cp* is large and when *Bs* is greater than its minimum value of 100, as shown in Figure 5-10. Therefore, the same reasoning holds with regards to the larger optimal *Bs* and *Cp* values obtained in Example 2 when efficiency has a larger weighting. The results for Example 2 also verify that when the battery sizes are approximately the same for both options, Option 2 has a lower optimal *Cp* value because less capacitance is required to store regenerative braking energy, *Er*, since the battery absorbs some of this energy. Overall, the results and analysis for both examples match the theoretical expectations of optimal ESS component sizing in a real vehicle.

Although it is not a general principle that rounding fractional optimal values results in optimal integer values, it has been verified numerically for these examples, and for other similar systems, that the fractional optimization results can be rounded to the nearest integer to obtain the optimal integer values for *Bs* and *Cp*. This method works in this case due to the smooth and gradual nature of the objective function, especially for the systems shown in these examples. Furthermore, since the objective function is given as a function of *Bs* and *Cp*, it is very simple to check both the next lower and the next higher integer values for a given fractional result to see if rounding up or down gives the higher objective function value. The advantage of the method giving fractional optimization results is that a designer can see the absolute optimum values of battery voltage and ultracapacitor capacitance. This is important in cases where a designer has the choice of different models of batteries and/or ultracapacitors to use, as they can choose the component type to match the optimal battery voltage or ultracapacitor capacitance. This becomes even more important if the company designing the ESS system is also designing the actual battery and/or ultracapacitor cell, and can thus create a custom-made cell which matches the optimal values exactly.

5.9 Summary

Chapter 5 has presented an analytical optimization method to determine optimal sizes of the battery and ultracapacitor in the novel battery-ultracapacitor ESS topology. Information is extracted from the ESS power requirements for a given drive cycle to design an optimal system based on efficiency, cost, and mass of the ESS. Analysis of various functions has given deeper insight into the effects of battery and ultracapacitor sizing on the efficiency of the system in acceleration and regenerative braking modes. The results for the examples shown illustrate how changing objective-function parameters affects the optimization results. Overall, this optimization method gives engineers an analytical tool for creating an optimal design of the novel battery-ultracapacitor topology, while providing insight into the relationship between battery and ultracapacitor sizing and system efficiency.

Chapter 6

Capacitor-Switched Regenerative Snubber for Boost Converters

6.1 Introduction To Soft-Switching Circuits for DC/DC Converters

High-power DC/DC converters are a crucial component of today's emerging vehicular technologies, such as hybrid-electric, battery-electric, and fuel cell vehicles. Chapters 2, 3, and 4 have discussed the topology, control, and modeling of a boost converter used in a fuel cell vehicle. In general, a voltage boost is required to step up the low voltage of the fuel cell or battery to the high voltage required by the electric motor inverter. In these applications, reducing the size and mass of the converter is imperative to allow ease of packaging and to provide higher fuel economy due to lower overall vehicle mass. High-efficiency operation is also crucial for further improvement of the fuel economy. Furthermore, the converter should be a simple design with a fast transient response, and should operate reliably over the entire load range. In addition to emerging vehicular systems, high-power DC/DC boost converters find applications in microturbine-based power generation systems and power factor correction schemes for single-phase front-end diode-rectifier circuits.

The large passive components used in high-power DC/DC boost converters, specifically the large boost inductor, comprise a major part of the mass of the converter. Thus, higher-frequency operation is imperative to reduce the size of the passive components so that high specific power, high power density, and also a fast transient response can be obtained. However, there are two major obstacles to achieving high-frequency operation for high-power (over 10kW) DC/DC converters. Firstly, the switching losses increase proportionally with the increased frequency, which reduces converter efficiency and increases cooling requirements. A larger cooling system adds extra cost and mass to the overall converter system. Secondly, and most problematically, the high-power IGBTs used in these converters are commonly limited to hard-switching operation at about 30kHz [55], or less, depending on the power level. The switching frequency limit exists to prevent overheating and failure of the IGBT. If soft-switching is used, the switching losses are reduced, and these IGBTs can operate at frequencies up to 70kHz [55], which can significantly reduce the size of the passive components in the converter without increasing the size of the heat sink. Thus, it can be concluded that an appropriate soft-switching circuit should be used in high-power boost converters for vehicular applications so that switching frequency can be increased, passive component sizes can be decreased, and high specific power and high power density objectives can be met.

In recent years, a number of techniques and circuits have been proposed to reduce the switching losses in DC/DC boost converters. In resonant and quasi-resonant converters, the devices are turned off and/or on at zero-voltage or zero-current of a resonant mode [58][59]. However, resonant converters require careful matching of the operating frequency to the resonant tank component values and operation failure can occur if there is any magnetic saturation or unexpected drift in resonant frequency. Also, it can be difficult to design filters and control circuits because of the wide range of switching frequency variations. Furthermore, the addition of one or more high-power inductors for the resonant circuit, which can have significant mass due to the high current rating required, can partially or fully negate the benefit of using a higher switching frequency to try to increase the specific power of the converter.

Passive soft-switching methods [60][61][62][63] use only passive components to achieve zero-voltage or zero-current switching at a constant switching frequency. The auxiliary circuits can be very complicated and require numerous extra components, including extra inductors. Again, the high current rating required for the extra inductors in high-power converters adds significant mass to the converter and can partially or fully negate the mass reduction accomplished by using a higher switching frequency. Also, many of the proposed passive methods are designed for low-power boost converters using MOSFETs and hence focus on reducing the reverse-recovery losses during turn-on of the switch (due to the boost diode) rather than the more significant turn-off losses found in high-power converters using IGBTS. However, new silicon carbide (SiC) diodes have nearly zero reverse-recovery current and can be implemented as the boost diode to virtually eliminate turn-on losses of the switch [64]. Finally, passive methods can cause higher component stresses and have generally been shown to provide only marginal reductions in switching losses.

Active soft-switching methods [65][66][67][68][69][70][71] use one or more auxiliary switches in addition to passive components to achieve zero-voltage or zero-current switching. Some disadvantages of active methods are in complexity of control or limitations in terms of voltage-boost range and load range. Many active methods proposed also focus on the reverse recovery losses at turn-on of the main switch, though this problem can now be easily remedied through the use of SiC boost diodes. Finally, some active methods have hard-switching of the auxiliary switch(es) and many have a high component count, including heavy extra inductors.

The literature review reveals that there is a need for a simple and efficient method for increasing the switching frequency of high-power boost converters without adding extra heavy inductors so that the converter mass can be reduced, which is essential for vehicular applications. Thus, this chapter introduces the capacitor-switched regenerative snubber for high-power boost converters. The circuit is simple, highly efficient, operates over the entire load range, and has a straightforward control strategy. Also, as high-power magnetic components comprise a significant portion of a circuit's mass, volume, and cost, the capacitor-switched regenerative snubber circuit is designed to require no additional inductors. The only additional components required are two IGBTs (which are connected as a leg, and can be easily implemented as a dual IGBT module), two diodes, and one snubber capacitor. The goal of the circuit is to reduce the mass and increase the efficiency of the high-power DC/DC boost converter.

6.2 Proposed Capacitor-Switched Regenerative Snubber Circuit

6.2.1 Circuit Design

In high-power IGBT-based DC/DC boost converters, the switch turn-off loss is generally greater than the turn-on loss. This high value of turn-off losses in an IGBT can be explained by the fact that there is a significant current tail as the voltage across the switch rises rapidly during turn-off. The turn-on loss, however, can be significantly reduced by reducing or eliminating the reverse recovery current of the boost diode. This can now be easily achieved by using Silicon Carbide (SiC) diodes, since they exhibit virtually zero reverse-recovery current [64]. Thus, the proposed capacitor-switched regenerative snubber circuit focuses on reducing the significant turn-off losses in high-power boost converters so that high switching frequencies can be obtained without exceeding the IGBT's thermal limits.

The circuit diagram of a conventional boost converter is shown in Figure 6-1, complete with input and output filters to smooth the input current and the output voltage. The proposed regenerative snubber circuit is shown in Figure 6-2. The idea is to charge the snubber capacitor C_s at one turn-off event and then discharge it at the next turn-off event. With this operation, the voltage rise across the switch is slowed down and the current tail through the switch is reduced at each turn-off, and virtually all of the energy used to accomplish this is returned to the output circuit. To realize this operation, the connection of the snubber capacitor to the main switch S_1 must be reversed for every turn-off, so that the charging and discharging actions bring the voltage across the snubber capacitor from 0 V to V_{out} and vice versa.

At the first turn-off of S_1, shown in Figure 6-3, auxiliary switch S_3 is on and auxiliary switch S_2 is off so that current flows through D_2 and S_3 to charge the snubber capacitor C_s from 0 V to the output voltage level, V_{out}. This charging action slows down the voltage rise across switch S_1, greatly reducing the losses while the current in the switch S_1 falls quickly. At the next turn-on, both S_2 and S_3 are off as shown in Figure 6-4; thus, the operation of S_1 at turn-on is unaffected by the snubber circuit. At the next turn-off of S_1 (shown in Figure 6-5), S_2 is on and S_3 is off; thus, the current flows through S_2 and D_3 to discharge the snubber capacitor. Again, this action greatly slows down the voltage rise across S_1 and reduces the current tail through S_1. All the energy stored in the snubber capacitor is transferred to the output of the circuit, leading to a very efficient design.

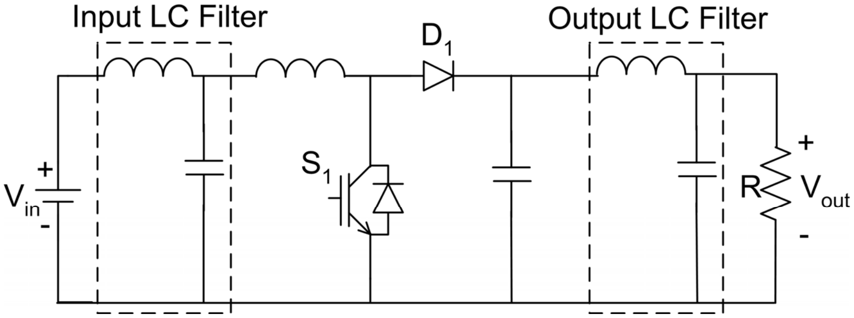

Figure 6-1: Conventional hard-switched boost converter

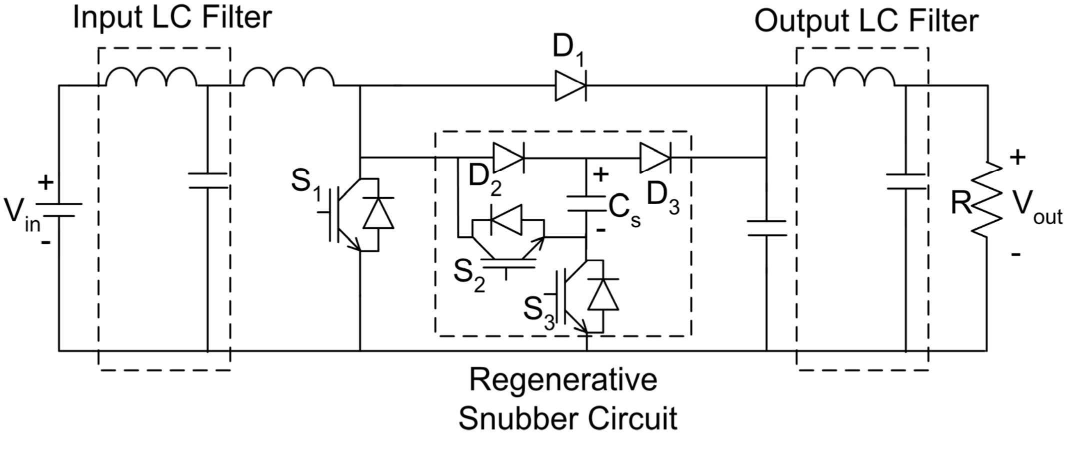

Figure 6-2: Boost converter with the proposed regenerative snubber

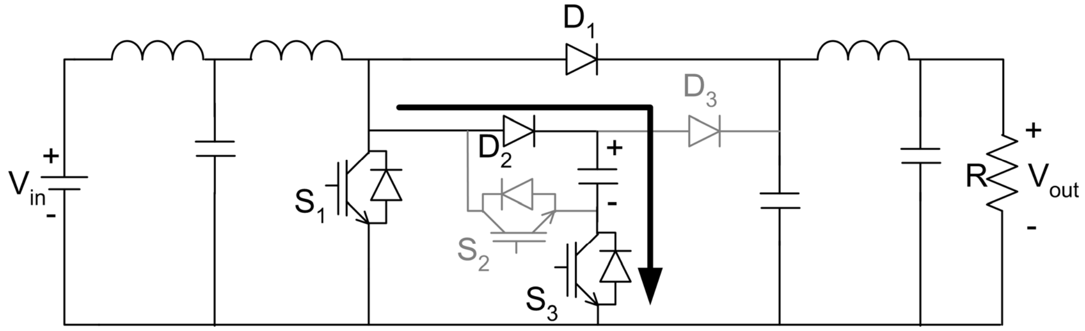

Figure 6-3: Operation of proposed regenerative snubber during first turn-off of S_1 (charging snubber capacitor)

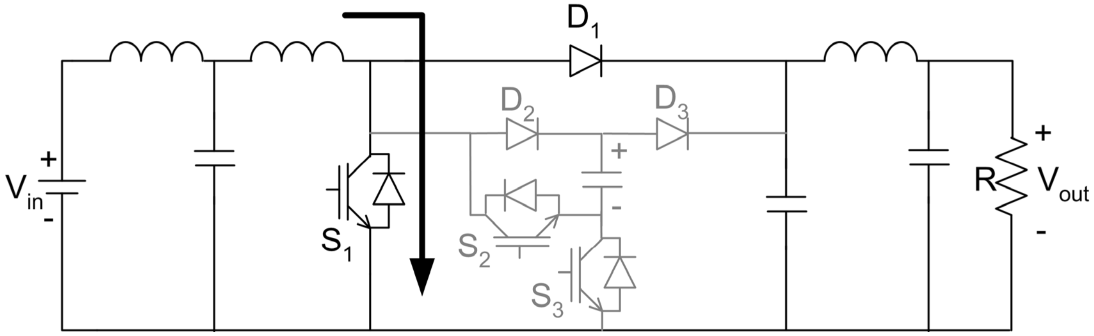

Figure 6-4: Operation of proposed regenerative snubber during any turn-on of S_1

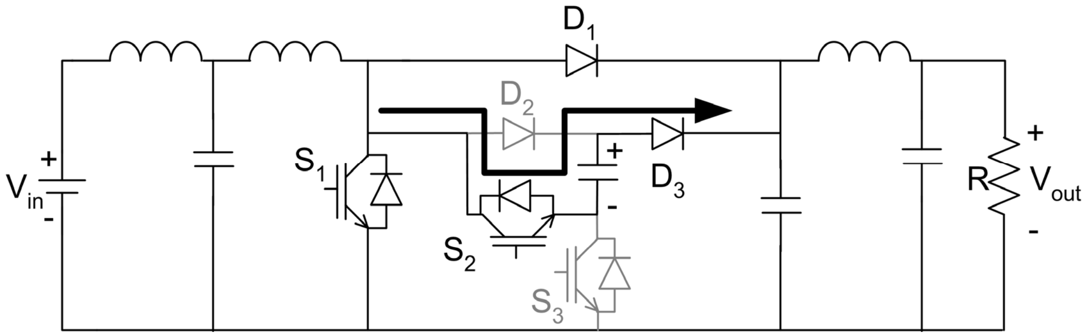

Figure 6-5: Operation of proposed regenerative snubber during second turn-off of S_1 (discharging snubber capacitor)

The only losses introduced into the converter by the snubber circuit are the short pulses of conduction loss in the auxiliary diodes. The auxiliary switches do not add further conduction losses compared to the hard-switched converter because the auxiliary IGBTs augment the on-time of the main switch, S_1. Thus, the main switch in the regenerative snubber converter is on for a shorter time than the main switch in the hard-switched converter to achieve the same voltage boost, and each auxiliary switch conducts for a period of time to make the total IGBT conduction time equal in the two converters. Also, due to the nature of the circuit, both auxiliary switches operate with zero-voltage turn-on and zero-voltage and zero-current turn-off; thus, virtually no switching losses are introduced [72]. Effectively, the current is commutated from the main switch (where a turn-off event would generate large losses due to the voltage rise across the switch) to an auxiliary switch, which has a zero-voltage and zero-current turn-off. Overall, the additional conduction losses in the auxiliary diodes, which are quantified in Section 6.3.1, are small in comparison with the reduction in the losses of the main switch at turn-off.

Many active methods used to reduce switching losses employ one auxiliary switch and one or more additional high-power inductors in the circuit. In the proposed capacitor-switched regenerative snubber circuit, the trade-off for requiring no additional inductors to achieve soft-switching is that two auxiliary switches are used. For the purpose of reducing the mass of high-power boost converters, this trade-off is desirable because the mass of the inductor is usually larger than that of the switch. Furthermore, the proposed circuit has two features which minimize the problems generally associated with using two auxiliary switches: (i) the auxiliary switches are connected in a leg arrangement, which is commonly offered by semiconductor manufacturers as a dual module – this reduces the physical component count and simplifies the layout, and (ii) the control strategy for both auxiliary switches is simple and requires no feedback or precise calculations or timing, as will be discussed in the next section.

6.2.2 Control Strategy

The control strategy required to operate the main and auxiliary switches is very simple and can easily be implemented on a microcontroller. No additional sensors or feedback are required for the auxiliary switches. Figure 6-6 shows the required gating signals. The auxiliary switches must turn on before the main switch turns off and they must turn off before the main switch turns back on. The auxiliary switches have a constant duty cycle to facilitate charging (S_3 on) and discharging (S_2 on) of the snubber capacitor. The duty cycle of the main switch can be changed by changing the turn-on time, while keeping the turn-off time in sync with the auxiliary switch turn-on times.

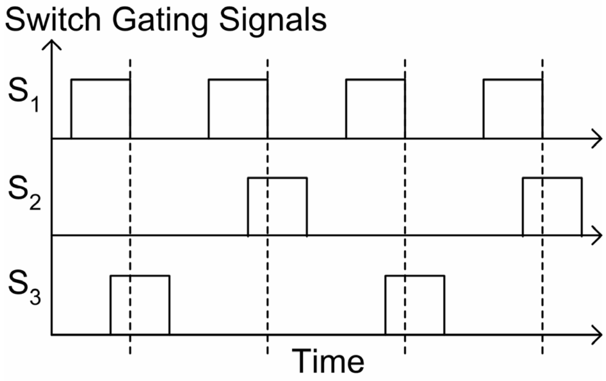

Figure 6-6: Required gating signals for switches S_1, S_2, and S_3

The boost converter is not practical for use with very high-voltage boosts (due to parasitic losses) [56], and so, very high duty cycles are not usually required. Thus, the fact that the snubber capacitor must finish charging or discharging before switch S_1 turns on does not pose any practical limitation on the switch duty cycle. Furthermore, the benefit of reduced turn-off losses can be achieved using a very small snubber capacitor (which also minimizes the conduction losses of the auxiliary circuit), that charges up quickly and poses virtually no restriction on switch duty cycle.

Simulations were performed using PSPICE to characterize the behaviour of the planned 5-kW prototype. The results are shown in Figure 6-7 to illustrate the timing of the gating signals for the three switches in the converter, as well as the voltages across and currents through the switches and the snubber capacitor. Figure 6-7 shows that there are no switching losses associated with the auxiliary switches, since they always turn on at zero voltage and turn off at zero voltage and zero current. For the simulation results shown here, an over-sized snubber capacitor was used to emphasize the theory of operation of the proposed circuit.

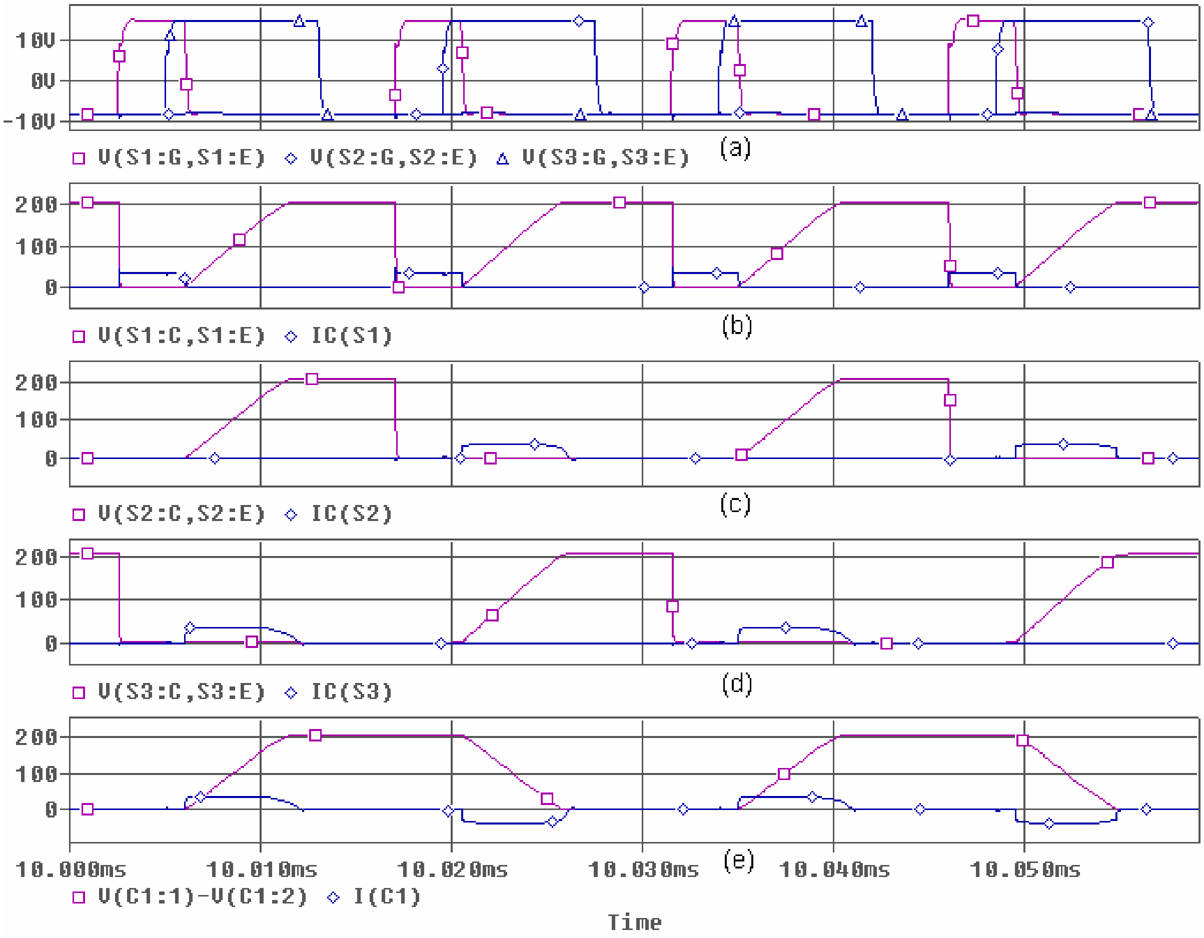

Figure 6-7: Simulation Results: (a) gating signals, (b, c, and d) voltages and currents of main and auxiliary switches, and (e) voltage and current of snubber capacitor

6.3 Experimental Prototype

In order to perform a comprehensive comparison between the capacitor-switched regenerative-snubber boost converter and the hard-switched boost converter in terms of mass, switch stress, and efficiency, two 5-kW boost converters, one with and the other without the snubber circuit, were designed, built, and tested. The IGBT used (specifications given in Table 6-1) was chosen because it is part of a product line of high-power IGBTs and it is capable of high-frequency operation due to its short turn-on and turn-off times. Using new switches with fast turn-on and turn-off times ensures the comparison between the two converters is relevant. This IGBT is oversized for the experimental prototype, and was chosen to be used for the main switch, S_1, for the following reasons:

1. It is a relatively high-power IGBT (rated at 150A) and has geometry and characteristics similar to other even higher-power switches in the product line. Thus, the switching waveforms both with and without the regenerative snubber give a clear indication of the switching loss reduction achieved from using the regenerative snubber circuit. It is imperative to use high-power type switches to analyze the benefit of the regenerative snubber, since it is designed for high-power converters and low-power switches can exhibit much different switching characteristics.
2. When building a prototype circuit, it is good practice to use over-sized components to avoid exceeding the thermal limits of the devices due to any unexpected circuit behaviour (e.g., EMI, control code bugs, etc.).

According to the PSPICE simulations, the auxiliary switches have peak and RMS current ratings that are slightly lower than those of the main switch [72]. However, the same IGBTs were used for the auxiliary and main switches in this prototype for the following reasons:

1. The IGBTs were available in the lab, and it was more practical to work with and build driver circuitry for the same type of switch. It is generally desirable to minimize the number of different parts required.
2. Again, it is good practice to use over-sized devices in a first prototype to reduce the possibility of over-heating the device due to any unexpected circuit behaviour.

Therefore, the experimental prototype can be seen as a proof-of-concept circuit where improvements in device selection could be made in a mass-produced converter. Specifically, smaller IGBTs can be used to decrease the additional mass of the auxiliary switches. The mass analysis is quantified in Section 6.3.2.

Cree Silicon Carbide (SiC) diodes [73] (model number CSD10060) are used in the experimental prototype. Each diode is rated at 10A and 600V, and exhibits nearly zero reverse recovery. Five diodes are used in parallel for each diode component D_1, D_2, and D_3 in order to meet the maximum forward current requirement of about 45A.

Table 6-1: Specifications for CM150DUS-12F IGBT

Maximum Collector-Emitter Voltage, V_{CES}	600V
Maximum Collector Current, I_C	150A
Turn-On Delay Time, $t_{d(on)}$	120 ns
Rise Time, t_r	100 ns
Turn-Off Delay Time, $t_{d(off)}$	350 ns
Fall Time, t_f	150 ns

Based on simulation results, the switching frequency for the capacitor-switched regenerative snubber converter was chosen to be 60kHz and the switching frequency for the hard-switched converter was chosen to be 30kHz. The simulation results showed that at these specified frequencies, the switching losses of the two converters would be approximately equal.

The hard-switched converter and the capacitor-switched regenerative-snubber converter use the exact same IGBTs, drivers, silicon-carbide diodes, filter capacitors, and boost capacitors. Copper busbars were designed and built for each converter to minimize parasitic inductance in the prototypes. The input filter inductors and boost inductors were custom-made for each converter by a magnetics company [54]. The input L-C filter for each converter uses a 2.2-mF electrolytic capacitor, and the inductance values were determined based on choosing the filter's resonant frequency to be approximately one decade below the switching frequency of each converter. The inductance of the main boost inductors for each converter was chosen to make the inductor current ripple approximately 8% at full power (45A input current). The output L-C filter was omitted to simplify the prototype construction. The circuit diagrams of the experimental set-ups are shown in Figure 6-8 and Figure 6-9 for the hard-switched and regenerative snubber converters, respectively. Photographs of both prototypes are shown in Appendix B.

The choice of size for the snubber capacitor should be made to minimize the capacitance as much as possible (to minimize conduction losses in the auxiliary components) while still ensuring the capacitor is large enough to slow down the voltage rise across the main switch in order to significantly reduce the turn-off losses. After the designer has determined the desired time for voltage rise, $\Delta t_{desired}$, the capacitance of the snubber capacitor, C_s, can be approximated by Equation (6-1).

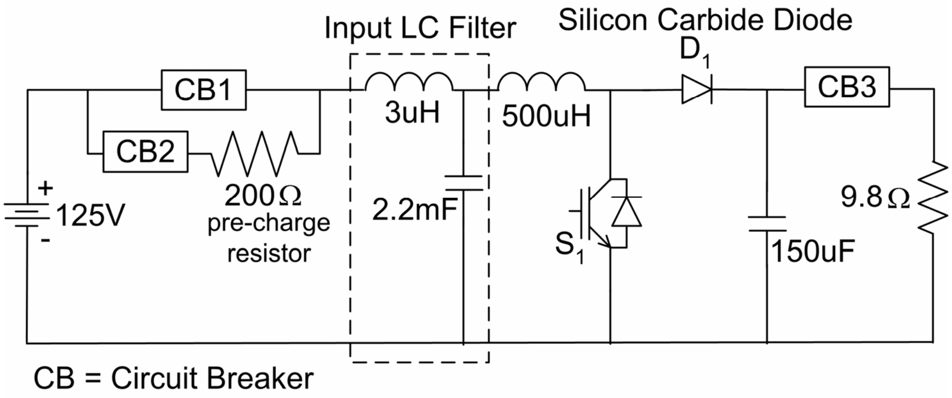

Figure 6-8: Hard-switched converter prototype

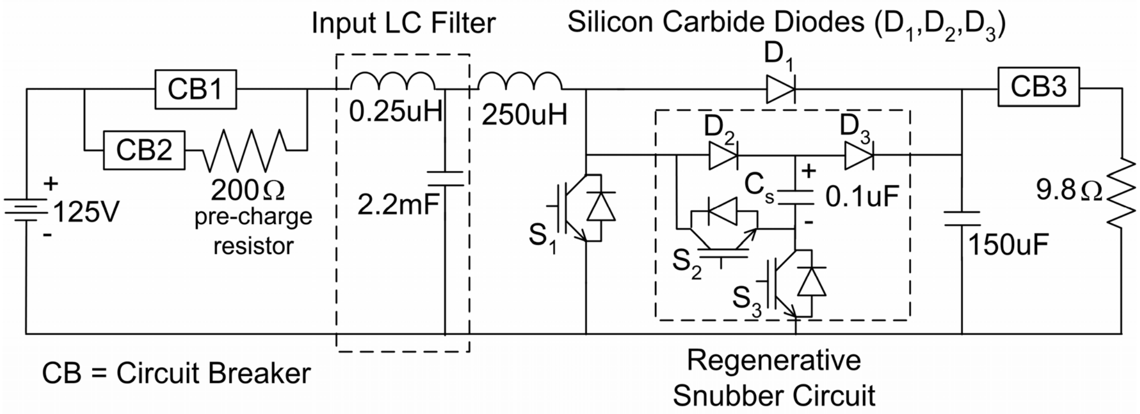

Figure 6-9: Regenerative-snubber converter prototype

$$C_s = I_{C,\max} \cdot \frac{\Delta t_{desired}}{V_{out,\max}} \tag{6-1}$$

In Equation (6-1), $I_{C,max}$ and $V_{out,max}$ are the maximum collector current for the main switch and the maximum output voltage, respectively. For example, in the experimental prototype, $V_{out,max}$ = 220V, $I_{C,max}$ = 45A, and $\Delta t_{desired}$ = 0.5 µs; therefore, C_s = 0.1 µF.

A microcontroller was programmed with the control strategy for use with the experimental prototypes. To decouple any effects caused by a closed-loop controller from the circuit behaviour, open-loop control was implemented. A potentiometer is used to alter the signal entering an A/D port on the microcontroller between 0 and 5V, to vary the duty cycle of the main switch, S_1. When S_1 begins switching, the auxiliary switch gating signals also become active, phase shifted by 180° with respect to one another. The auxiliary switches have a constant duty cycle, which should be set so that their on-time is slightly longer than $\Delta t_{desired}$, to allow for the auxiliary switches to be turned on just before the main switch turns off. There is no negative effect associated with having an auxiliary switch on after the snubber capacitor has been charged or discharged, as long as it is turned off before the main switch turns on again. A closed-loop current or voltage control scheme can be easily implemented, as the only change would be that a software control loop would control the main switch duty cycle rather than an analog signal from the potentiometer.

6.3.1 Experimental Results

The experimental results verify the operation of the regenerative snubber circuit and match well with the PSPICE simulation results. Figure 6-10 shows the voltage across and current through the switch in the hard-switched converter with a switching frequency of 30kHz and Figure 6-11 shows the slower rate of voltage rise across the main switch S_1 at turn-off in the capacitor-switched regenerative-snubber converter, with a switching frequency of 60kHz. Figures 6-10 and 6-11 also show that the maximum voltage spike (due to parasitic inductances) across the switch at turn-off is reduced from 244V in the hard-switched converter (a 22% peak over the output voltage of 200V) to 218V in the regenerative-snubber converter (a 9% peak over the output voltage of 200V), implying a considerable reduction in voltage stress.

Figure 6-12 and Figure 6-13 show detailed views of the voltage across and current through the main switch in the hard-switched and regenerative-snubber converter, respectively, during turn-off. Figure 6-13 shows that the regenerative snubber circuit reduces the turn-off losses by reducing the current tail and slowing the rate of voltage rise across the switch. Figure 6-14 and Figure 6-15 show detailed views of the voltage across and current through the main switch in the hard-switched and regenerative-snubber converter, respectively, during turn-on of S_1. The use of the SiC diodes has reduced the turn-on losses in both converters (compared to the loss expected if SiC diodes were not used) by removing the current spike that would be present at turn-on due to reverse recovery of the boost diodes [64].

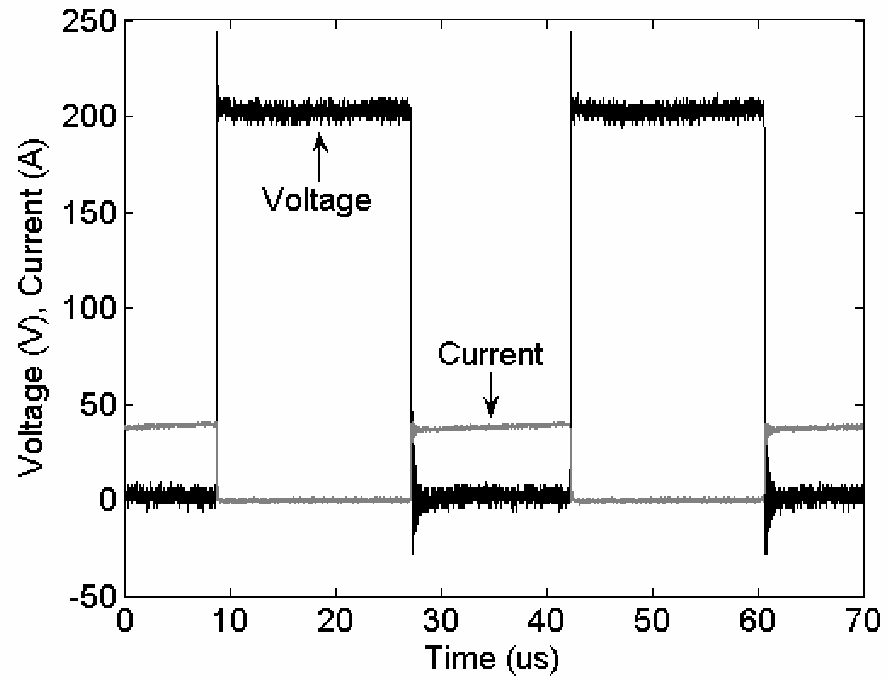

Figure 6-10: Voltage across and current through switch in hard-switched converter

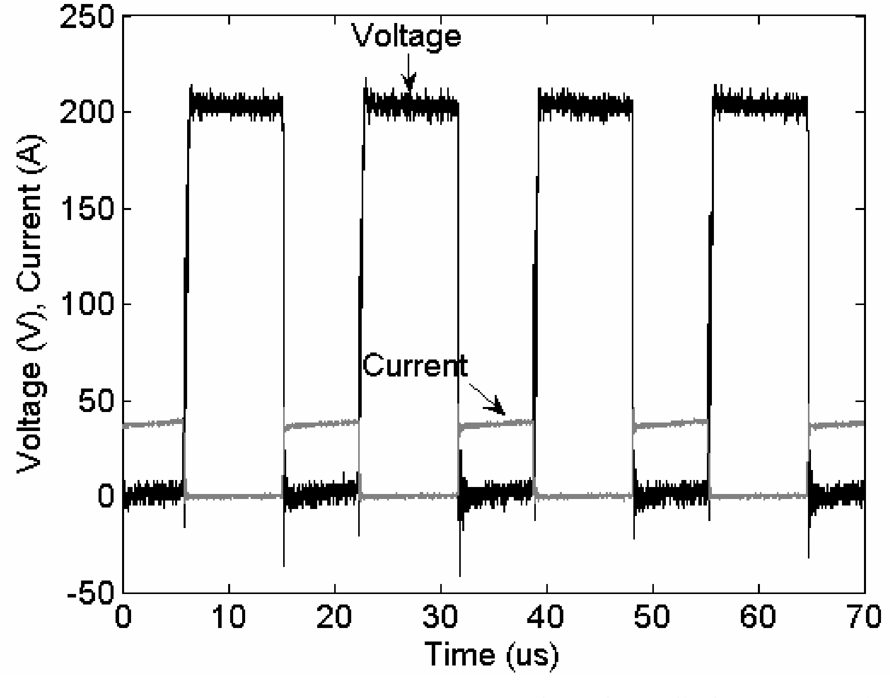

Figure 6-11: Voltage across and current through main switch (S_1) in regenerative-snubber converter

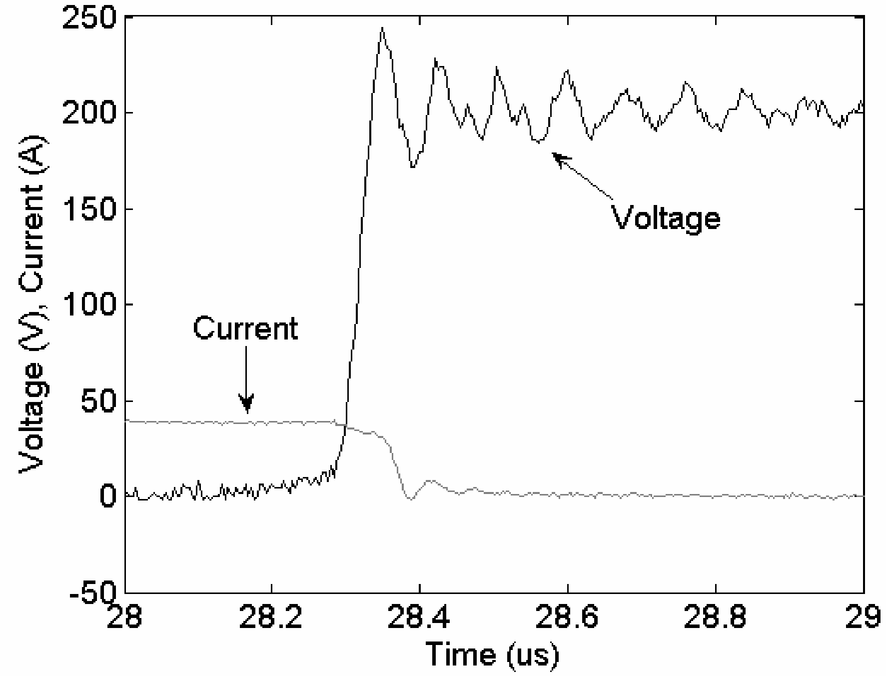

Figure 6-12: Detailed view of voltage across and current through switch in hard-switched converter during turn-off event

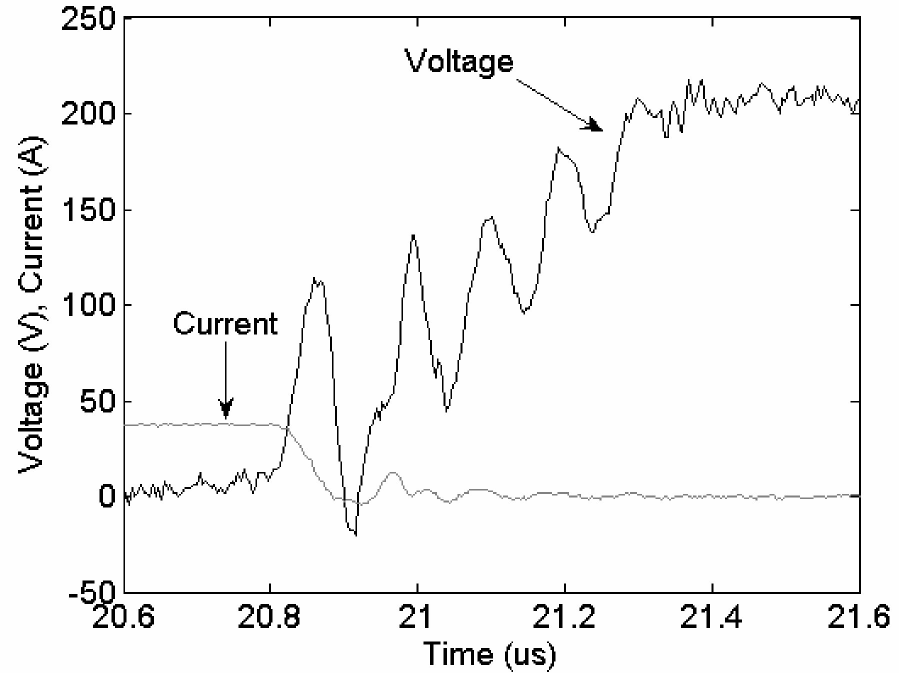

Figure 6-13: Detailed view of voltage across and current through main switch (S_1) in regenerative-snubber converter during turn-off event

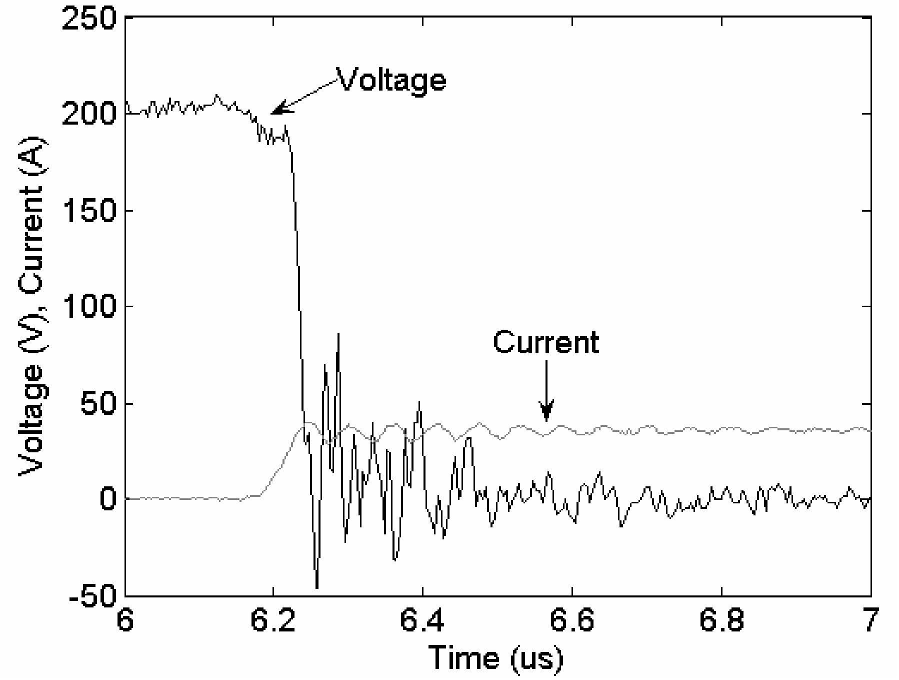

Figure 6-14: Detailed view of voltage across and current through switch in hard-switched converter during turn-on event

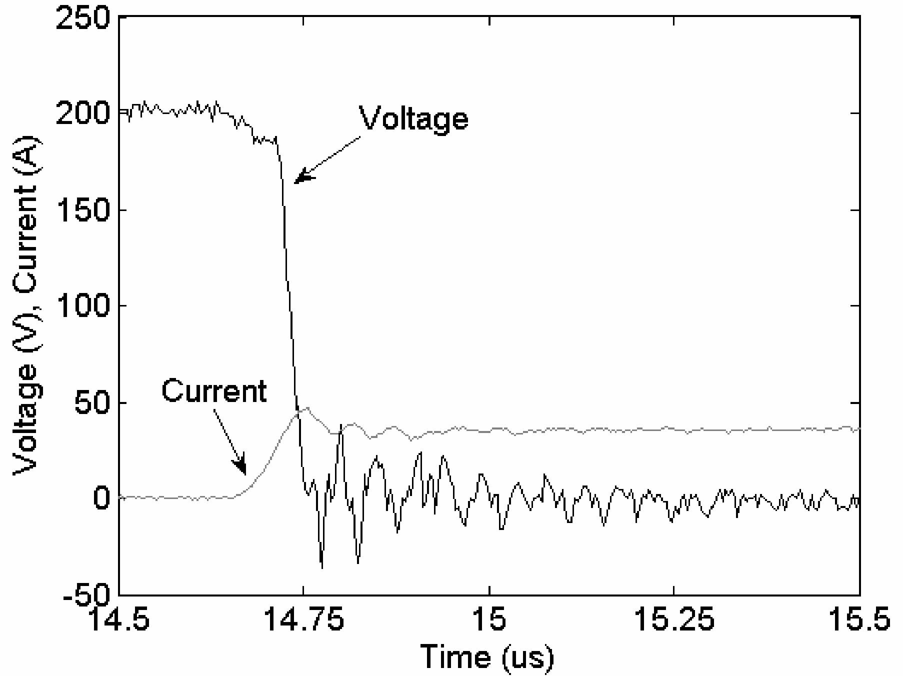

Figure 6-15: Detailed view of voltage across and current through main switch (S_1) in regenerative-snubber converter during turn-on event

Figure 6-16 and Figure 6-17 show the voltage across and current through the auxiliary switches (S_2 and S_3), as well as the snubber capacitor voltage, V_{Cs}, during two consecutive turn-off events of the main switch. During the first turn-off event of the main switch, S_3 is turned on (Figure 6-17), a current pulse I_{S3} passes through S_3 and the snubber capacitor charges up to the output voltage level. The voltage across S_3 stays at zero and the voltage across S_2 follows the voltage across the main switch and rises to the output voltage level. When the main switch S_1 is turned on, the voltage across S_3 remains at zero and the voltage across S_2 follows the voltage across the main switch and falls to zero. During the next turn-off event, S_2 is turned on (Figure 6-16) and a current pulse I_{S2} passes through S_2, discharging the snubber capacitor to zero. This makes the voltage across S_3 rise as the voltage across the main switch rises. When S_1 is turned on again, the voltage across S_2 remains at zero and the voltage across S_3 follows the voltage across the main switch and falls to zero. This cycle repeats itself during the following turn-off and turn-on events of the main switch. As seen from Figure 6-16 and Figure 6-17, the auxiliary switches have virtually no switching losses, because the switch voltages are nearly zero when conduction begins and ends.

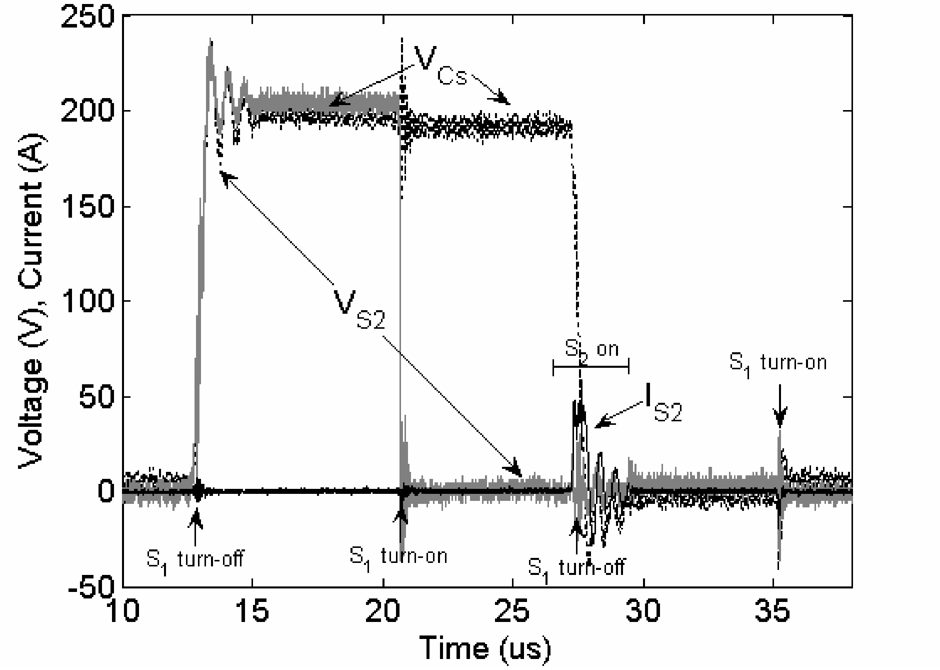

Figure 6-16: Regenerative-snubber converter: voltage across auxiliary switch S_2 (V_{S2}), current through auxiliary switch S_2 (I_{S2}), and voltage across snubber capacitor (V_{Cs}) during 2 consecutive turn-off events of the main switch (S_1)

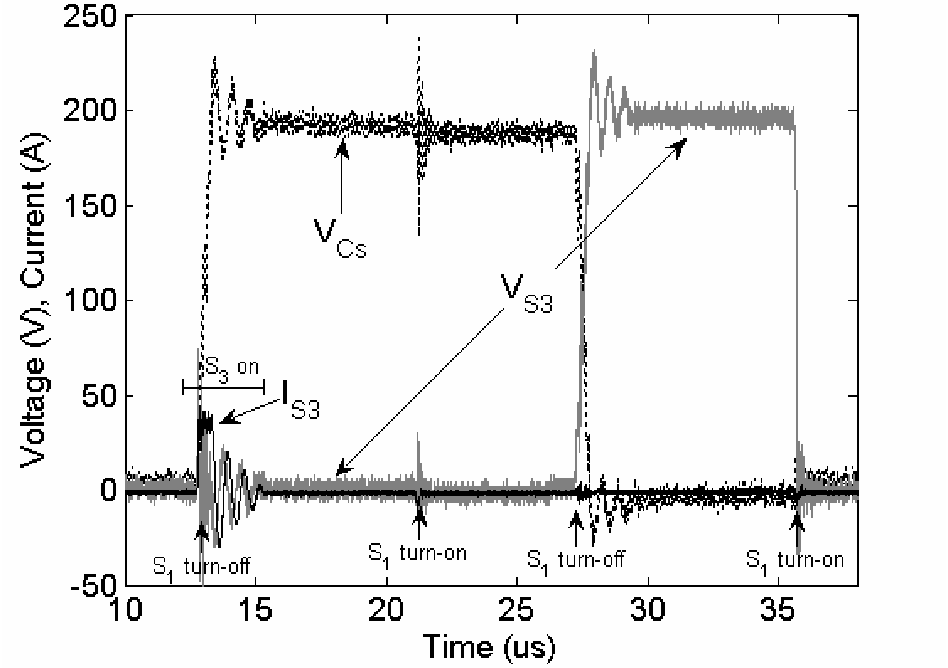

Figure 6-17: Regenerative-snubber converter: voltage across auxiliary switch S_3 (V_{S3}), current through auxiliary switch S_3 (I_{S3}), and voltage across snubber capacitor (V_{Cs}) during 2 consecutive turn-off events of the main switch (S_1)

Table 6-2 provides a quantitative comparison of switching and conduction losses in the two converters. The power loss for each turn-on switching event is integrated over 0.5 μs and the power losss for each turn-off switching event is integrated over 0.8 μs to obtain the energy loss per event. These particular time intervals were selected for each type of event so that the main switching transients were captured in each interval, but conduction losses in the switch after or before the event were not included in the integration for switching losses. All results shown are for the case when the output power, P_{out}, equals 4kW and the output voltage equals 200V. The results show that in the hard-switched converter, the turn-off losses are over double the turn-on losses when the SiC diodes are used. Also, the energy loss per turn-off event for the regenerative-snubber converter is reduced by 68.8% compared to that for the hard-switched converter. As expected from the simulation results, the total switching power loss is approximately equal in the hard-switched converter switching at 30kHz and the regenerative-snubber converter switching at 60kHz. Also, the regenerative-snubber converter reduces the conduction losses in the main switch by reducing the duty cycle for a particular voltage boost. These conduction losses are transferred to the auxiliary switches, allowing the main switch to operate at an even higher frequency before reaching its thermal limits.

Table 6-2: Power and Energy Loss in Hard-Switched and Regenerative Snubber Converters

	Hard-Switched Converter (30kHz)	Regenerative-Snubber Converter (30kHz)	Regenerative-Snubber Converter (60kHz)
Turn-On Energy Loss	0.256 mJ	0.231 mJ	0.231 mJ
Turn-On Power Loss	7.68 W	6.93 W	13.86 W
Turn-Off Energy Loss	0.538 mJ	0.168 mJ	0.168 mJ
Turn-Off Power Loss	16.14 W	5.04 W	10.08 W
Improvement in Turn-Off Power Loss	-	68.8%	37.5%
Total Switching Power Loss	23.82 W	11.97 W	23.94 W
Main IGBT Conduction Loss	23.94 W	23.085 W	23.085 W
Total Power Loss in Main IGBT	47.76 W	35.055 W	47.025 W
Auxiliary IGBT Conduction Loss	-	0.855 W	0.855 W
Auxiliary Diode Conduction Loss	-	0.787 W	0.787 W
Snubber Capacitor Resistive Loss	-	0.2816 W	0.2816 W
Total Power Loss for Main IGBT and Regenerative Snubber Circuit Components	47.76 W	36.98 W	48.95 W
Converter Efficiency Improvement From Hard-switched Converter at P_{out} = 4kW	-	0.27%	N/A (different inductor)

Due to the noise present in the voltage waveforms, which is especially significant at the low voltages present during conduction, the conduction losses in the main switch and in the auxiliary components shown in Table 6-2 have been calculated based on the measured duty cycles and current. The measured current magnitude in the main switch and auxiliary components when P_{out} = 4kW is approximately 38A. The on-time of the main switch in the hard-switched converter is 14 μs, which corresponds to a duty cycle, d_{HS}, of 0.42. The on-time of the main switch in the regenerative-snubber converter switching at 30kHz is 13.5 μs, which corresponds to a duty cycle, d_{RS}, of 0.405. Since each auxiliary IGBT, switching at 15kHz, alternates being on at each turn-off event, the conduction loss can be easily calculated by treating both switches as one IGBT switching at 30kHz with an on-time of 0.5 μs, which corresponds to a duty cycle, d_{AUX}, of 0.015. The two auxiliary diodes can be treated in the same way, using the same duty cycle d_{AUX} = 0.015. Finally, the equivalent series resistance of the snubber capacitor, R_{Cs}, is obtained from the component datasheet to determine the power loss in the capacitor using the auxiliary component duty cycle, d_{AUX} = 0.015. Equations (6-2) to (6-6) show the calculations of the conduction and snubber capacitor losses shown in Table 6-2.

$$P_{S1conduction,HS} = V_{CE@I_C} \times I_C \times d_{HS} = 1.5V \times 38A \times 0.42 = 23.94W \quad \textbf{(6-2)}$$

$$P_{S1conduction,RS} = V_{CE@I_C} \times I_C \times d_{RS} = 1.5V \times 38A \times 0.405 = 23.085W \quad \textbf{(6-3)}$$

$$P_{S2,3conduction,RS} = V_{CE@I_C} \times I_C \times d_{AUX} = 1.5V \times 38A \times 0.015 = 0.855W \quad \textbf{(6-4)}$$

$$P_{D2,3conduction,RS} = V_{FW@I_F \div 5} \times I_F \times d_{AUX} = 1.38V \times 38A \times 0.015 = 0.7866W \quad \textbf{(6-5)}$$

$$P_{ESR,Cs} = \left(I_{Cs}\right)^2 \times R_{Cs} \times d_{AUX} = \left(38A\right)^2 \times 13m\Omega \times 0.015 = 0.2816W \quad \textbf{(6-6)}$$

An analysis of the overall converter efficiency is crucial to verifying the advantages of using the proposed regenerative snubber circuit. The efficiency data for the regenerative-snubber converter operating at 60kHz and at 30kHz, and for the hard-switched converter operating at 30kHz, is show in Figure 6-18 for the output power range 2 kW to 5 kW. Note that when the regenerative-snubber converter is operated at 30kHz, the 500-μH boost inductor is used rather than the 250-μH inductor shown in Figure 6-9 so that a fair comparison can be made between the two converters operating at the same frequency. This is an important point because the 250-μH inductor is smaller, and thus, has lower resistive and magnetic losses than the 500-μH inductor.

Figure 6-18 shows that when the switching frequencies and boost inductor sizes are kept constant (at 30kHz and 500μH respectively) between the two converters, the regenerative-snubber converter attains higher efficiency than the hard-switched converter due to the reduced switching losses at turn-off. Furthermore, these efficiency results verify the measurements and calculations given in Table 6-2, since at an output power of about 4kW, the efficiency of the regenerative-snubber converter is about 0.25% higher than that of the hard-switched converter, which is in close agreement with the 0.27% increase calculated in Table 6-2.

The greatest advantage of the regenerative-snubber converter is revealed when the efficiencies of the hard-switched converter at 30kHz are compared with those of the regenerative-snubber converter at 60kHz. From Table 6-2 it can be inferred that the switching losses are approximately equal in these two cases. The significant increase in the efficiency of the regenerative-snubber converter is due to the decreased resistive and magnetic losses in the 250-μH boost inductor compared to the larger 500-μH boost inductor. This result shows that the use of the capacitor-switched regenerative snubber allows operation at double the maximum hard-switching frequency (which reduces converter size – to be quantified in Section 6.3.2), while increasing the converter efficiency.

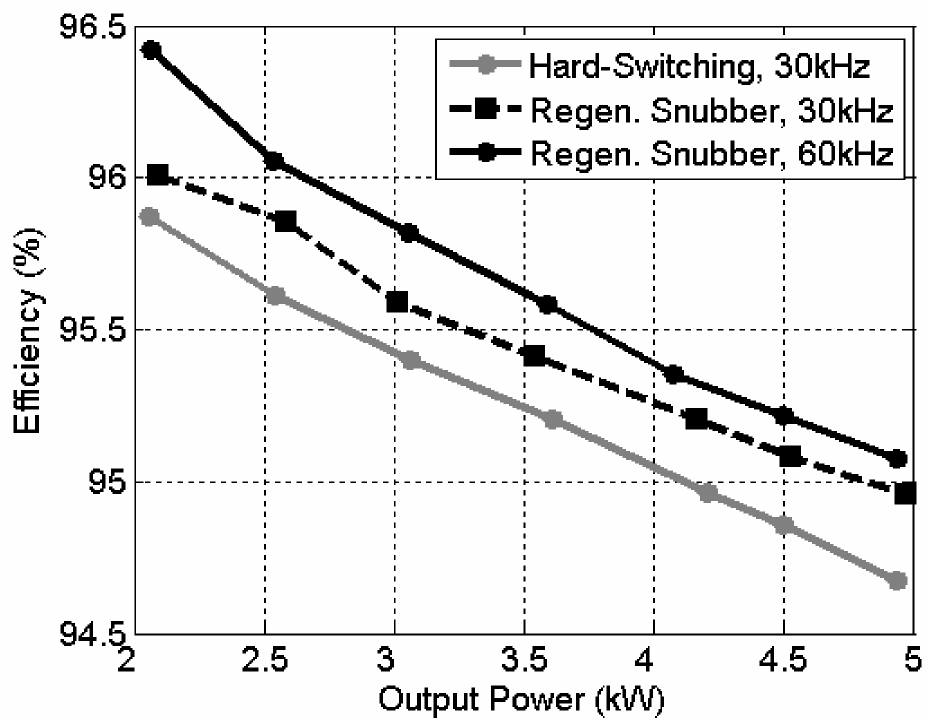

Figure 6-18: Comparison of the efficiency of the regenerative-snubber converter prototype with a switching frequency of 60kHz and 30kHz with the efficiency of the hard-switched converter prototype with a switching frequency of 30kHz

6.3.2 Mass Analysis

In the experimental prototypes, the IGBTs used are oversized for the operating power level, due to the reasons given in Section 6.3. Therefore, in order to accurately determine the mass reduction from using the capacitor-switched regenerative snubber circuit, the analysis is done on converters with appropriately-sized IGBTs, which would be the case for mass-produced converters. Therefore, the International Rectifier IGBT, IRG4PSC71UD, is used in place of the Powerex IGBT in the prototype for the mass analysis (I_c = 60A, V_{CES} = 600V, switching frequency = 8 – 60kHz, mass = 6g).

Table 6-3 shows the resulting mass analysis for both prototypes. It is shown that the boost inductor mass is reduced by 38.1% from the 500-μH inductor to the 250-μH inductor and that the overall mass reduction for the proposed converter is 16.14%. It is also important to note that the inductors contribute a significant amount to the mass of the converter. This emphasizes one advantage of the capacitor-switched regenerative snubber circuit: no heavy auxiliary inductors are required. Further reductions in mass could be obtained if both input and output LC-filters were required, as the filter inductors required for the capacitor-switched regenerative-snubber converter would again be smaller than the inductors required for the hard-switched converter.

Table 6-3: Mass Analysis of Hard-Switched and Regnerative-Snubber Converters

Component	Component Mass (kg)	Number in Hard-Switched Converter	Number in Regenerative Snubber Converter	Hard-Switched Converter Mass (kg)	Regenerative Snubber Converter Mass (kg)
IGBT	0.006	1	3	0.006	0.018
Driver + circuitry	0.05	1	3	0.05	0.15
SiC Diode	0.01	5	15	0.05	0.15
Boost Capacitor	0.44	1	1	0.44	0.44
Filter Capacitor	1.1	1	1	1.1	1.1
HS 500μH Inductor	2.1	1	0	2.1	0
HS Filter Inductor	0.12	1	0	0.12	0
RS 250μH Inductor	1.3	0	1	0	1.3
RS Filter Inductor	0.06	0	1	0	0.06
Snubber Capacitor	0.037	0	1	0	0.037
Total Mass				3.86	3.237
% Improvement				16.14%	

Another important practical aspect of a new design is the cost. An accurate cost analysis of the prototypes was not possible because the cost of the custom-made inductors and the other purchased components do not reflect high-volume production. However, it is projected that, depending on the particular design and power level, the additional cost of the auxiliary IGBTs, diodes, and snubber capacitor for the regenerative snubber converter can be partially or fully offset by the savings in cost due to using smaller passive components at the higher switching frequency.

6.4 Summary

This chapter proposes a novel capacitor-switched regenerative snubber for high-power DC/DC boost converters which has been shown to reduce mass and increase efficiency compared to the hard-switched converter. The capacitor-switched regenerative snubber circuit significantly reduces turn-off losses of the main switch and turn-on losses can be reduced by the use of zero-reverse-recovery SiC diodes. Unlike many soft-switching converters presented in the literature that use heavy extra inductors in the soft-switching circuit, the only additional components required for the proposed regenerative snubber circuit are two IGBTs, two diodes, and one capacitor. The two IGBTs used are connected in a leg arrangement, and thus a dual IGBT module can be used to minimize mass, volume, and cost. The snubber circuit is controlled by a simple strategy which is easily implemented and requires no additional sensors or feedback. The auxiliary switches are switched at zero-voltage and zero-current conditions.

To prove the concept experimentally, two 5-kW boost converters were built and tested. Though the hard-switched boost converter had a switching frequency of 30kHz and the capacitor-switched regenerative-snubber boost converter had a switching frequency of 60kHz, the regenerative snubber converter showed considerably higher efficiencies due to the reduction in turn-off switching losses and the reduced losses in the smaller inductor. A mass analysis showed that for an optimally designed converter, the regenerative-snubber converter gives a mass reduction of over 16% from the hard-switched converter due to the smaller passive components required at the higher switching frequency. Also, the extra cost of the auxiliary components can be partially or fully offset by the reduced cost of the passive components. Another benefit of using the regenerative snubber circuit is reduced voltage stress during switching events.

The proposed regenerative snubber for boost converters does not pose any practical limitations in terms of operating power or voltage boost. Its simple design and control, as well as high efficiency and mass reduction benefits, make it well suited for many applications such as fuel cell, hybrid-electric, and battery-electric vehicles, uninterruptible power supplies (UPS), and stationary grid-connected generating systems powered by fuel cells, photovoltaic arrays, and microturbines, requiring a voltage boost to control the current injected into the grid.

Chapter 7

Conclusions and Future Work

7.1 Summary of Contributions

Fuel cell vehicles are a promising technology which may soon revolutionize personal transportation and the automotive industry. The benefits of widespread proliferation of fuel cell vehicles are clear: high efficiency, zero harmful emissions, and a potentially renewable fuel. To aid in the commercialization of fuel cell vehicles, the research in this thesis has focused on advancing fuel cell vehicle design in order to improve vehicle performance and durability, increase efficiency, and reduce costs. The following discussion summarizes the main contributions of the thesis.

In Chapter 2, analysis was performed on numerous fuel cell vehicle powertrain topologies from the literature and the most promising topologies for each ESS type were selected for simulation in Chapter 4. This chapter also proposed two novel diode-based fuel cell-battery-ultracapacitor topologies, one without and one with an anti-parallel switch across the diode to enable charging of the battery with regenerative braking energy. The topology is unique from other fuel cell-battery-ultracapacitor topologies presented in the literature because it uses one low-power unidirectional DC/DC converter instead of the high-power bidirectional DC/DC converter usually employed, and the battery is connected to the ultracapacitor through a diode. This novel topology provides the following advantages over fuel cell-battery-ultracapacitor topologies presented in the literature: lower mass and cost, higher-efficiency battery charge and discharge paths, higher fault tolerance, and the option of a simple modification to create a plug-in vehicle. Furthermore, high-efficiency charging and discharging of the ultracapacitor is maintained and proper design of the system can ensure that the ultracapacitor provides the majority of the transient power requirements, thus reducing battery use and extending the battery lifetime.

Chapter 3 provides insight into the design and control of a 65-kW DC/DC boost converter for use in a fuel cell vehicle. It is shown that the input-current-control method for the boost converter is advantageous to the output-voltage-control method because (i) it is more suitable for intuitively controlling the power flow in the vehicle powertrain and (ii) it has both the poles and the zero in the left-half s-plane (LHP) meaning arbitrarily good tracking is achievable. The results from Chapter 3 pertaining to DC/DC converter mass, cost, and control are applied to the vehicle simulator models developed in Chapter 4.

Chapter 4 provided an in-depth and detailed comparison of near-optimal fuel cell-battery, fuel cell-ultracapacitor, and fuel cell-battery-ultracapacitor vehicles using a custom-made vehicle simulator in MATLAB/Simulink. Acceleration time, fuel economy, and cost were included in the objective function and estimated battery durability was also used to approximate lifetime costs. The simulation results lead to the following conclusions:

(1) Due to the present and predicted future high relative cost of fuel cells compared to batteries and ultracapacitors, the optimal fuel cell size (i.e., power rating) is approximately equal to the minimum power required for cruising at high speeds and powering the auxiliary vehicle systems. For the SUV used in this study, the ideal fuel cell size was 40kW.

(2) A fuel cell-ultracapacitor vehicle is the least-desirable vehicle choice due to the relatively high powertrain cost and low fuel economy resulting from the high vehicle mass.

(3) The novel diode-based fuel cell-battery-ultracapacitor topology presented in Chapter 2 is an overall improvement compared to the best fuel cell-battery-ultracapacitor topology found in the literature, which uses a high-power DC/DC converter to connect the battery to the high-voltage bus, because it yields higher fuel economy and has a lower cost.

(4) The fuel cell-battery and fuel cell-battery-ultracapacitor vehicles are close competitors. The optimized fuel cell-battery vehicle is generally less costly initially and can offer better acceleration (for a given ESS cost range); yet the optimized fuel cell-battery-ultracapacitor vehicle (using the novel topology) has slightly higher fuel economy and most importantly can extend the battery lifetime due to less battery stress. Based on an analysis of the battery currents in both vehicle types, it is probable that the battery life extension will translate into fewer required replacements of the battery over the vehicle lifetime, and thus the lifetime cost of the fuel cell-battery-ultracapacitor vehicle has the potential to be significantly lower than the lifetime cost of the fuel cell-battery vehicle.

Chapter 5 has presented an analytical optimization method to determine optimal sizes of the battery and ultracapacitor in the novel battery-ultracapacitor topology for both design options (i.e., with and without the anti-parallel switch across the diode). This optimization method gives engineers an analytical tool for creating an optimal design of the novel battery-ultracapacitor topology for a given system and power requirement profile, while providing insight into the relationship between battery and ultracapacitor sizing and system efficiency.

Chapters 2, 4, and 5 focus on the optimization of fuel cell vehicle components and powertrain topologies to increase knowledge in the area of optimal fuel cell vehicle design. However, the power electronic converters used in fuel cell and electric vehicle powertrains are also an important area of research, as these converters contribute significant mass and cost to the powertrain and have a large impact on the vehicle efficiency and fuel economy. For these reasons, Chapter 6 investigates soft-switching methods presently available for DC/DC boost converters, and proposes a novel capacitor-switched regenerative snubber for high-power DC/DC boost converters which is shown experimentally to reduce mass and increase efficiency compared to the hard-switched converter. The novel topology is unique in that it does not require any extra inductors in the soft-switching circuit, which, at high power levels, can be large and heavy. Furthermore, the capacitor-switched regenerative snubber circuit is controlled by a simple strategy which is easily implemented and requires no additional sensors or feedback. The proposed regenerative snubber circuit's simple design and control, as well as high efficiency and mass reduction benefits, make it well suited for many applications such as fuel cell, hybrid-electric, and battery-electric vehicles, as well as any other non-automotive applications where a high-power boost converter is required.

Hence, the main contributions of this thesis provide new ideas to improve the design of fuel cell vehicles in the areas of powertrain topologies, energy storage systems, and power electronic converters.

7.2 Suggestions for Future Work

In regards to future work on fuel cell vehicle design, the following directions are proposed:

- The vehicle simulator can be improved and extended by including more in-depth battery modeling details which can be obtained from extensive experimental testing of the desired battery cell. Firstly, the battery degradation under high current loads, such as those present in hybrid vehicle powertrains, can be measured and quantified. As the battery is charged and discharged, the cell capacity reduces, and the end of the cell lifetime is approached. It would be desirable to derive an analytical relationship between the current magnitude and frequency of the battery current pulses over the drive cycle, including the thermal environment of the cell, and the expected lifetime of the battery cell. This relationship could be used within the vehicle simulator to give the expected battery lifetime for a specific drive cycle given the current profile of the battery over that cycle. This result would give a quantitative measurement of the increase in battery lifetime when using an ultracapacitor for most of the transient power requirements in a battery-ultracapacitor ESS, and thus, would give a quantitative measure of the lifetime costs of both the fuel cell-battery vehicle and the fuel cell-battery-ultracapacitor vehicle. Secondly, the equivalent series resistance within the battery changes slightly as a function of battery state-of-charge (SOC) and current. Thus, experimental testing of the battery cell could give results quantifying this resistance change, and the battery model in the vehicle simulator could be made more accurate by including this variable battery resistance.

- Similar experimental testing could be done on the ultracapacitor cell, so that cell lifetime can be quantified, though this data will not have as profound an effect on the vehicle optimization results as that obtained for battery cells because the ultracapacitor is already known to have a significantly longer lifetime than the battery.
- This thesis has presented an intuitive control strategy for use in the fuel cell vehicle; yet, the research area of powertrain control is rich with possibilities to find new ways to improve vehicle efficiency and increase the lifetime of the powertrain components through optimal control strategies.
- In terms of the higher-level vehicle optimization, there is a natural extension to investigate the addition of the plug-in capability to fuel cell vehicles in terms of the impact on fuel economy, vehicle cost, control strategies, and the optimal sizing of components.
- Further to the previous idea, it is useful to extend the study to include pure-electric vehicles, which can be powered by a battery or a battery and an ultracapacitor. In this type of study, fuel cell and battery durability are crucial metrics to quantify in order to accurately predict lifetime costs of both vehicle types.

Appendix A

Derivation of Average State-Space Model for Boost Converter

The average state-space modeling technique [40] is used to obtain the state-space model of the boost converter operating in continuous current mode based on the boost converter circuit shown in Figure 3-4. When the switch is closed, or in the ON state, the following system of first-order differential equations describes the input (or inductor) current and the output (or capacitor) voltage.

$$\frac{di_{in}}{dt} = \frac{V_{in}}{L} \tag{A-1}$$

$$\frac{dv_{out}}{dt} = -\frac{v_{out}}{RC} \tag{A-2}$$

When the switch is open, or in the OFF state, the following system of first-order differential equations describes the inductor (or input) current and the capacitor (or output) voltage.

$$\frac{di_{in}}{dt} = -\frac{v_{out}}{L} + \frac{V_{in}}{L} \tag{A-3}$$

$$\frac{dv_{out}}{dt} = \frac{i_{in}}{C} - \frac{v_{out}}{RC} \tag{A-4}$$

Equations (A-1) to (A-4) are used to create an expression for the average input (or inductor) current and average output (or capacitor) voltage, as shown in Equations (A-5) and (A-6). The duty cycle, *d*, is the amount of time, relative to the period, that the switch is ON during each switching period.

$$\begin{aligned} \frac{di_{in}}{dt}, ave. &= d \times \frac{di_{in}}{dt}(ON - state) + (1-d) \times \frac{di_{in}}{dt}(OFF - state) \\ &= d \times \left(\frac{V_{in}}{L}\right) + (1-d) \times \left(-\frac{v_{out}}{L} + \frac{V_{in}}{L}\right) \\ &= -\frac{1-d}{L} v_{out} + \frac{V_{in}}{L} \end{aligned} \tag{A-5}$$

$$\begin{aligned}\frac{dv_{out}}{dt}, ave. &= d \times \frac{dv_{out}}{dt}(ON-state) + (1-d) \times \frac{dv_{out}}{dt}(OFF-state) \\ &= d \times \left(-\frac{v_{out}}{RC}\right) + (1-d) \times \left(\frac{i_{in}}{C} - \frac{v_{out}}{RC}\right) \\ &= \frac{1-d}{C} i_{in} - \frac{v_{out}}{RC}\end{aligned} \tag{A-6}$$

For simplicity, let:

$$\frac{di_{in}}{dt} = \frac{di_{in}}{dt}, ave. \qquad \frac{dv_{out}}{dt} = \frac{dv_{out}}{dt}, ave. \tag{A-7}$$

Therefore,

$$\begin{aligned}\frac{di_{in}}{dt} &= -\frac{1-d}{L} v_{out} + \frac{1}{L} V_{in} \\ \frac{dv_{out}}{dt} &= \frac{1-d}{C} i_{in} - \frac{1}{RC} v_{out}\end{aligned} \tag{A-8}$$

Equation (A-8) is a system of first-order nonlinear differential equations of the general form:

$$\begin{aligned}\frac{d\overline{x}}{dt} &= f(\overline{x}, \overline{u}) \qquad where \quad \overline{x} = \begin{bmatrix} i_{in} \\ v_{out} \end{bmatrix}, \overline{u} = \begin{bmatrix} V_{in} \\ d \end{bmatrix} \\ \overline{y} &= g(\overline{x}, \overline{u})\end{aligned} \tag{A-9}$$

This system of nonlinear differential equations can be linearized about the operating points V_{in}^* and V_{out}^* to obtain the average state-space model of the boost converter in continuous current operation, as shown in Equation (A-10).

$$\begin{aligned}\frac{d}{dt}\begin{bmatrix} \Delta i_{in} \\ \Delta v_{out} \end{bmatrix} &= \begin{bmatrix} 0 & -\frac{V_{in}^*}{LV_{out}^*} \\ \frac{V_{in}^*}{CV_{out}^*} & -\frac{1}{RC} \end{bmatrix}\begin{bmatrix} \Delta i_{in} \\ \Delta v_{out} \end{bmatrix} + \begin{bmatrix} \frac{1}{L} & \frac{1}{L} V_{out}^* \\ 0 & -\frac{V_{out}^{*\ 2}}{RCV_{in}^*} \end{bmatrix}\begin{bmatrix} \Delta V_{in} \\ \Delta d \end{bmatrix} \\ \overline{y} &= \begin{bmatrix} 0 & 1 \\ 1 & 0 \end{bmatrix}\begin{bmatrix} \Delta i_{in} \\ \Delta v_{out} \end{bmatrix} + \begin{bmatrix} 0 & 0 \\ 0 & 0 \end{bmatrix}\begin{bmatrix} \Delta V_{in} \\ \Delta d \end{bmatrix}\end{aligned} \tag{A-10}$$

Appendix B

Photographs of DC/DC Converter Prototypes

Figures B-1 and B-2 show photographs of the experimental prototypes designed and built to obtain the results given in the analysis in Chapter 6. Figure B-1 shows the hard-switched converter prototype and Figure B-2 shows the capacitor-switched regenerative-snubber converter prototype. For both converters, the components were attached to a large heatsink and air-cooled with a fan. The labels on each figure identify the components shown in the photographs.

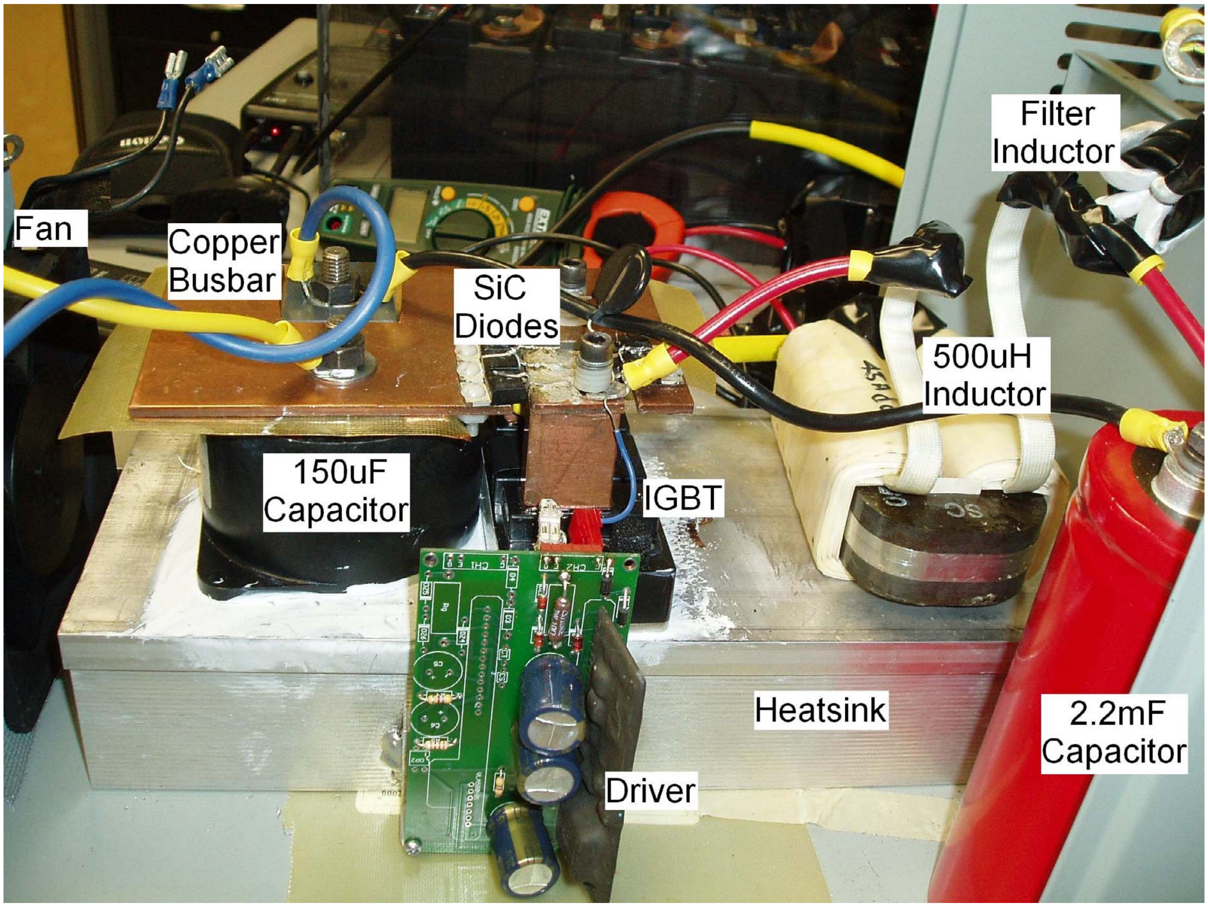

Figure B-1: Photograph of the hard-switched boost converter analyzed in Chapter 6

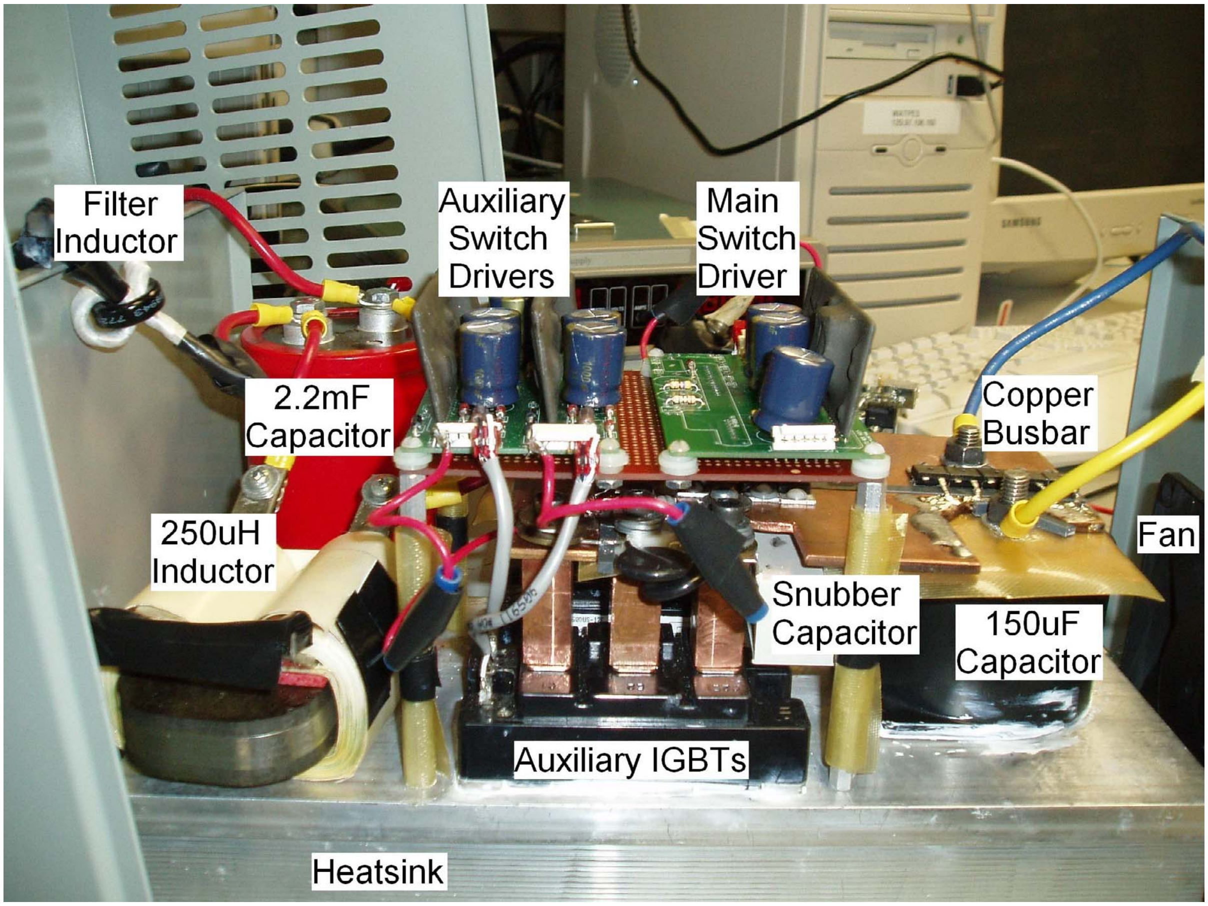

Figure B-2: Photograph of the capacitor-switched regenerative-snubber converter presented and analyzed in Chapter 6

Bibliography

---

[1] J. H. Wood, G. R. Long, and D. F. Morehouse, "Long-Term World Oil Supply Scenarios: The Future Is Neither as Bleak or Rosy as Some Assert", US Department of Energy, 2004. Available Jan. 2008: http://www.eia.doe.gov/pub/oil_gas/petroleum/feature_articles/2004/worldoilsupply/oilsupply04.html

[2] L. Bernstein et. al., "Intergovernmental Panel on Climate Change Fourth Assessment Report – Climate Change 2007: Synthesis Report – Summary for Policymakers", *Intergovernmental Panel on Climate Change*, 2007. Available Jan. 2008: www.ipcc.ch

[3] N. Kunzli et all, "Public-Health Impact of Outdoor and Traffic-Related Air Pollution: A European Assessment", *The Lancet*, Vol. 356, Number 9232, September 2000, pp. 795-801.

[4] C. C. Chan, "The State of the Art of Electric, Hybrid, and Fuel Cell Vehicles", *Proceedings of the IEEE*, Vol. 95, Issue 4, April 2007, pp. 704-718.

[5] L. G. Schumacher, W. Marshall, J. Krahl, W. B. Wetherell, and M. S. Grabowski, "Biodiesel Emissions Data from Series 60 DDC Engines", *Transactions of the American Society of Agricultural and Biological Engineers*, Vol 44(6), 2001, pp. 1465-1468.

[6] J. Rifkin, "Hydrogen Economy: The Creation of the World-Wide Energy Web and the Redistribution of Power on Earth", Penguin Putnam, New York, 2002.

[7] Fuel Cell Light Duty Vehicles, Available Jan. 2008: http://www.fuelcells.org/info/charts.html

[8] EG&G Services, "Fuel Cell Handbook – Fifth Edition", US Department of Energy, Office of Fossil Energy, West Virginia, 2000.

[9] US Department of Energy, Energy Efficiency and Renewable Energy, Available Jan. 2008: http://www.eere.energy.gov/hydrogenandfuelcells/fuelcells/fc_types.html

[10] HyPM Power Module Brochure, Hydrogenics Corporation, Available Jan. 2008: http://www.hydrogenics.com/power/products.hypm.asp

[11] Ballard, Available Jan. 2008: http://www.ballard.com/Automotive_Fuel_Cells/Application_Overview.htm

[12] Honda News Release, Available Jan. 2008: http://world.honda.com/news/2005/4050629.html

[13] C. Huang and A. T-Raissi, "Analyses of One-Step Liquid Hydrogen Production from Methane and Landfill Gas", *Journal of Power Sources*, Vol. 172, Issue 2, November 15, 2007, pp. 950-958.

[14] M. J. Barbosa, J. M. S. Rocha, J. Tramper, and R. H. Wijffels, "Acetate as a Carbon Source for Hydrogen Production by Photosynthetic Bacteria", *Journal of Biotechnology*, Vol. 85, Issue 1, January 23, 2001, pp. 25-33.

[15] A. Burke, "Batteries and Ultracapacitors for Electric, Hybrid, and Fuel Cell Vehicles", in *Proceedings of the IEEE*, Vol. 95, Issue 4, April 2007, pp. 806-820.

[16] Cobasys, Available Jan. 2008: http://www.cobasys.com/products/transportation_product_info.shtml

[17] Saft, Available Jan. 2008: www.saft.fr

[18] A123 Systems, Available Jan. 2008: http://www.a123systems.com

[19] Maxwell Technologies, Available Jan. 2008: http://www.maxwell.com/ultracapacitors/products/medium-cell/bcap0350.asp

[20] J.-S. Lai and D.J. Nelson, “Energy Management Power Converters in Hybrid Electric and Fuel Cell Vehicles”, *Proceedings of the IEEE*, Vol.95, No. 4, April 2007, pp.766-777.

[21] K.S. Jeong and B.S. Oh, “Fuel Economy and Life-Cycle Cost Analysis of a Fuel Cell Hybrid Vehicle”, *Journal of Power Sources*, 105, 2002, pp. 58-65.

[22] A. Emadi, K. Rajashekara, S. Williamson, and S. Lukic, “Topological Overview of Hybrid Electric and Fuel Cell Vehicular Power System Architectures and Configurations”, *IEEE Transactions on Vehicular Technology*, Vol. 54, No. 3, May 2005, pp. 763-770.

[23] A. Ohkawa, “Electric Power Control System for a Fuel Cell Vehicle Employing Electric Double-Layer Capacitor”, *SAE World Congress*, Detroit, 2004, SAE 2004-01-1006.

[24] W. Gao, “Performance Comparison of a Fuel Cell-Battery Hybrid Powertrain and a Fuel Cell-Ultracapacitor Hybrid Powertrain”, *IEEE Transactions on Vehicular Technology*, Vol. 54, No. 3, May 2005.

[25] Enova Systems, “60/90-kW Drive”, Available Jan. 2008: http://www.enovasystems.com

[26] A. Ritchie and W. Howard, “Recent Developments and Likely Advances in Lithium-Ion Batteries”, *Journal of Power Sources*, Vol. 162, 2006, pp. 809-812.

[27] J. Schindall, “The Charge of the Ultracapacitors”, *IEEE Spectrum*, November 2007, pp. 42-46.

[28] J. Miller, P. McCleer, and M. Cohen, “Ultracapacitors as Energy Buffers in a Multiple Zone Electrical Distribution System”, Maxwell Technologies White Paper, Available Jan. 2008: http://www.maxwell.com/ultracapacitors/technical-support/white_papers.asp

[29] Y. Wu and H. Gao, “Optimization of Fuel Cell and Supercapacitor for Fuel-Cell Electric Vehicles”, *IEEE Transactions on Vehicular Technology*, Vol. 55, No. 6, November 2006, pp. 1748-1755.

[30] R. Schupbach and J. Balda, “The Role of Ultracapacitors in an Energy Storage Unit for Vehicle Power Management”, in *Proc. of 2003 IEEE Vehicular Technology Conference,* Orlando, 2003, pp. 3236-3240.

[31] G. Pede, A. Iacobazzi, S. Passerini, A. Bobbio, and G. Botto, “FC Vehicle Hybridisation: An Affordable Solution for an Energy-Efficient FC Powered Drive Train”, *Journal of Power Sources*, vol. 125, 2004, pp. 280-291.

[32] A. Baisden and A. Emadi, “ADVISOR-Based Model of a Battery and an Ultra-capacitor Energy Source for Hybrid Electric Vehicles”, *IEEE Transactions on Vehicular Technology*, Vol. 53, No. 1, Jan. 2004, pp. 199-205.

[33] J. Bauman and M. Kazerani, “A Comparative Study of Fuel Cell-Battery, Fuel Cell-Ultracapacitor, and Fuel Cell-Battery-Ultracapacitor Vehicles”, *IEEE Transactions on Vehicular Technology*, (Accepted for future publication).

[34] R.A. Dougal, S. Liu, and R.E. White, “Power and Life Extension of Battery-Ultracapacitor Hybrids”, *IEEE Transactions on Components and Packaging Technologies*, Vol. 25, No. 1, March 2002, pp. 120-131.

[35] L. Gao, R.A. Dougal, and S. Liu, “Power Enhancement of an Actively Controlled Battery/Ultracapacitor Hybrid”, *IEEE Transactions on Power Electronics*, Vol 20, No. 1, Jan. 2005, pp. 236-243.

[36] M.J. Gielniak and Z.J. Shen, “Power Management Strategy Based on Game Theory for Fuel Cell Hybrid Electric Vehicles”, *IEEE Vehicular Technology Conference,* Los Angeles, Sept. 26-29, 2004, pp. 4422-2226.

[37] R. King and R.W.A.A. DeDoncker, "Low Cost Electronic Ultracapacitor Interface Technique to Provide Load Leveling of a Battery for Pulsed Load or Motor Traction Drive Applications", United States Patent, No. 5,723,956, March 3, 1998.

[38] A.W. Stienecker, T. Stuart, and C. Ashtiani, "An Ultracapacitor Circuit for Reducing Sulfation in Lead Acid Batteries for Mild Hybrid Electric Vehicles", *Journal of Power Sources*, Vol. 156, 2006, pp. 755-762.

[39] J.-S. Lai and D.J. Nelson, "Energy Management Power Converters in Hybrid Electric and Fuel Cell Vehicles", in *Proceedings of the IEEE*, Vol. 95, Issue 4, April 2007, pp. 766-777.

[40] D. Maksimovic, A.M. Stankovic, V.J. Thottuvelil, and G.C. Verghese, "Modeling and simulation of power electronic converters", in *Proceedings of the IEEE*, Vo. 89, Issue 6, June 2001, pp. 898-912.

[41] K. Wipke, M. Cuddy, and S. Burch, "ADVISOR 2.1: A User-Friendly Advanced Powertrain Simulation Using a Combined Backward/Forward Approach", *IEEE Transactions on Vehicular Technology*, Vol. 48, No. 6, Nov. 1999, pp. 1751-1761.

[42] Argonne National Laboratory Vehicle Systems Analysis Technical Team, "FreedomCAR and Fuel Partnership", September 2006, Available Jan. 2008: http://www.transportation.anl.gov/software/PSAT

[43] A. Rousseau, P. Sharer, and R. Ahluwalia, "Energy Storage Requirements for Fuel Cell Vehicles", *SAE World Congress*, Detroit, 2004, SAE 2004-01-1302.

[44] M.-J. Kim, and H. Peng, "Combined Control/Plant Optimization of Fuel Cell Hybrid Vehicles", in *Proc. of 2006 American Control Conference*, Minneapolis, 2006, pp.496-501.

[45] G. Paganelli, Y. Guezennec, and F. Rizzoni, "Optimizing Control Strategy for Hybrid Fuel Cell Vehicle", *SAE World Congress*, Detroit, 2002, SAE 2002-01-0102.

[46] J. Schiffer, O. Bohlen, R.W. De Doncker, D.U. Sauer, Ahn Kyun Young, "Optimized Energy Management for Fuel Cell-Supercap Hybrid Electric Vehicles", in *Proc. of 2005 IEEE Vehicle Power and Propulsion Conferenc*e, Chicago, 2005, pp. 341-348.

[47] H. Fathy, J. Reyer, R. Papalambros, and A. Ulsoy, "On the Coupling Between the Plant and Controller Optimization Problems", *Proc. of 2001 American Control Conference*, Arlington, 2001, pp.1864-1869.

[48] R.H. Perry and D.W. Green, "Perry's Chemical Engineers' Handbook (7th Edition)", McGraw-Hill, 1997.

[49] R. Rose, "Questions and Answers About Hydrogen and Fuel Cells" (Report style), Washington, DC: U.S. Dept. of Energy, 2005.

[50] US Department of Energy, "Future Fuel Cells R&D", http://www.fossil.energy.gov/programs/powersystems/fuelcells/

[51] J. Mierlo, P. Bossche, and G. Maggetto, "Models of Energy Sources for EV and HEV: Fuel Cells, Batteries, Ultracapacitors, Flywheels and Engine-Generators", *Journal of Power Sources,* Vol. 128, 2004, pp. 76-89.

[52] M. Keyser, M. Mihalic, A. Pesaran, and D. Rivers, "Thermal Characterization of Plastic Lithium Ion Cells", National Renewable Energy Laboratory, Jan. 2007.

[53] M. Amrhein and P. Krein, , "Dynamic Simulation for Analysis of Hybrid Electric Vehicle System and Subsystem Interactions, Including Power Electronics", *IEEE Transctions on Vehicular Technology*, Vol. 54, No. 3, May 2005, pp. 825-836.

[54] Correspondence with Tom Bresel, Electronic Craftsmen: www.ecraftsmen.com

[55] Powerex, Available Jan. 2008: www.pwrx.com

[56] N. Mohan, T. Undeland, and W. P. Robbins, "Power Electronics: Converters, Applications, and Design", John Wiley & Sons: New York, 2nd ed., 1995, pp. 172-178.

[57] M. Panagiotidis, D. Delagrammatikas, and D. Assanis, "Development and Use of a Regenerative Braking Model for a Parallel Hybrid Electric Eehicle", *SAE World Congress*, Detroit, March 6-9, 2000, SAE 2000-01-0995.

[58] K.H. Lui and F.C.Y. Lee, "Zero-Voltage Switching Technique in DC/DC Converters", *IEEE Transactions on Power Electronics*, Vol. 5, July 1990, pp. 293-304.

[59] Q. Li and P. Wolfs, "An Analysis of the ZVS Two-Inductor Boost Converter Under Variable Frequency Operation," *IEEE Transactions on Power Electronics*, Vol. 22, Jan. 2007, pp. 120-131.

[60] K. Smith and K. Smedley, "Properties and Synthesis of Passive Lossless Soft-Switching PWM Converters," *IEEE Transactions on Power Electronics*, Vol. 14, Sept. 1999, pp. 890-899.

[61] E.S. da Silva, L. dos Reis Barbosa, J.B. Vieira, L.C. de Freitas, and V.J. Farias, "An Improved Boost PWM Soft-Single-Switched Converter with Low Voltage and Current Stresses," *IEEE Transactions on Industrial Electronics*, Vol. 48, Dec. 2001, pp. 1174-1179.

[62] D. Dah-Chuan Lu, D. K.-W. Cheng, and Y.-S. Lee, "A Single-Switch Continuous-Conduction-Mode Boost Converter with Reduced Reverse-Recovery and Switching Losses", *IEEE Transactions on Industrial Electronics*, Vol. 50, Aug. 2003, pp. 767 -776.

[63] C.-J. Tseng and C.-L. Chen, "A Passive Lossless Snubber Cell for Nonisolated PWM DC/DC Converters", *IEEE Transactions on Industrial Electronics*, Vol. 45, Aug. 1998, pp. 593-601.

[64] M.M. Hernando, A. Fernandez, J. Garcia, D.G. Lamar, and M. Rascon, "Comparing Si and SiC Diode Performance in Commercial AC-to-DC Rectifiers with Power-Factor Correction", *IEEE Transactions on Industrial Electronics*, Vol. 53, April 2006, pp. 705-707.

[65] C.-M. Wang, "A New Family of Zero-Current-Switching (ZCS) PWM Converters", *IEEE Transactions on Industrial Electronics*, Vol. 52, Aug. 2005, pp. 1117-1125.

[66] H.-S. Choi and B. H. Cho, "Novel Zero-Current-Switching (ZCS) PWM Switch Cell Minimizing Additional Conduction Loss", *IEEE Transactions on Industrial Electronics*, Vol. 49, Feb. 2002, pp. 165 -172.

[67] L.H.S.C. Barreto, M.G. Sebastião, L.C. de Freitas, E.A.A. Coelho, V.J. Farias, and J.B. Vieira, Jr., "Analysis of a Soft-Switched PFC Boost Converter Using Analog and Digital Control Circuits", *IEEE Transactions on Industrial Electronics*, Vol. 52, Feb. 2005, pp. 221 -227.

[68] H. Bodur and A. F. Bakan, "An Improved ZCT-PWM DC-DC Converter for High-Power and Frequency Applications", *IEEE Transactions on Industrial Electronics,* Vol. 51, Feb. 2004, pp. 89-95.

[69] C.-M. Wang, "Novel Zero-Voltage-Transition PWM DC-DC Converters", *IEEE Transactions on Industrial Electronics*, Vol. 53, Feb. 2006, pp. 254-262.

[70] Y. Jang, M.M. Jovanovic, K.-H. Fang, and Y.-M. Chang, "High-Power-Factor Soft-Switched Boost Converter," *IEEE Transactions on Power Electronics*, Vol. 21, Jan. 2006, pp. 98-104.

[71] B. Ivanovic and Z. Stojiljkovic, "A Novel Active Soft Switching Snubber Designed for Boost Converters," *IEEE Transactions on Power Electronics*, Vol. 19, May 2004, pp. 658-665.

[72] J. Marshall and M. Kazerani, "A Novel Lossless Snubber for Boost Converters", *IEEE International Symposium on Industrial Electronics*, July 9-13 2006, Montreal, pp. 1030-1035.

[73] Cree, Available January 2008: www.cree.com/power